



Theoretical and experimental study of tunable liquid crystal lenses: wavefront optimization

Thèse

Oleksandr Sova

Doctorat en physique
Philosophiæ doctor (Ph. D.)

Québec, Canada

Theoretical and experimental study of tunable liquid crystal lenses: wavefront optimization

Thèse

Oleksandr Sova

Sous la direction de:

Tigran Galstian, directeur de recherche

Résumé

Les systèmes optiques adaptatifs ont des applications dans plusieurs domaines: imagerie (zoom et autofocus), médecine (endoscopie, ophtalmologie), réalité virtuelle et réalité augmentée. Les lentilles à base de cristaux liquides font une grande partie de l'industrie de l'optique adaptative parce qu'elles présentent de nombreux avantages par rapport aux méthodes traditionnelles. Malgré les progrès importants réalisés au cours des dernières décennies, certaines limitations de performances et de production existent toujours. Cette thèse explore les moyens de surmonter ces problèmes, en considérant deux types de lentilles adaptatives: lentille à cristaux liquides utilisant le principe de division diélectrique et lentille de contrôle modal.

L'introduction de cette thèse présente la théorie des cristaux liquides et des lentilles adaptatives, abordant également les lentilles à cristaux liquides existantes.

Dans le premier et le deuxième chapitres de cet ouvrage, nous démontrons les résultats de la modélisation théorique de la conception de lentilles à cristaux liquides à double couche diélectrique optiquement cachée. Nous avons étudié l'influence de paramètres géométriques, tels que l'épaisseur de la cellule à cristaux liquides, la forme et les dimensions des diélectriques qui forment la couche optiquement cachée, sur la puissance optique de la lentille. La puissance optique en fonction de la permittivité et de la conductivité relatives des diélectriques a été obtenue. Le comportement d'une telle lentille en présence de variation de température a été analysé.

Nous avons poursuivi la recherche du concept de couche diélectrique cachée en examinant des microstructures basées sur ce principe. Deux systèmes de microlentilles et microprismes ont été simulés. La comparaison de la dépendance de la modulation de phase optique sur la fréquence spatiale des microstructures a été obtenue. Les écarts par rapport aux fronts d'onde idéaux ont été évalués dans les deux cas. Nous avons également comparé les conceptions proposées avec une approche traditionnelle des électrodes interdigitales. Les dispositifs suggérés pourraient être utilisés pour l'orientation de faisceau laser ou comme des réseaux de microlentilles variables.

Dans le troisième et le quatrième chapitres, nous présentons une étude de lentilles adaptatives basées sur le principe de contrôle modal.

Nous avons vérifié les résultats de simulation en les comparant avec les dépendances obtenues expérimentalement de la puissance optique et des aberrations sphériques moyennes quadratiques. Nous avons exploré les modifications suivantes de la lentille de contrôle modal

traditionnelle: 1) électrode annulaire alimentée supplémentaire; 2) électrode à disque flottant; 3) combinaison des deux premiers cas. L'influence de chaque modification a été étudiée et expliquée. Les résultats des simulations ont montré qu'en utilisant la combinaison d'électrodes supplémentaires avec une technique d'alimentation optimale - le front d'onde pourrait être corrigé à travers la pleine ouverture de la lentille. La lentille modifiée répond aux exigences de faibles aberrations pour les applications ophtalmiques (par exemple, implant intraoculaire).

Finalement, une nouvelle conception d'une lentille de Fresnel de contrôle modal ayant une grande ouverture a été étudiée. Les performances d'imagerie de la lentille de Fresnel proposée ont été évaluées et comparées à la lentille de référence, construite en utilisant une approche de contrôle modal traditionnelle. Le prototype a démontré l'augmentation de la puissance optique par rapport à une lentille de contrôle modal conventionnelle du même diamètre d'ouverture. Un modèle théorique et des simulations numériques des lentilles de Fresnel ont été présentés. Les simulations ont démontré une possibilité d'amélioration considérable de la qualité d'image obtenue en utilisant des tensions et des fréquences optimisées.

Summary

Adaptive optical systems have applications in various domains: imaging (zoom and autofocus), medicine (endoscopy, ophthalmology), virtual and augmented reality. Liquid crystal-based lenses have become a big part of adaptive optics industry as they have numerous advantages in comparison with traditional methods. Despite significant progress made over the past decades, certain performance and production limitations still exist. This thesis explores ways of overcoming these problems, considering two types of tunable lenses: liquid crystal lens using dielectric dividing principle and modal control lens.

The introduction of this thesis presents the theory of liquid crystals and adaptive lenses, addressing existing liquid crystal lenses as well.

In the first and second chapters of this work we demonstrate the results of theoretical modeling of double dielectric optically hidden liquid crystal lens design. We have studied the influence of geometrical parameters, such as thickness of liquid crystal cell, shape and dimensions of dielectrics forming the optically hidden layer, on the optical power of the lens. The dependences of optical power on the relative permittivity and conductivity of dielectrics were obtained. The behavior of such a lens in the presence of temperature variation was analyzed.

We have further extended the concept of hidden dielectric layer to exploration of microstructures. Two systems of microlenses and microprisms have been simulated. The comparison of optical phase modulation dependence on spatial frequency of microstructures was obtained. Deviations from ideal wavefronts were evaluated in both cases. We also compared proposed designs with a standard interdigital electrode approach. Suggested devices could be used for continuous light steering or as tunable microlens arrays.

In the third and fourth chapters we present our studies of tunable lenses based on modal control principle.

We verified simulation results by comparing them with experimentally obtained dependences of optical power and root mean square spherical aberrations. We have explored the following modifications of conventional modal control lens: 1) additional powered ring electrode; 2) floating disk electrode; 3) combination of the first two cases. The influence of each modification was studied and explained. Simulation results showed that using the combination of additional electrodes along with optimal powering technique - the wavefront could be corrected within the entire clear aperture

of the lens. Modified lens meets low aberration requirements for ophthalmic applications (for example, intraocular implant).

Finally, a new design of a wide aperture tunable modal control Fresnel lens was investigated. Imaging performance of the proposed Fresnel lens was evaluated and compared with the reference lens built using traditional modal control approach. The prototype device demonstrated the increase of optical power in comparison with a conventional modal control lens of the same aperture size. A theoretical model and numerical simulations of the Fresnel lens design were presented. Simulations demonstrated a possibility of noticeable image quality improvement obtained using optimized voltages and frequencies.

Contents

Résumé.....	ii
Summary	iv
Contents.....	vi
List of tables.....	ix
List of figures	x
Acknowledgments.....	xv
Foreword	xvi
Introduction.....	1
I.1 Types of liquid crystals: nematics, smectics, cholesterics	1
I.2 Continuum theory of liquid crystals	2
I.3 Dielectric and optical anisotropies of liquid crystals.....	4
I.4 Liquid crystals in the presence of external electric field.....	6
I.5 Partial differential equations describing the reorientation of molecules.....	9
I.6 Optical phase retardation in nematic liquid crystals	12
I.7 Overview of existing tunable liquid crystal lens designs.....	13
I.8 Description of hidden layer and modal control lenses.....	18
I.9 Goals and motivation	21
Chapter 1 Theoretical analyses of a liquid crystal adaptive lens with optically hidden dielectric double layer.....	24
1.1 Résumé.....	25
1.2 Abstract	26
1.3 Introduction	26
1.4 Theoretical simulation of the lens geometry variations	29
1.4.1 Impact of the LC thickness.....	32
1.4.2 Hidden layer dimensions.....	33
1.5 Variations of material parameters of the lens.....	38
1.5.1 Increase of the relative permittivity of IML.....	38
1.5.2 Increase of the conductivity of IML.....	38
1.6 Environmental (temperature) dependence.....	39
1.7 Summary and conclusions.....	41
1.8 Acknowledgment	41
Chapter 2 Modulation transfer function of liquid crystal microlenses and microprisms using double dielectric layer.....	42
2.1 Résumé.....	43
2.2 Abstract	44
2.3 Introduction.....	44
2.4 Simulation details.....	45

2.5 Results	46
2.5.1 Hidden microlens array	46
2.5.2 Hidden microprism array	51
2.5.3 Out of plane switching	54
2.6 Summary and conclusions.....	56
2.7 Acknowledgment	57
Chapter 3 Liquid crystal lens with optimized wavefront across the entire clear aperture.....	58
3.1 Résumé	59
3.2 Abstract	60
3.3 Introduction	60
3.3.1 Basic design of the lens.....	60
3.3.2 Wavefront deformations across the entire clear aperture	62
3.4 Analysis of the modal control lens	63
3.4.1 Theoretical model.....	63
3.4.2 Comparison with experimental results	65
3.5 Wavefront improvement	68
3.5.1 Proposed design modification	68
3.5.2 Comparison of aberrations	71
3.6 Discussion	72
3.7 Conclusions	73
3.8 Acknowledgments.....	74
Chapter 4 Modal control refractive Fresnel lens with uniform liquid crystal layer	75
4.1 Résumé	76
4.2 Abstract	77
4.3 Introduction	77
4.4 Experimental method and materials	78
4.5 Experimental results.....	80
4.5.1 Interferometric-polarimetric measurements	80
4.5.2 Tests with Fresnel MC-TLCL and raspberry pi camera.....	83
4.6 Theoretical model.....	88
4.6.1 Comparison with experiment	88
4.6.2 Control optimization	91
4.7 Summary and conclusions.....	93
4.8 Acknowledgments.....	93
Summary and conclusions.....	94
Appendix A Nelder-Mead method.....	96
Appendix B PSF and MTF calculation	98

Bibliography..... 102

List of tables

Table 1.1. Experimental parameters used hereafter as reference for simulations.....	30
Table 1.2. Comparison of simulations for $H_{CL}=185\ \mu\text{m}$ and $H_{CL}=92.5\ \mu\text{m}$	35
Table 1.3. Examples of conductivity values for two different materials.....	39
Table 1.4. Simulation parameters.....	40
Table 2.1. Simulation parameters.....	45
Table 3.1. Parameter values used for simulations.....	67
Table 3.2. Optimization parameters and constraints.....	70
Table 4.1. Simulation parameters.....	88
Table 4.2. Optimized control parameters and corresponding calculated OPs.....	92
Table A.1. Pseudocode for the Nelder-Mead algorithm.....	97

List of figures

Figure I.1. Phase transitions of LCs with the increase of temperature.....	1
Figure I.2. Three possible deformations of NLC.....	3
Figure I.3. Molecule of 5CB LC ($C_{18}H_{19}N$). Color coding for atoms: black – carbon, white- hydrogen, blue – nitrogen.....	4
Figure I.4. Reorientation of LC molecule with (a) positive and (b) negative dielectric anisotropies in electric field.....	7
Figure I.5. Schematic representation of LC’s director in Cartesian coordinates.....	9
Figure I.6. Schematic representation of LC’s director in cylindrical coordinates.....	11
Figure I.7. Dependence of refractive index encountered by incident beam on director orientation (black arrow – direction of polarization, yellow arrow – direction of propagation).....	12
Figure I.8. One of the first LC lens designs [22].....	14
Figure I.9. GRIN LC lens with a hole-patterned electrode [24].....	14
Figure I.10. Schematics of an LC lens with a curved electrode [26].	15
Figure I.11. Scheme of refractive Fresnel lens described in [27].....	16
Figure I.12. Schematics of a hidden dielectric double layer lens [28].	18
Figure I.13. Schematic demonstration of the hidden layer LC lens with (a) zero control voltage and (b) applied voltage.....	19
Figure I.14. Geometry of a tunable modal control lens [31]. Dc – diameter of the controlling hole patterned electrode (HPE), WCL – weakly conductive layer, PI – polyimide alignment layer, L – thickness of the LC layer, UTE – uniform transparent electrode.....	20
Figure I.15. Equivalent electric circuit of the MC lens [31].	21
Figure 1.1. Schematic of the DDOH layer lens [30].	27
Figure 1.2. Schematic of the dielectric divider concept.	27
Figure 1.3. Example of experimentally measured dependence of OP of the lens versus the applied RMS voltage. U_{th} , U_{min} , and U_{max} are the threshold, minimum, and maximum considered voltages, respectively.	28
Figure 1.4. Parabolic approximation of optical phase retardation. Control voltage was (a) 10 V_{rms} and (b) 30 V_{rms} .	31
Figure 1.5. COP as a function of LC cell thickness and driving voltage.	32
Figure 1.6. Schematics of the double dielectric hidden layer.....	34
Figure 1.7. OP dependence on changes of the height H_{CL} of the CL (varied from 50% to 300% of the experimental value).....	36
Figure 1.8. Variation of the base radius of the CL.....	36
Figure 1.9. OP versus base radius of the CL.....	37
Figure 1.10. OP dependence on the relative permittivity of index matching layer. The relative permittivity of the CL was fixed to 3.9.....	38
Figure 1.11. OP dependence on the conductivity of index matching layer. Relative permittivity is the same for CL and IML. Conductivity of CL was constant: $\sigma_{CL}=1 \cdot 10^{-13}$ S/m.....	39
Figure 1.12. Temperature dependence of OP for (a) E49 and (b) 5CB LCs. Nematic-isotropic transition temperatures (T_{N-I}) for E49 and 5CB were about 97°C and 35.1°C, respectively.....	40
Figure 2.1. Schematics of the simulated microlens array with sinusoidal distribution of the CL material. ...	47
Figure 2.2. Optical power dependence on control voltage (single LC lens), for different thicknesses of middle glass substrate (aperture diameter = 1.75 mm).	47
Figure 2.3. Electric potential distribution in the middle of the LC cell for different numbers of microlenses within 2000 μm wide simulated system (different spatial frequencies).....	48
Figure 2.4. Modulation transfer function (the case of sinusoidal CL material).	49
Figure 2.5. Dependence of the optical power and lens aperture diameter of each microlens versus the number of CL units (the case of sinusoidal CL material).	50

Figure 2.6. Normalized RMS phase retardation deviation from ideal parabolic shape and difference between max and min phase retardation (the case of sinusoidal CL material) versus the number of CL units.	50
Figure 2.7. Schematics of the simulated microprism array.....	51
Figure 2.8. Electric potential distribution in the middle of the LC cell for different numbers of microprisms within 2000 μm wide simulated system (different spatial frequencies).....	51
Figure 2.9. Modulation transfer function (the case of microprism array).....	52
Figure 2.10. (a) Director tilt angle in the middle of the LC cell for 1, 3 and 5 microprisms over 2000 μm and (b) the corresponding phase shifts.....	52
Figure 2.11. Percentage of the prism width in the “dead zone” due to fringing fields versus the number of microprisms per 2000 μm	53
Figure 2.12. Normalized RMS phase retardation deviation from the (desired) linear form and the difference between max and min phase retardation values versus the number of microprisms over 2000 μm within the (a) “active zone” of single microprism and (b) in the entire clear aperture of the microprism (covering both active and passive zones).....	54
Figure 2.13. Schematics of the “out of plane” switching.	55
Figure 2.14. Modulation transfer function (the case of “out of plane” switching using patterned electrodes).	55
Figure 2.15. Optical power of each microlens depending upon the gap between two neighboring electrodes (the case of “out of plane” switching using patterned electrodes).....	56
Figure 2.16. Normalized RMS phase retardation deviation from ideal parabolic shape and difference between max and min phase retardation (the case of “out of plane” switching using patterned electrodes).	56
Figure 3.1. Conventional modal control LC lens design, WCL – weakly conductive layer, HPE – hole patterned electrode, UTE – uniform transparent electrode, LC – liquid crystal of thickness L	62
Figure 3.2. Simulated wavefront generated by a standard modal control lens (black solid line) versus the ideal parabolic fit (blue dashed line). $r = 0$ is the center of the lens, while $r = 1.5$ mm is its periphery.	62
Figure 3.3. Schematic representation of the experimental setup used for measuring the OPs and SAs of TLCLs: 1) He-Ne laser, 2) polarizers, 3) beam expander, 4) function generator, 5) TLCL, 6) relay lens, 7) Shack-Hartmann wavefront sensor.....	65
Figure 3.4. Experimentally measured dependences of real and imaginary relative permittivities (parallel and perpendicular components) of LC material upon applied signal’s frequency.....	66
Figure 3.5. (a) Comparison of simulated (open circles) and measured (filled squares) dependences of the OP of the standard modal control TLCL upon the driving frequency. (b) Comparison of corresponding RMS spherical aberrations vs frequency. Applied voltage is 5 V_{rms} . The clear aperture is 3 mm.....	67
Figure 3.6. Schematics of modified modal control lens designs. (a) MC lens with inner ring electrode ($D_{\text{in.r.}}$ – diameter of the inner ring electrode); (b) MC lens with a floating electrode ($D_{\text{fl.el.}}$ – diameter of the floating electrode); (c) a design combining components of (a) and (b).	68
Figure 3.7. Optical power (filled squares) and RMS SAs (open circles) simulated for a standard modal control lens with 4 mm clear aperture.	69
Figure 3.8. Comparison of RMS spherical aberrations vs optical power for different designs of optimized MC lenses: (a) MC; (b) MC+inner ring; (c) MC+floating electrode; (d) MC+inner ring+floating electrode.	71
Figure 3.9. (I) Normalized wavefronts and (II) deviations of phase retardation from the ideal shape: (a) MC; (b) MC+inner ring; (c) MC+floating electrode; (d) MC+inner ring+floating electrode.	72
Figure 3.10. RMS SAs of optimized lens with combined additional electrodes.....	73
Figure 4.1. Schematic presentation (a) and top substrate electrode pattern (b) of the studied Fresnel lens; WCL - weakly conductive layer, CRE – concentric ring electrodes, UTE - uniform transparent electrode, LC – liquid crystal.	79

Figure 4.2. Observed interference fringes obtained with the F-MC-TLCL placed between crossed polarizers. Green dashed lines separate inner and outer zones. $U = 4 V_{\text{rms}}$, (a) $f=10$ kHz, $U_I=0.35 V_{\text{rms}}$; (b) $f=10$ kHz, $U_I=2 V_{\text{rms}}$; (c) $f=20$ kHz, $U_I=0.35 V_{\text{rms}}$; (d) $f=20$ kHz, $U_I=2 V_{\text{rms}}$	81
Figure 4.3. Reconstructed phase profiles for the proposed F-MC-TLCL. Dashed lines are for eye guiding only.	81
Figure 4.4. Optical characterization for the reference (classic MC-TLCL) and the proposed here (F-MC-TLCL) lenses. (a) OP vs frequency, (b) RMS wavefront errors vs frequency. Solid lines are third order polynomial approximations used for eye guiding only.	82
Figure 4.5. Schematics of the experimental setup used for comparison of image quality between MC-TLCL and F-MC-TLCL: (1) raspberry pi v4 [100], (2) raspberry pi camera v2 [101], (3) F-MC-TLCL or MC-TLCL, (4) polarizer, (5) USAF resolution chart, (6) function generators.	83
Figure 4.6. Pictures of the USAF resolution chart recorded by using the raspberry pi camera with (a) conventional MC-TLCL (unpowered); (b) MC-TLCL with $U=3 V_{\text{rms}}$, $f=22.5$ kHz; (c) F-MC-TLCL with $U=4 V_{\text{rms}}$, $U_I=0.35 V_{\text{rms}}$, $f=22.5$ kHz. The small horizontal red line (in the centers of pictures) is used for intensity scan and analyses (see Fig. 4.7).	84
Figure 4.7. Contrast plots (a) conventional MC-TLCL (unpowered); (b) MC-TLCL with $U=3 V_{\text{rms}}$, $f=22.5$ kHz; (c) F-MC-TLCL with $U=4 V_{\text{rms}}$, $U_I=0.35 V_{\text{rms}}$, $f=22.5$ kHz.	85
Figure 4.8. Picture of a target with increasing spatial frequency (in lp/mm) (a) without TLCL, when the raspberry pi camera is focused to infinity; (b) using MC-TLCL with $U=3 V_{\text{rms}}$, $f=22.5$ kHz; (c) using F-MC-TLCL with $U=4 V_{\text{rms}}$, $U_I=0.35 V_{\text{rms}}$, $f=22.5$ kHz. Blue horizontal lines are used for following intensity scans (see Fig. 4.9).	85
Figure 4.9. Contrast comparison for various spatial frequencies along the blue horizontal line (see Fig. 4.8) without TLCL, raspberry pi camera is focused to infinity (dashed blue line with circles); using conventional MC-TLCL (red dashed line with triangles) and F-MC-TLCL (black solid line).	86
Figure 4.10. Pictures of objects taken with raspberry pi camera focused to infinity (a) without TLCL, (b) MC-TLCL with $U=3 V_{\text{rms}}$, $f=22.5$ kHz; (c) F-MC-TLCL with $U=4 V_{\text{rms}}$, $U_I=0.35 V_{\text{rms}}$, $f=22.5$ kHz; (d) – solid lines are gray values measured along red lines shown in (a)–(c), lines with symbols are corresponding Gaussian fits.	87
Figure 4.11. Experimental measurements of 5CB's real and imaginary relative permittivity components at different applied signal's frequencies.	89
Figure 4.12. Comparison of (a) OPs and (b) RMS aberrations (total RMS wavefront errors in case of experiment and RMS SAs in case of theory) between experimentally acquired data and results obtained through simulations with fitting parameters.	90
Figure 4.13. RMS wavefront errors vs OPs. Experimental results for MC-TLCL ($U=3 V_{\text{rms}}$) – black line with squares, experimental result for F-MC-TLCL ($U=4 V_{\text{rms}}$, $U_I=0.35 V_{\text{rms}}$) – red line with circles, simulation of F-MC-TLCL ($U=4 V_{\text{rms}}$, $U_{I\text{eff}}=1.61 V_{\text{rms}}$) – blue line with up triangles, simulation of F-MC-TLCL (optimized driving) – green line with down triangles.	91
Figure 4.14. Wavefront comparisons (a) and processed wavefronts (b) with parabolic approximations (solid lines): experimentally obtained wavefront for F-MC-TLCL ($U=4 V_{\text{rms}}$, $U_I=0.35 V_{\text{rms}}$, $f=22.5$ kHz) – black line with squares; simulated F-MC-TLCL ($U=4 V_{\text{rms}}$, $U_{I\text{eff}}=1.61 V_{\text{rms}}$, $f=22.5$ kHz) – red line with circles; simulated F-MC-TLCL (optimized driving) – blue line with triangles.	92
Figure B.1. Schematics of light propagation through LC lens.	98
Figure B.2. Point spread function of simulated modal control lenses with 4 mm clear aperture: (a) – traditional approach, (b) – modified lens with improved aberrations.	99
Figure B.3. Modulation transfer function of simulated modal control lenses with 4 mm clear aperture: (a) – traditional approach, (b) – modified lens with improved aberrations.	99
Figure B.4. Simulated phase profiles of micropisms (orange dashed lines) and corresponding ideal profiles (blue solid lines) in the case of (a) 1 prism over 2000 μm and (b) 3 prisms over 2000 μm	100

Figure B.5. Light intensity distribution (arbitrary units) along direction of beam propagation (z axis), simulated using (a) ideal prism phase retardation profile, (b) phase retardation profile of a microprism with the “dead zone”. Spatial frequency of the hidden dielectric structure is 1 microprism over 2000 μm (see Fig. B.4 (a)).	100
Figure B.6. Light intensity distribution (arbitrary units) along direction of beam propagation (z axis), simulated using (a) ideal prisms’ phase retardation profile, (b) phase retardation profile of microprisms with the “dead zone”. Spatial frequency of the hidden dielectric structure is 3 microprisms over 2000 μm (see Fig. B.4 (b)).	101

In memory of my grandfather

Acknowledgments

Firstly, I would like to thank Professor Tigran Galstian for giving me an opportunity to do my doctoral studies at Laval University. I want to express my gratitude for all discussions, comments and advices that I have received from him working on different projects. He has provided enormous help and support during my research. Without his guidance and encouragement this thesis would not have been possible.

I would also like to thank the Theoretical Physics Department of Taras Shevchenko National University of Kyiv. I am particularly grateful to Professor Victor Reshetnyak, who has introduced me to the world of liquid crystals and constantly supported me on my scientific journey.

I thank the R&D group of LensVector Inc. for the use of their equipment, discussions and technical advices.

I would like to thank Professor Michel Piché for reviewing the present thesis before submission. His valuable remarks and comments have helped to increase the quality of this work.

I want to thank the administrative and technical staff of COPL and Laval University for providing all necessary services, permitting me to conduct my research. Particularly, I want to thank Patrick Larochelle and Souleymane Toubou Bah who have always found ways to resolve any issues in laboratories.

I thank the Sentinel North of NSERC/Laval University for their financial support.

Thanks to my family in Ukraine and friends (all over the world) who have welcomed my decision to move to Canada to continue my studies and helped me to integrate into Quebec society. I would like to express special thanks to my wife who has been by my side every step of this PhD project.

Finally, I want to thank my mother who has inspired me to become a physicist.

Foreword

This thesis is based on four articles published in peer-reviewed journals. I am the principal author in all the articles that were inserted in the thesis.

The thesis begins with an introduction into theory of liquid crystals. All numerical models presented further in this thesis were constructed within the theoretical framework described in the introduction.

An overview of existing tunable liquid crystal lens designs is presented. Their advantages and drawbacks are discussed referring to publications. The designs explored in this PhD project are briefly introduced.

The first chapter consists of an article discussing design and theoretical analyses of controllable liquid crystal lenses that use optically hidden dielectric double layer. The second chapter studies a possibility to extend the concept of hidden dielectric layer to construction of tunable microlens and microprism arrays. These articles were co-authored by Professor Victor Reshetnyak from Taras Shevchenko National University of Kyiv:

- O. Sova, V. Reshetnyak, T. Galstian, *Theoretical analyses of a liquid crystal adaptive lens with optically hidden dielectric double layer*, J. Opt. Soc. Am. A. 34 (2017) 424–431.
- O. Sova, V. Reshetnyak, T. Galstian, *Modulation transfer function of liquid crystal microlenses and microprisms using double dielectric layer*, Appl. Opt. 57 (2018) 18–24.

All authors participated in the discussion and manuscript writing. Simulation results presented in these articles were obtained by me.

The third and fourth chapters discuss tunable lenses based on modal control. In the third chapter we present the theory of modal control lenses. We verify the results of numerical simulations by comparing them with experimental data. Then we suggest several design modifications that help to improve image quality provided by these lenses. In the fourth chapter we present an article in which we introduce a new design of a wide aperture tunable modal control Fresnel lens. The experimental procedure is discussed. Comparison of experimental measurements of the Fresnel lens with a conventional reference lens is performed and analyzed. A theoretical model and optimization strategy are presented.

- O. Sova, T. Galstian, *Liquid crystal lens with optimized wavefront across the entire clear aperture*, Opt. Commun. 433 (2019) 290–296.

- O. Sova, T. Galstian, *Modal control refractive Fresnel lens with uniform liquid crystal layer*, Opt. Commun. 474 (2020) 126056

Experiments and designs were discussed with Professor Tigran Galstian. Sample preparations, experimental measurements and theoretical simulations were realized by me. The manuscripts were written under supervision of Professor Tigran Galstian. I provided my versions of the manuscripts which then were completed in accordance with Professor Galstian's edits and recommendations.

Co-authors:

Tigran Galstian: Center for Optics, Photonics and Laser, Department of Physics, Engineering Physics and Optics, Laval University, Pav. d'Optique-Photonique, 2375 Rue de la Terrasse, Québec, G1V 0A6, Canada.

e-mail: galstian@phy.ulaval.ca

Victor Reshetnyak: Theoretical Physics Department, Taras Shevchenko National University of Kyiv, Volodymyrska street 64, Kyiv, 01601, Ukraine.

e-mail: VReshetnyak@univ.kiev.ua

Publications during PhD program:

1. O. Sova, V. Reshetnyak, T. Galstian, *Theoretical analyses of a liquid crystal adaptive lens with optically hidden dielectric double layer*, J. Opt. Soc. Am. A. 34 (2017) 424–431.
2. T. Galstian, O. Sova, K. Asatryan, V. Presniakov, A. Zohrabyan, M. Evensen, *Optical camera with liquid crystal autofocus lens*, Opt. Express. 25 (2017) 29945–29964.
3. O. Sova, V. Reshetnyak, T. Galstian, *Modulation transfer function of liquid crystal microlenses and microprisms using double dielectric layer*, Appl. Opt. 57 (2018) 18–24.
4. O. Sova, T. Galstian, *Liquid crystal lens with optimized wavefront across the entire clear aperture*, Opt. Commun. 433 (2019) 290–296.
5. O. Sova, T. Galstian, *Modal control refractive Fresnel lens with uniform liquid crystal layer*, Opt. Commun. 474 (2020) 126056

Conference presentations

1. O. Sova, T. Galstian, *Modal liquid crystal lens with optimized wavefront control*, Photonics North, Montreal, June 5-7, 2018.

2. O. Sova, T. Galstian, *Refractive modal control liquid crystal Fresnel lens*, Sentinel North Scientific Meeting, Lévis, August 26-28, **2019**
3. O. Sova, T. Galstian, *Refractive modal control liquid crystal Fresnel lens*, OLC 2019, Quebec, September 8-13, **2019**

Introduction

I.1 Types of liquid crystals: nematics, smectics, cholesterics

Liquid crystalline state of matter has been discovered in the 19th century. In the state of mesophase, liquid crystals (LCs) possess properties of both liquids (molecular flow) and crystals (optical, dielectric, diamagnetic anisotropies). In order to characterize LCs, a unit vector, called the director $\mathbf{n}(\mathbf{r})$, that shows the average orientation of long molecular axes of LC molecules at a certain position in space was introduced [1]. It should be noticed that \mathbf{n} and $-\mathbf{n}$ states are identical. The first classifications of LCs were made based on director's orientation relative to the centers of mass of molecules. Generally, LCs are divided into two main groups: thermotropic and lyotropic. For thermotropic LCs, mesophase exists only in a certain range of temperatures, when for lyotropic LCs it depends on the concentration of amphiphilic molecules [2]. Further in this thesis we will discuss only thermotropic LCs.

Thermotropic LCs can be subdivided into several types: nematic, smectic and cholesteric. Some LCs can transition from one mesophase to another with the increase of temperature. These possible phase changes as a function of temperature are demonstrated in Figure I.1:

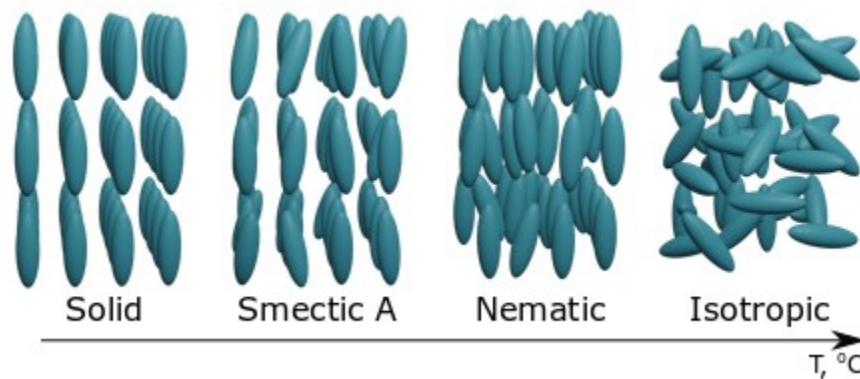


Figure I.1. Phase transitions of LCs with the increase of temperature.

Nematic LCs (NLC) have molecules that are elongated in one direction. The centers of mass of these molecules are distributed in space chaotically [3]. Therefore, no positional, but only long-range orientational order is present in nematics. Their molecules can be approximated with rods or cylinders. It is one of the most common liquid crystalline phases. The molecules can be oriented with external electric or magnetic fields (as a consequence of anisotropy, see hereafter). Uniformly oriented samples are optically uniaxial and strongly birefringent [2]. Nematics have found numerous

applications is modern commercial technologies such as displays [4], beam steering devices [5], tunable lenses [6].

Smectic LCs have well defined layers of molecules. This mesophase is observed at lower temperatures than nematic one and has higher degree of order. Molecular structure of smectics resembles a two-dimensional crystal, where in each layer the molecules are oriented at a certain angle relative to layer's surface. Layers can slide freely over each other as interlayer forces are weak in comparison with lateral forces between molecules in each layer [2].

Cholesteric mesophase possesses higher symmetry in comparison with nematics. It is composed of optically active molecules that gradually change their orientation, rotate around the axis normal to director. This twist can be either left- or right-handed depending on molecular structure. The distance at which molecules make one full rotation around the axis is called a chiral pitch. The pitch can be varied with temperature or by adding other molecules.

Although cholesteric and smectic LCs are interesting from scientific research and commercial device production sides (reflective cholesteric display [7], light shutters [8]), our work is based on investigation of nematics.

I.2 Continuum theory of liquid crystals

To give a theoretical description of phenomena observed in LCs we need a parameter that characterizes long-range orientational order. The director gives only qualitative characterization of molecular orientation and does not depict the influence of external electric field, mechanical deformations, or temperature [3]. Therefore, the use of director alone for LC characterization becomes insufficient. Thus, we define an order parameter, which is a second rank tensor as follows [1]:

$$Q_{\alpha\beta} = Q(T) \left(n_{\alpha} n_{\beta} - \frac{1}{3} \delta_{\alpha\beta} \right), \quad (I.1)$$

where $Q(T)$ – temperature dependent scalar order parameter; n_{α} , n_{β} – director components, $\delta_{\alpha\beta}$ - Kronecker delta. In the case of isotropic liquids $Q(T) = 0$, for solids its value becomes 1 and for all known nematic phases $0 < Q(T) < 1$ [9,10].

It is convenient to consider LC as a continuous medium, disregarding the processes that take place on molecular scale [1,11]. This approach is justified when the following conditions are fulfilled [12]:

1) The energy of intermolecular interactions is much higher than given energy per molecule participating in physical processes

2) Involved characteristic distances (where we can observe significant variations of $Q_{\alpha\beta}$) for these phenomena are larger ($\sim 1 \mu\text{m}$) than molecular dimensions ($\sim 20 \text{ \AA}$) [1]

Developed by Oseen [13] and Frank [14] continuum theory can successfully describe the behavior of LCs in the presence of external (electric or magnetic) fields as well as orientational effects coming from bounding substrates.

Equilibrium state of LCs corresponds to a minimum of free energy. Deviation from this state comes with additional energy related to LC deformations [3]. We can construct the expression for free energy density, developing it into series of tensor order parameter and its gradients (corresponding to energy distortions). Because tensor $Q_{\alpha\beta}$ varies at much larger distances than molecular size - the distorted state of nematics can be described in terms of $\mathbf{n}(\mathbf{r})$. The director is assumed to vary slowly and smoothly within the volume of LCs.

We distinguish three main types of deformations of NLCs due to the influence of external fields (electric or magnetic). They are called splay, twist and bend (Fig. I.2).

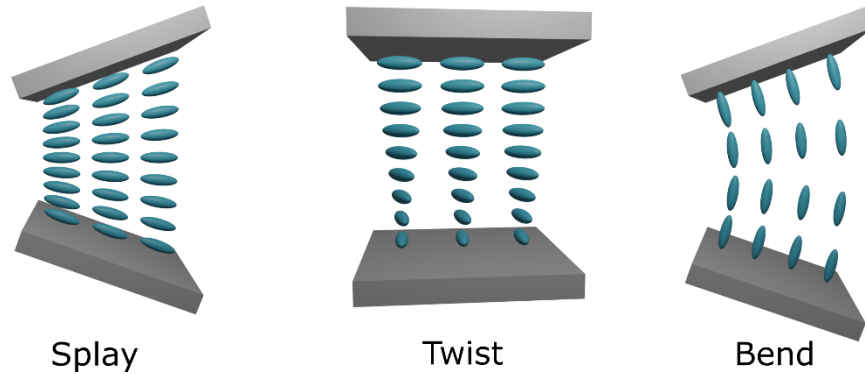


Figure I.2. Three possible deformations of NLC.

Frank and Oseen have suggested an expression describing the contributions of each basic deformation into total free energy density:

$$f = \frac{1}{2} K_{11} (\nabla \mathbf{n})^2 + \frac{1}{2} K_{22} (\mathbf{n} \cdot \nabla \times \mathbf{n})^2 + \frac{1}{2} K_{33} (\mathbf{n} \times \nabla \times \mathbf{n})^2, \quad (\text{I.2})$$

where K_{11} , K_{22} , K_{33} are splay, twist and bend elastic constants respectively (terms used by analogy with solid materials). Then the expression for elastic free energy of LC can be written as

$$F_{elastic} = \frac{1}{2} K_{11} \int (\nabla \mathbf{n})^2 dV + \frac{1}{2} K_{22} \int (\mathbf{n} \cdot \nabla \times \mathbf{n})^2 dV + \frac{1}{2} K_{33} \int (\mathbf{n} \times \nabla \times \mathbf{n})^2 dV. \quad (I.3)$$

This expression is the fundamental equation of the elastic continuum theory of nematics [12]. Further we will use it to describe the response of LC molecules to the presence of electric field.

I.3 Dielectric and optical anisotropies of liquid crystals

The molecules of LCs have various forms (for example disc shaped or banana-shaped) that define their physical properties. We will discuss nematic molecules that are elongated in one direction. The molecular conformation of a typical NLC 5CB is shown in Figure I.3.

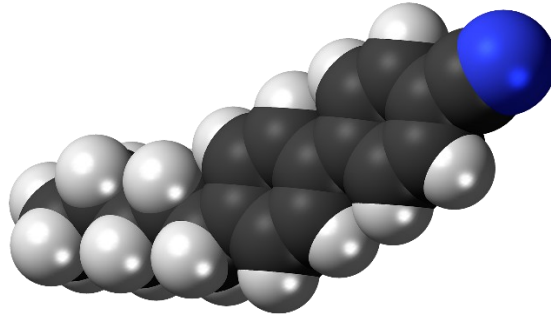


Figure I.3. Molecule of 5CB LC ($C_{18}H_{19}N$). Color coding for atoms: black – carbon, white – hydrogen, blue – nitrogen.

In practice, LC mixtures are often used (for example E49 or E7 which contains multiple components: $C_{18}H_{19}N$, $C_{20}H_{23}N$, $C_{21}H_{25}NO$, $C_{24}H_{23}N$). LC molecules are mostly composed of neutral atoms. But bonds between atoms lead to one part of the molecule to possess a positive charge when the other part possesses a negative charge. Thus, these molecules are permanent dipoles. The situation when molecules are electrically neutral, but in the presence of electric field the charges inside them are displaced (induced dipole) is also possible [15]. As the result of dipole moment present in NLCs, their orientation can be controlled with application of electric field (this will be discussed in detail in section I.4).

Liquid crystals exhibit anisotropic properties due to their molecular structure. Dielectric constants measured along (ϵ_{\parallel}) long molecular axis and perpendicular to it (ϵ_{\perp}) have significantly different values. Dielectric anisotropy of an LC is defined as $\epsilon_a = \epsilon_{\parallel} - \epsilon_{\perp}$. In contrast with isotropic materials, the dielectric permittivity of LCs is not a constant, but a second rank tensor. To describe the propagation of light in liquid crystals we further consider them to be electrically anisotropic, non-conductive and magnetically isotropic. Strictly speaking, LCs have magnetic anisotropy $\chi_a = \chi_{\parallel} - \chi_{\perp}$

(where χ_{\parallel} and χ_{\perp} are magnetic susceptibilities measured along and perpendicular to director, respectively), but $\chi_a \ll 1$ and hence magnetic permeability $\mu \approx 1$ [10,16].

To consider propagation of light in anisotropic medium we start with Maxwell's equations for electric and magnetic fields. In this section we use Gaussian convention. In the absence of free charges and currents, Maxwell's equations take the following form:

$$\nabla \cdot \mathbf{D} = 0 \quad (\text{I.4})$$

$$\nabla \cdot \mathbf{B} = 0 \quad (\text{I.5})$$

$$\nabla \times \mathbf{E} + \frac{1}{c} \frac{\partial \mathbf{B}}{\partial t} = 0 \quad (\text{I.6})$$

$$\nabla \times \mathbf{H} - \frac{1}{c} \frac{\partial \mathbf{D}}{\partial t} = 0, \quad (\text{I.7})$$

where c is the speed of light, \mathbf{E} – electric field vector, \mathbf{H} – magnetic field vector, \mathbf{B} – magnetic induction vector, \mathbf{D} – dielectric displacement vector.

The solutions for electric and magnetic fields are plane monochromatic waves:

$$\mathbf{E} = \mathbf{E}_0 e^{i(\mathbf{k}\mathbf{r} - \omega t)} \quad (\text{I.8})$$

$$\mathbf{H} = \mathbf{H}_0 e^{i(\mathbf{k}\mathbf{r} - \omega t)}. \quad (\text{I.9})$$

Substituting Equations (I.8), (I.9) into Equations (I.6), (I.7) and introducing a unit vector $\mathbf{s} = \frac{\mathbf{k}}{|\mathbf{k}|}$, where $|\mathbf{k}| = \frac{\omega n}{c}$, Equations (I.6), (I.7) transform into (I.10) and (I.11) correspondingly:

$$n[\mathbf{s} \times \mathbf{E}] = \mu \mathbf{H} \quad (\text{I.10})$$

$$n[\mathbf{s} \times \mathbf{H}] = -\mathbf{D}, \quad (\text{I.11})$$

where constitutive relation $\mathbf{B} = \mu \mathbf{H}$ has been used.

Excluding \mathbf{H} from Equations (I.10) and (I.11), we can rewrite (I.11) as

$$\mathbf{D} = \frac{n^2}{\mu} (\mathbf{E} - \mathbf{s}(\mathbf{s} \cdot \mathbf{E})). \quad (\text{I.12})$$

As mentioned above, dielectric permittivity in anisotropic materials is a tensor. Given the fact that this tensor is symmetric, we can choose a coordinate system where it would have only diagonal components:

$$\hat{\varepsilon} = \begin{pmatrix} \varepsilon_x & 0 & 0 \\ 0 & \varepsilon_y & 0 \\ 0 & 0 & \varepsilon_z \end{pmatrix}. \quad (\text{I.13})$$

Then Equation (I.12) takes the following form (where \mathbf{E} is now $\mathbf{E}=\mathbf{E}_0e^{i(\mathbf{k}\cdot\mathbf{r})}$):

$$\mu\epsilon_i E_i = n^2 (E_i - s_i (\mathbf{s} \cdot \mathbf{E})), \quad i = x, y, z. \quad (\text{I.14})$$

Performing a series of simple mathematical transformations using Equation (I.14) that are described in [17], we obtain Fresnel's equation of wave normals:

$$s_x^2 (\nu_p^2 - \nu_y^2) (\nu_p^2 - \nu_z^2) + s_y^2 (\nu_p^2 - \nu_z^2) (\nu_p^2 - \nu_x^2) + s_z^2 (\nu_p^2 - \nu_x^2) (\nu_p^2 - \nu_y^2) = 0, \quad (\text{I.15})$$

where $\nu_p = \frac{c}{n}$ - phase velocity, $\nu_i = \frac{c}{\sqrt{\mu\epsilon_i}}$ ($i=x, y, z$) - principal velocities of propagation.

Further we will consider only optically uniaxial crystals ($\nu_o = \nu_x = \nu_y$, $\nu_e = \nu_z$) as this represents the case of NLC. Defining the angle between z axis and vector \mathbf{s} (parallel to \mathbf{k}) to be θ , Equation (I.15) becomes:

$$(\nu_p^2 - \nu_o^2) [(\nu_p^2 - \nu_e^2) \sin^2 \theta + (\nu_p^2 - \nu_o^2) \cos^2 \theta] = 0. \quad (\text{I.16})$$

This quadratic equation has two solutions for ν_p^2 :

$$\nu_{p1}^2 = \nu_o^2 \quad (\text{I.17})$$

$$\nu_{p2}^2 = \nu_o^2 \cos^2 \theta + \nu_e^2 \sin^2 \theta. \quad (\text{I.18})$$

Finally, these solutions can be rewritten in terms of refractive indices as follows:

$$n_1 = n_o \quad (\text{I.19})$$

$$n_2 = \frac{n_o n_e}{\sqrt{n_e^2 \cos^2 \theta + n_o^2 \sin^2 \theta}}. \quad (\text{I.20})$$

Therefore, in the anisotropic media, such as NLC, we can observe two propagating waves: the ordinary wave encounters the ordinary refractive index, which is independent of direction of propagation; the extraordinary wave encounters an effective refractive index that changes as a function of angle between wave vector and optical axis.

I.4 Liquid crystals in the presence of external electric field

The orientation of LC molecules changes under the influence of external electric or magnetic fields. We will discuss the case of electric field as it is used for most practical applications. The energy that comes from the contribution of electric field:

$$F_E = -\frac{1}{2} \int (\mathbf{E} \cdot \mathbf{D}) dV, \quad (\text{I.21})$$

where $\mathbf{D} = \varepsilon_0 \hat{\varepsilon} \mathbf{E}$ is dielectric displacement vector, $\hat{\varepsilon}$ - dielectric tensor. Then the whole expression for free energy becomes

$$F = F_{elastic} + F_E = \frac{1}{2} K_{11} \int (\nabla \mathbf{n})^2 dV + \frac{1}{2} K_{22} \int (\mathbf{n} \cdot \nabla \times \mathbf{n})^2 dV + \frac{1}{2} K_{33} \int (\mathbf{n} \times \nabla \times \mathbf{n})^2 dV - \frac{1}{2} \int (\mathbf{E} \cdot \mathbf{D}) dV, \quad (I.22)$$

Dielectric tensor depends on director components as follows:

$$\hat{\varepsilon} = \varepsilon_{\perp} \delta_{ij} + \varepsilon_a n_i n_j. \quad (I.23)$$

Dictated by the chemical structure of LC molecules, dielectric anisotropy ε_a (see page 4) can be either positive, as shown in Figure I.4 (a), ($\varepsilon_{\parallel} > \varepsilon_{\perp}$) or negative, Figure I.4 (b), ($\varepsilon_{\parallel} < \varepsilon_{\perp}$).

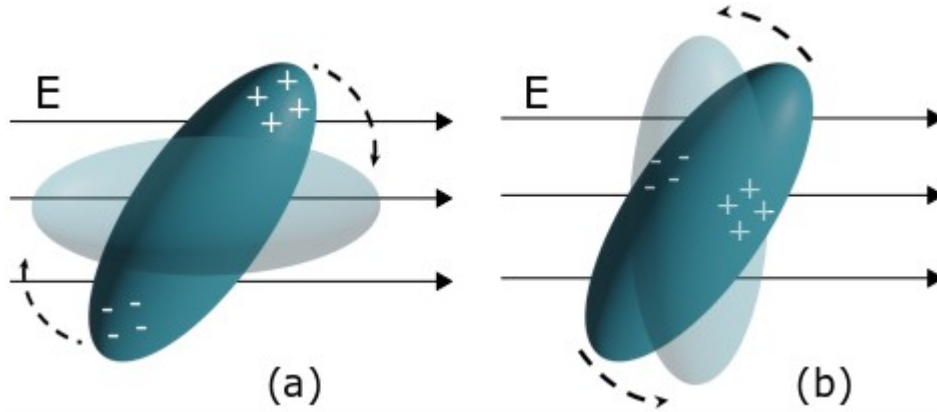


Figure I.4. Reorientation of LC molecule with (a) positive and (b) negative dielectric anisotropies in electric field.

NLCs with positive dielectric anisotropy have their dipole moments directed parallel to long molecular axis. Therefore, these molecules tend to change their orientation to be parallel to the external electric field, as this state is energetically preferable. On the other hand, NLCs with negative dielectric anisotropy (which is typical for molecules that are permanent dipoles) have dipole moments perpendicular to long molecular axis. In this case they change their orientation in such a way that director is perpendicular to electric field. In this thesis we work with NLCs that have positive dielectric anisotropy.

Let us discuss a simple case of electric field induced reorientation of NLC with positive dielectric anisotropy in a planar cell. Under the condition that LC molecules are initially completely parallel to cell substrates, there exists a threshold voltage at which molecules start changing their orientation [1]:

$$V_{th} = \pi \sqrt{\frac{(K_{11} + K_{33})/2}{\epsilon_0 |\epsilon_a|}}. \quad (I.24)$$

This process is called a Frederiks transition and was originally observed in a meniscus (formed by a plane glass and a convex glass) in magnetic field, but the equivalent effect also takes place in electric field. We see that V_{th} is independent of cell geometry and is a function of elastic and dielectric properties of LC. For $V \gg V_{th}$ the molecules become completely reoriented, with their dipole moments being parallel to the electric field. Usually the AC voltage is applied, as in DC voltage we observe the migration of charged particles to one electrode of the cell structure, damaging it eventually. Thin transparent layers of conductive materials (for example indium-tin-oxide, ITO) are deposited on glass substrates to serve as electrodes. The thickness of ITO layer is about 20 - 50 nm.

Equation (I.22) shows that there are two competing sources contributing into free energy. Elastic forces tend to keep the molecules oriented in accordance with initial, non-disturbed state. On the other side, electric field forces tend to orient the molecules to align them parallel to \mathbf{E} . Inner surfaces of LC cells are usually covered with polyamide, that is mechanically rubbed or chemically treated to create grooves. They provide nearly parallel orientation of molecules in proximity to glass substrates (planar initial orientation), defining distribution of director within the cell. Some types of polyamides make molecules nearly perpendicular to contact surfaces (homeotropic orientation).

From the point of view of electric circuits, an LC cell can be represented as a leaky variable capacitor with capacitance gradually changing from $C_{\perp} = \epsilon_0 \epsilon_{\perp} S/d$ when the cell is unpowered to $C_{\parallel} = \epsilon_0 \epsilon_{\parallel} S/d$ for a cell where LC is completely reoriented, where ϵ_0 – dielectric permittivity of vacuum, S – cell area, d – cell thickness.

It should be mentioned that dielectric constants of LCs are frequency dependent. For many mobile applications, the typical working frequency does not exceed several kHz (as it is directly proportional to power consumption), but in certain cases the use of higher frequencies is justified. An example of such a system will be presented further.

When the electric tension is switched off – a relaxation of molecules occurs, as they return to the state of original orientation. The times of molecular relaxation and excitation can be evaluated as [18]:

$$\tau_{relax} = \frac{\gamma_1 L^2}{\pi^2 K}, \quad (I.25)$$

$$\tau_{excit} = \frac{\tau_{relax}}{\left| \left(\frac{V}{V_{th}} \right)^2 - 1 \right|}, \quad (I.26)$$

where γ_1 is rotational viscosity of LC, K – elastic constant ($K \approx K_{11} \approx K_{33}$ – one constant approximation).

Dielectric and optical anisotropies of LCs as well as simple means of orientational control are widely exploited in modern optical technology. In the next section we will demonstrate the governing equations for LC reorientation within the frame of continuum theory, based on the full free energy described by Eq. (I.22).

I.5 Partial differential equations describing the reorientation of molecules

Having built free energy functional (Eq. (I.22)) we can now search for such a distribution of LC molecules under the influence of electric field, that results in a steady state. Mathematically, this is the problem of variational calculus [19], where free energy is a functional to be minimized. Finding the first variation and equalizing it to zero, we obtain the Euler-Lagrange equation. The solution of this partial differential equation (PDE) is a function that corresponds to minimum of free energy and therefore is a steady state distribution. Let us present several geometries that will be used further in this thesis.

We start with a geometry shown in Figure I.5, considering Cartesian coordinate system:

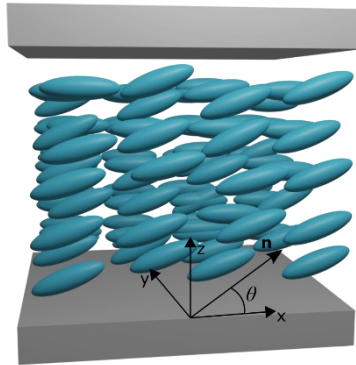


Figure I.5. Schematic representation of LC's director in Cartesian coordinates.

where the LC cell is assumed to be infinitely long in y direction. Thus, the reorientation of LC molecules takes place in xOz plane. This assumption is often made to simplify PDE, as resulting

solutions still agree well with experiments. The angle between director $\mathbf{n}(\mathbf{r})$ and x axis is θ , then director components are the following:

$$\mathbf{n} = (\cos \theta, 0, \sin \theta). \quad (I.27)$$

Then the resulting PDE for director's reorientation angle is

$$\begin{aligned} & \theta_{xx} (K_{11} \sin^2 \theta + K_{33} \cos^2 \theta) + \theta_{zz} (K_{11} \cos^2 \theta + K_{33} \sin^2 \theta) + \\ & + (K_{33} - K_{11}) [(\theta_z^2 - \theta_x^2) \sin \theta \cos \theta + \theta_{xz} \sin 2\theta] + \\ & + \varepsilon_0 \varepsilon_a (\sin \theta \cos \theta (E_z^2 - E_x^2) + E_x E_z \cos 2\theta) = 0, \end{aligned} \quad (I.28)$$

where ε_0 is the dielectric constant of vacuum, $\theta_{xx} = \partial^2 \theta / \partial x^2$, $\theta_{zz} = \partial^2 \theta / \partial z^2$, $E_x = \partial E / \partial x$.

This PDE should be accompanied by boundary conditions for θ (at $z=0$ and $z=L$). We use strong anchoring approximation, meaning that LC's director can not deviate from a certain predefined orientation at boundary surfaces $\theta(x,0) = \theta(x,L) = \theta_1$. For planar orientation, the value of θ_1 is several degrees. A different approach, that can often be found in literature, is called weak anchoring boundary condition. In this case, one more term (for example an expression proposed by Rapini and Papoular [20]), describing surface anchoring energy should be added to total free energy. Then boundary conditions would take more complex form.

A one elastic constant approximation, meaning that $K_{11} = K_{33} = K$, is widely used to simplify PDE (I.28). Under this condition, Equation (I.28) is transformed into

$$(\theta_{xx} + \theta_{zz}) + \frac{\varepsilon_0 \varepsilon_a}{K} (\sin \theta \cos \theta (E_z^2 - E_x^2) + E_x E_z \cos 2\theta) = 0. \quad (I.29)$$

When LC cell's dimension in x direction is much larger than its height (which in many cases holds true), all x derivatives and E_x field component become small and can be neglected; then Equation (I.29) further simplifies to

$$\theta_{zz} + \frac{\varepsilon_0 \varepsilon_a}{K} (\sin \theta \cos \theta (E_z^2)) = 0. \quad (I.30)$$

The other geometry used in our projects consists of a cell with top annular electrode and bottom whole transparent electrode. Given the symmetry, the choice of a cylindrical coordinate system is more suitable (Fig. I.6):

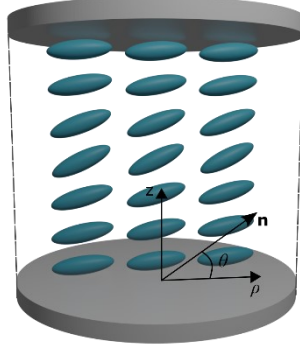


Figure I.6. Schematic representation of LC's director in cylindrical coordinates.

Director angle does not change with rotation around z axis. Applying similar procedure of variational calculus and one constant approximation, we obtain the following equation:

$$\theta_{zz} + \theta_{\rho\rho} + \frac{\theta_{\rho}}{\rho} + \frac{\varepsilon_0 \varepsilon_a}{K} (\sin \theta \cos \theta (E_z^2 - E_{\rho}^2) + E_{\rho} E_z \cos 2\theta) = 0. \quad (\text{I.31})$$

Typically, the diameter of top ring electrode is much larger than cell's height. Thus, neglecting ρ derivatives and E_{ρ} electric field component, we can simplify (I.31) to the form similar to Equation (I.30).

Having chosen the appropriate equation for director reorientation (either (I.30) or (I.28), for the problems that we worked on), we needed to couple it with Maxwell's equations. Considering only the influence of electric field and assuming no free charges present in LC, Maxwell's equations simplify to the equation for electric potential:

$$\nabla \cdot \left(\left(\varepsilon_0 \hat{\varepsilon} + i \frac{\sigma}{\omega} \right) \nabla V \right) = 0, \quad (\text{I.32})$$

where $\hat{\varepsilon}$ is a dielectric tensor as given by Equation (I.23). Boundary conditions for this equation are chosen individually for each problem, corresponding to the applied control voltage.

The system of coupled PDEs for director reorientation and electric field distributions are solved numerically using finite difference method. Calculated director configuration is then used to estimate optical response of the LC system.

Several approximations and simplifications in the choice of equations are necessary because full 3D problems are often computationally demanding. Moreover, for the LC systems considered within this project, these simplifications have proved to give solutions that agree well with experimental data. The results of numerical simulations enable us to quickly improve experimental

samples, as optimal control parameters and geometry can be found in advance. Overall behavior of experimental systems can be analyzed, permitting us to focus experimental part of the research on the most promising designs.

I.6 Optical phase retardation in nematic liquid crystals

Let us consider a planar LC cell with linearly polarized light normally incident on it. Optical axis is parallel to director. Depending on the orientation of LC molecules the beam experiences different refractive indices. Optical path for the beam passing LC cell of thickness L , as demonstrated in Figure I.7 (a) is $n_e L$, when for situation depicted in Figure I.7 (c) it is $n_o L$.

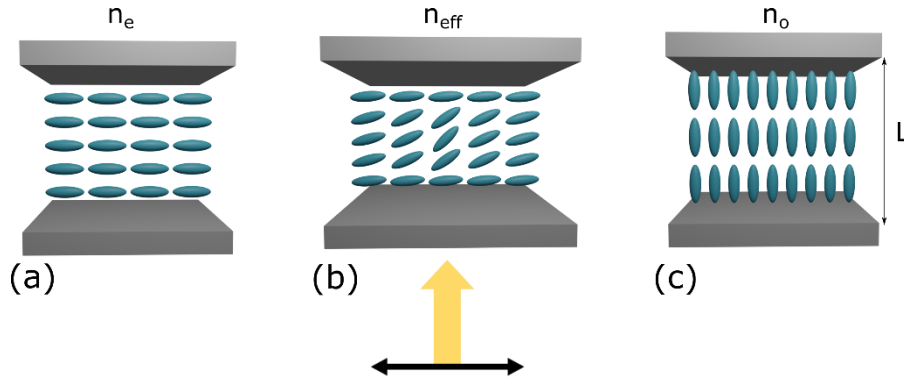


Figure I.7. Dependence of refractive index encountered by incident beam on director orientation (black arrow – direction of polarization, yellow arrow – direction of propagation).

When director makes an angle with beam's polarization direction (Figure I.7 (b)), the effective refractive index is

$$n_{eff} = \frac{n_o n_e}{\sqrt{n_e^2 \cos^2 \theta + n_o^2 \sin^2 \theta}}, \quad (I.33)$$

as it was shown in section I.3.

Because ordinary and extraordinary beams face different refractive indices, there will be a phase retardation between them, that can be calculated as

$$\varphi = \frac{2\pi}{\lambda} \int n_{eff}(x, y, z) dz. \quad (I.34)$$

It is possible to create such a distribution of effective refractive index that phase profile of extraordinary beam at the exit from the LC cell will be similar to that of a beam passing through an ordinary lens. Numerous techniques providing electric field modulation within LC cell to create

gradual variation of refractive index exist. Moreover, as molecular orientation is controlled with application of voltage, we can change the shape of final phase profile, varying optical power and aberrations as well.

Many designs of adaptive liquid crystal lenses have been presented in recent years. In the following sections we will briefly discuss the evolution of adaptive LC optics and show several examples of these designs. Then we will introduce the designs that have been investigated during this project and that will be discussed in detail in the subsequent chapters of this thesis.

I.7 Overview of existing tunable liquid crystal lens designs

Tunable lenses have always been of great interest because they have numerous applications not only in scientific domain, but in everyday use devices as well (phone cameras, web cameras, etc.). Today we know various approaches to create a tunable lens, starting from a straightforward mechanical displacement of an ordinary lens, ending with liquid lenses formed within elastomeric membranes. Although some optical systems use these types of lenses, there exists an even more elegant approach of liquid crystal-based tunable lensing. We may notice that existing tunable lenses often mimic eyes of wild birds or animals. For example, some bird species have the ability to deform their eyes [21] to focus on prey or other particular objects of interest. On the other hand, we have liquid lenses that achieve the change of optical power via variation of elastic transparent membrane's curvature when a liquid is injected or pulled out. Another possibility is to deform a drop of liquid using electrowetting effect [15].

However, the approach of liquid crystal tunable lenses stands out. These lenses have visible advantages: exclusion of mechanical movement, easy control, relatively simple fabrication, low cost and high image quality. A simple LC cell can act as a lens if we shape the electric field in such a way that it creates parabolic distribution of LC director within the cell. This leads to a parabolic distribution of effective refractive index. Thus, a plane linearly polarized wave acquires spherical phase retardation as it passes through the cell. Depending on the distribution of molecules we can equally create lenses with negative or positive optical powers. As the reorientation of molecules varies gradually with the application of voltage – we achieve controllable change of focal distance. The concept of liquid crystal lenses was developed by S. Sato. In one of his first papers dedicated to this subject he described the possibility of making switchable lenses using LCs (Fig. I.8) [22].

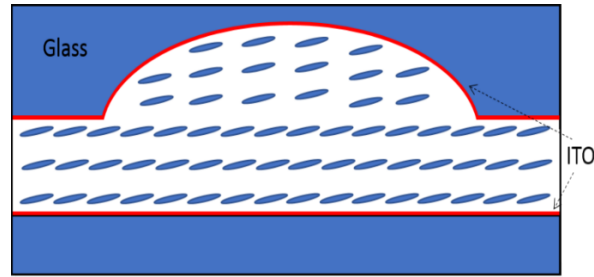


Figure I.8. One of the first LC lens designs [22].

In this case the lens consisted of a flat and a concave glass substrates covered with transparent electrodes (ITO). The gap in between them was filled with LC, which enabled shifting between two focal points as voltage was turned on or off.

Tunable liquid crystal lenses have greatly evolved over the past decades, overcoming many limitations of other types of adaptive lenses (slow response, high aberrations, gravitational effect in case of liquid lenses). This field remains competitive, as new designs of liquid crystal lenses emerge. All LC based lenses can be divided into several categories [23], for example: curved lenses (shown in Fig. I.8), gradient index (GRIN) lenses (Figures I.9 and I.10), composite lenses (combinations of curved and GRIN types), Fresnel lenses (Figure I.11). The difference among designs is defined mainly by the means of shaping the electric field inside the LC cell. Let us take a closer look at several designs representing different categories.

There are many variations of GRIN LC lens designs. This type of lenses usually involves the presence of a supplementary layer, which shapes the electric field. This could be, for example, a layer of dielectric fabricated in such a way that its permittivity decreases quadratically from the center to the periphery. One of the first LC-based GRIN lenses was reported by Sato, Figure I.9 [24].

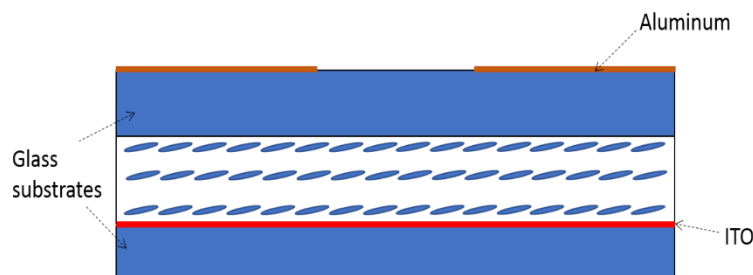


Figure I.9. GRIN LC lens with a hole-patterned electrode [24].

In this case the top electrode (made from ITO or aluminum) has a hole pattern of predefined diameter. Inner surfaces of the cell are covered with polyimide (not shown in Fig. I.9). The polyamide layers were rubbed in anti-parallel directions to ensure homogenous alignment of molecules. An intermediate upper glass substrate (located right below hole patterned electrode) ensures gradual drop of electric field potential, which decreases from the edge of the aperture towards the center. This, in turn, creates parabolic distribution of director's orientation. However, in the absence of additional glass layer, we would observe an abrupt change in electric potential close to the edge of circular electrode and the lens would not function properly, as the formation of disclination lines (defects) would be highly probable. The advantages of this design are the simplicity of photolithography and the possibility of creating LC lenses of relatively large aperture sizes (the lens of 7 mm diameter was characterized by Sato). However, the operating voltages for this design remain rather high [25] due to the glass layer that softens electric field.

One of the simplest ways to create a parabolic electric potential distribution is to use a curved electrode. Such a design, demonstrated in Figure I.10 was published by Wang et al [26]:

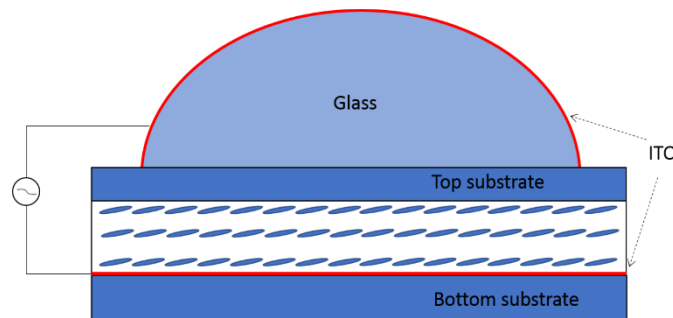


Figure I.10. Schematics of an LC lens with a curved electrode [26].

The lens consists of a standard LC cell with initial planar alignment and a plano-convex glass lens in contact with one of the cell's substrates. The convex surface of the glass is covered with a thin transparent conductive ITO film. The opposite inner side of the cell is coated with ITO as well. Polyamide layers deposited on the inner walls of the cell were mechanically treated to provide initial orientation of director. When voltage is applied to the electrodes, we observe more director reorientation at the periphery of the glass lens (as we have higher values of electric potential in these areas due to proximity of top electrode). Director's reorientation gradually decreases from the periphery towards the center of the cell at fixed applied voltage. Resulting device acts as a tunable lens. It is worth noticing that even when no voltage is applied, this system will still be focusing light, as its total optical power is the sum of optical power coming from a glass lens and variable optical

power from LC cell. Initial focal distance (at $V=0$) is defined only by contribution from the plano-convex lens. When voltage is increased – LC starts reorienting, increasing total optical power. As voltage is increased further, director becomes reoriented not only at the edge of the aperture but in the center as well, thus decreasing optical power coming from LC cell. One of the main drawbacks of this design is residual optical power in ground state. Also, relatively high voltages are required for operation.

A common problem faced by LC lenses is their inability to achieve high optical powers for a wide aperture (> 4 mm) and maintain other characteristics simultaneously (low scattering levels, low aberrations, fast reorientation). One possibility to increase the optical power is to make thicker LC cells, because it is directly proportional to cell's height. But this solution comes with some tradeoffs, such as larger excitation times and increasing scattering. However, certain designs enable us to obtain higher optical powers, preserving normal excitation times and image contrast.

A concept proposed by the group of Bos [27] adapts a well-known approach of refractive Fresnel lens (Figure I.11).

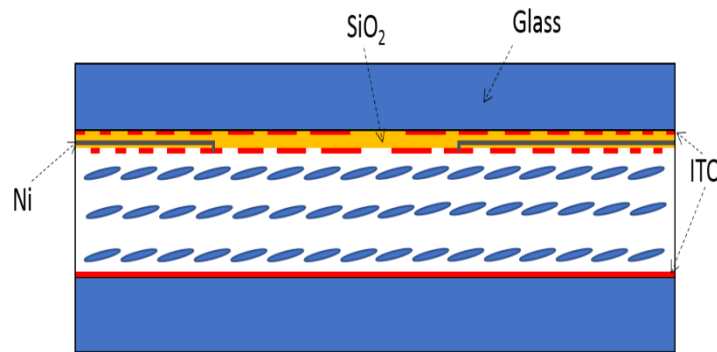


Figure I.11. Scheme of refractive Fresnel lens described in [27].

First, a glass substrate is covered with concentric ITO rings of equal areas separated by gaps using photolithography. Every pair of neighboring ring electrodes is connected with a resistor that serves to decrease electric potential, propagating from one electrode to the other. The first layer of patterned ITO is then covered with dielectric (SiO_2) in which openings are made to connect to external bus lines by means of nickel deposition and patterning. In total, the first substrate has 288 ring electrodes, several of them are directly connected to bus line electrodes (see Ni in Figure I.11). Then a new layer of dielectric is deposited, insulating the first layer of ITO and bus line connections. Finally, the second layer of ITO is deposited and patterned to form concentric rings that are slightly shifted relative to the first layer. Inner surface of the second substrate is covered with one layer of

ITO that serves as common ground. Both substrates are then covered with polyamide, rubbed in antiparallel directions, and glued together.

Application of voltage to bus line connections creates an abrupt reorientation of LC director in certain parts of the lens, where ring electrodes are connected directly. Electric potential drops on interelectrode resistors until another electrode with direct connection appears, causing another jump of potential. In such a way it is possible to obtain the phase pattern with several phase resets, resembling the one of a conventional Fresnel lens, where similar phase profile is achieved by means of relief structures.

Creating phase resets the authors managed to obtain desired optical power and maintain fast reorientation of the lens, but the fabrication process is complex and involves several steps of photolithography and deposition. Resulting device is a switchable Fresnel lens.

Although a great number of LC lens designs have been reported, they all possess some limitations. It is often required to have a large diameter lens, but the maximal achievable optical power of an LC lens decreases quadratically with the increase of clear aperture's radius. In order to have a wide dynamic range of optical powers we need a big difference of phase retardation between central and peripheral portions of the lens. It can be obtained if we increase the cell's thickness, but then the response times will increase as well. Another problem that comes with making thicker LC cells is scattering, which degrades contrast and resolution. The important aspect for mobile applications is power consumption. Therefore, designs that require high voltages might be inappropriate.

It is preferable to have a simple experimental procedure for lens assembly, because every additional step increases unit price. LC lenses are polarization dependent, unless the final device is composed of two lenses with one having rubbing direction turned 90 degrees relative to the other. Finally, the aberrations should be minimized to provide the best image quality.

It is rather challenging (almost impossible) to create a design that would overcome all the above-mentioned limitations. On the other hand, we can find good application targeted solutions. In the next section we will describe the lenses that have been broadly studied in this thesis. They proved to have some advantages in comparison with existing concepts, which will be further discussed in detail.

I.8 Description of hidden layer and modal control lenses

Our study explores two designs of LC lenses. In this section we are presenting the physics of their operation, referring to theory from the previous sections. Here we are focusing on key mechanisms of their functioning, as full descriptions, design modifications, theoretical models, and experimental characterizations (where applicable) will be demonstrated in the next chapters.

The first concept that we investigated uses dielectric dividing principle. The schematic representation of this device is shown below (Figure I.12, plane x, z cross-section; the axes x and z are aligned parallel and perpendicular to the cell substrates, respectively).

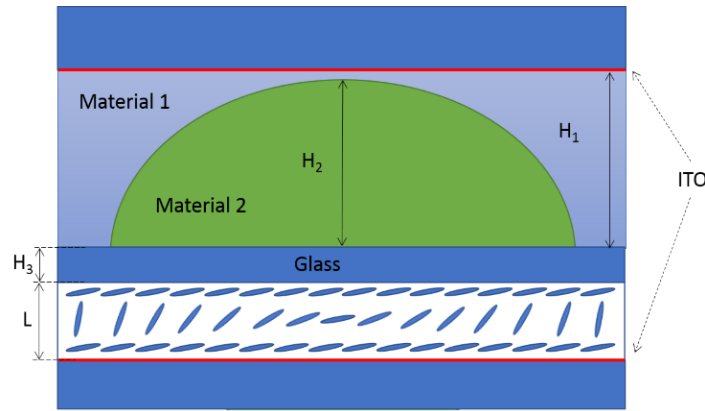


Figure I.12. Schematics of a hidden dielectric double layer lens [28].

It consists of the following materials and layers: three glass substrates (top, middle, and bottom), two of them (top and bottom) are covered with transparent conductive electrodes (ITO), facing each other inside of the structure. A planar oriented NLC layer of thickness L is sandwiched between the middle (with thickness H_3) and bottom substrates, both bearing rubbed alignment layers (polyimide) (not shown in the Figure I.12).

The top and middle substrates contain a dielectric doublet structure that is made out of two transparent dielectrics (materials 1 and 2) that have different relative permittivity $\epsilon_1 \neq \epsilon_2$ at low electric frequencies (e.g., 1 kHz), but similar optical refractive indices $n_1 = n_2$. This makes the doublet structure optically invisible (hidden), thus eliminating light reflections (from the interface between those two materials) without the use of anti-reflection coatings.

Any electric potential difference V , applied to ITO layers, is divided into two vertical sections of drop of potential ($V = V_1 + V_2$), that would be different at various points of space if we move our

observation point in the horizontal direction (see Fig. I.12). Indeed, the values of V_1 and V_2 are defined by the dielectric constants (ϵ_1, ϵ_2) and the thicknesses of two dielectrics (H_1, H_2), [29,30]. Thus, for given materials, the electric field inside of the NLC layer has different values (when moving in the horizontal direction) depending upon the local ratio of the thicknesses of materials 1 and 2. Consequently, the electric field transforms (via the dielectric torque, [9]) the initial uniform orientation (Figure I.13 (a)) of the director into a non-uniform one (Figure I.13 (b)).

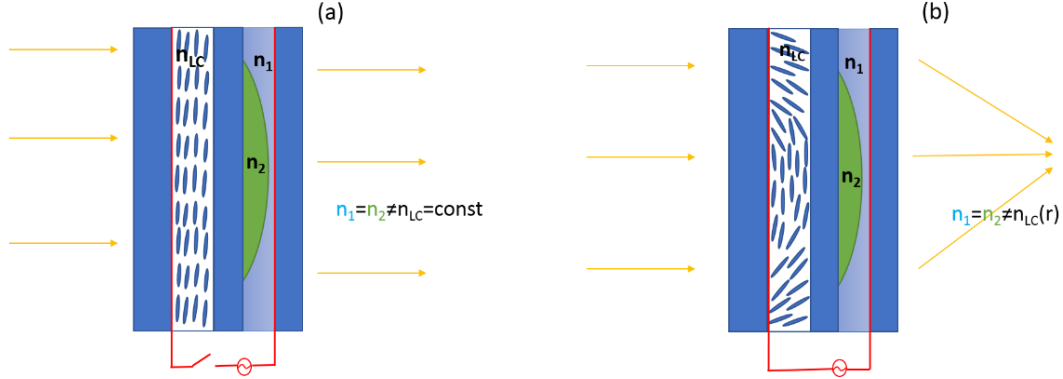


Figure I.13. Schematic demonstration of the hidden layer LC lens with (a) zero control voltage and (b) applied voltage.

Thanks to the optical anisotropy of the NLC, this nonuniform distribution of the director results in an inhomogeneous refractive index profile, defined by the profile of the dielectric doublet hidden layer (e.g., parabolic). Most importantly, the optical hiding of two dielectric lens structures (by index matching) decouples its optical and electrical functions, thus allowing the generation of dynamically variable phase profiles (including non-parabolic) without taking care of the static optical aberrations that the doublet structure might generate otherwise.

Thus, the probe beam of an extraordinary polarization mode (in the plane of drawing), propagating from left to right, will be focused if $\epsilon_1 > \epsilon_2$, and if the optical and dielectric anisotropies of the NLC are positive. At the same time, the ordinary polarized probe component will maintain its uniform phase front. The phase lag of the extraordinary polarized wave in the center of the lens with respect to its value in the periphery of the lens varies with different applied voltages, so the optical power of the lens (the inverse of focal distance) is electrically controllable, Figure I.13 (b). This approach enables obtaining nonuniform electric fields of almost arbitrary form while using planar ITO layers. In addition, the use of two dielectrics may enable achieving a very high contrast of dielectric permittivity ϵ_1/ϵ_2 [30]. For instance, material 1 may be a water-based solution with a relatively high dielectric constant $\epsilon_1 \approx 78$ at low electric frequencies (in the 1 kHz range, typically

used to drive the LC devices) and a predetermined value of its dielectric constant at high optical frequencies (defining the value of $n_1 \approx 1.3$). Then, an example of material 2 could be from the family of fluorinated polymers [30] that has a similar (to the material 1) refractive index $n_1 \approx n_2$, but quite different (smaller) low-frequency dielectric constant $\epsilon_2 \approx 3$.

The described structure is obtained by sandwiching the above mentioned dielectric doublet between the top and mid substrates [30]. Then the obtained “laminated” structure is used as a substrate to build an NLC cell with the help of the bottom substrate (Figure I.12). This design has zero optical power ground state, flat LC cell with simple flat electrodes, no light reflections on material interfaces and control voltages comparable with existing LC lenses.

Let us now address a different design of LC lenses that was investigated and improved within the framework of this thesis. This lens offers an alternative and promising approach, using the concept of modal control (MC). Initially published by Naumov [31], the MC design has been thoroughly discussed in literature [31–34]. Just as in the case of a double dielectric hidden layer, this approach uses a uniform LC cell. The LC is placed (Figure I.14) between one uniform transparent electrode (UTE, typically made of ITO) and one hole patterned electrode (HPE).

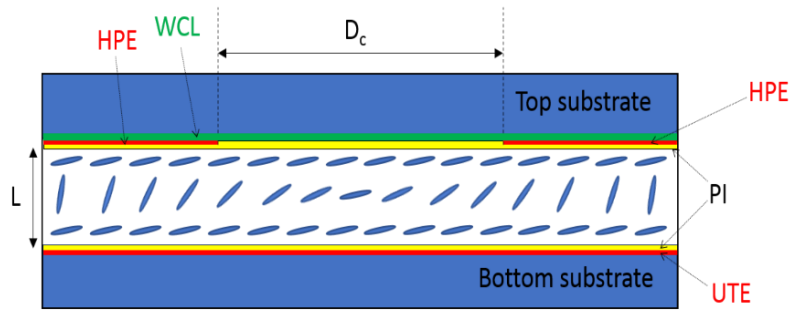


Figure I.14. Geometry of a tunable modal control lens [31]. D_c – diameter of the controlling hole patterned electrode (HPE), WCL – weakly conductive layer, PI – polyimide alignment layer, L – thickness of the LC layer, UTE – uniform transparent electrode.

A highly resistive or weakly conductive layer (WCL) is added to the HPE (Figure I.14) to soften the spatial (along the x axis) variations of electric field and to limit optical aberrations. The fundamental mechanism of the electric field’s spatial shaping in these lenses is based on the combination of electrical capacitive and resistive properties of the LC cell [33,35]. The LC cell represents an equivalent distributed capacitance in parallel with resistance, when WCL represents distributed resistance connected in parallel (Figure I.15):

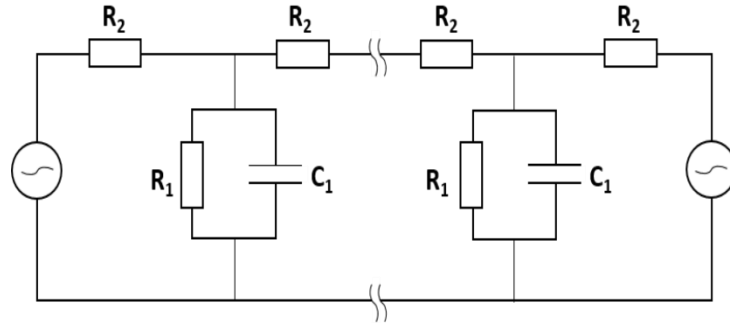


Figure I.15. Equivalent electric circuit of the MC lens [31].

The reactive impedance of LC and active impedance of WCL create a voltage divider that gives the electric field a nearly parabolic shape [31]. The drop of voltage is defined by dielectric properties of LC, sheet resistance of WCL, geometry of the top control electrode and frequency of applied signal. Thus, we have two parameters (voltage and frequency) to tune optical power. Moreover, it is possible to find an optimal set of voltages and frequencies that would minimize aberrations [32].

The main advantages of this design are simple (one step) photolithography and possibility of controlling optical power variation with both voltages and frequencies. On the other hand, the resulting wavefront generated by such a lens is not perfectly parabolic. It has been experimentally demonstrated that image quality can be significantly improved by adding a floating disk electrode onto the top substrate [36,37]. This step does not overcomplicate fabrication and provides great aberration reduction. Moreover, other modifications of this design lead to even better wavefront control, correcting it to nearly parabolic form within the entire aperture.

I.9 Goals and motivation

Despite wide integration of LC tunable lenses into optical systems, certain challenges remain. They usually require a compromise solution, depending on specific application. LC lenses are polarization dependent; therefore, two lenses need to be stacked together (having their rubbing directions crossed at 90 degrees) to avoid this issue. Unfortunately, this complicates the assembly and raises the problem of focus mismatch. A solution explored today is the use of blue phase LCs [38,39]. The optical powers need to vary continuously within achievable range (for zoom and autofocus applications), when some designs provide only on-off regimes. At the same time, large aperture LC lenses (for augmented reality, ophthalmology) need to have sufficient dynamic optical power ranges. This is problematic because the increase of clear aperture leads to decrease of optical power. Other

requirements imposed by optics industry include low aberrations, reasonable power consumption and small response times.

We have addressed some of these issues, suggesting completely new designs (hidden layer lens [28,30] and microscopic structures [40], modal control Fresnel lens [41]), or modifying and improving existing ones (modal control lens with additional electrodes [36,37,42]). Our goal was to develop LC lenses, which would have simple fabrication, continuous variation of optical power and the best possible image quality. All our designs have homogenous cell gaps (avoiding complex surface treatment for orientation of director), flat electrodes (made with a minimal number of photolithography steps), simple drivers (which lowers overall cost of the lens). Nevertheless, the image quality that our lenses can provide is comparable with existing commercially available LC lenses.

The hidden layer LC lens has been patented [43] and implemented in mobile telephone cameras. It can achieve the maximal optical power of 10 D, maintaining autofocus time < 1 sec [30]. The lens is polarization dependent, but the assembly of two lenses is still very thin (0.5 mm) and creates no problems for smart phone integration.

Conducted theoretical analysis [44] of this lens explores the limits of the design regarding geometrical parameters, material parameters and environmental dependence. In another study we theoretically extrapolated the use of optically hidden dielectrically dividing layer to creation of microlens and microprism arrays [40]. Electrically controllable microlenses are crucial for production of switchable autostereoscopic displays [15], when tunable microprisms are used for light steering [45].

The theoretical analyses of modified modal control lens showed the opportunity of significant aberration reduction [37,42]. Indeed, the lens implemented in a mobile camera [37] demonstrated good performance in comparative tests with commercial devices. Using the algorithm developed specifically for LC lenses [46] it could achieve faster autofocus than traditional approaches (including voice coil motor (VCM) based lenses).

Another important field of MC LC lens applications is medical domain: endoscopy [47,48] and ophthalmology [42,49]. Wavefronts formed by LC lenses often have severe deviations from spherical shape in proximity to electrode (peripheral portion of aperture). For most uses the solution would be to hide this part of the wavefront covering it with a diaphragm. But this is unacceptable for ophthalmology, as the entire clear aperture, with no obscurations, needs to be used. In our work we

suggested a modification of conventional MC lens approach, which enables wavefront correction in this area. At the same time, proposed design provides low aberrations in compliance with medical requirements.

Lastly, we developed a new Fresnel modal control lens design [41]. The first prototype showed increased maximal optical power in comparison with conventional MC lenses. Although, measured aberrations were rather high, we theoretically showed that it is possible to lower them using optimized control (combinations of voltages and frequencies). The concept of Fresnel lens in combination with modal control principle provide the increase of maximal optical power for large aperture LC lenses (6 mm), avoiding the use of thicker cells and all accompanying issues.

All designs demonstrated further in this thesis were developed targeting mobile imaging, beam control and medical applications. Any variable lens brings MTF degradation into optical system [6], thus it is impossible to find a perfect design of a tunable lens. However, every approach considered in the following chapters has certain advantages for specific use.

Chapter 1 Theoretical analyses of a liquid crystal adaptive lens with optically hidden dielectric double layer

Oleksandr Sova^{1,2}, Victor Reshetnyak¹ and Tigran Galstian^{2,3,*}

¹Physics Faculty, Taras Shevchenko National University of Kyiv, Volodymyrska Street 64, Kyiv 01601, Ukraine

²Université Laval, Département de physique, de génie physique et d'optique, Center d'optique, photonique et laser, Pavillon d'Optique-Photonique, 2375 Rue de la Terrasse, Québec G1V0A6, Canada

³LensVector Inc., 6203 San Ignacio Ave. Suite 110, San Jose, California 95119, USA

*Corresponding author: galstian@phy.ulaval.ca

Journal of the Optical Society of America A, Vol. **34**: pp. 424–431, 2017

Tunable liquid crystal lens with hidden dielectric double layer is the first design that we investigated during this doctoral project. The present chapter is based on a manuscript published in the Journal of the Optical Society of America A. Theoretical background given in the introduction is implemented for numerical simulations in this study. Operation mechanism of this approach is explained using simplified dielectric division scheme.

Our theoretical study explores the limits of this lens by simulating systems with varying geometric and material parameters. We explain, compare, quantify, and discuss the influence of every modification made to the original lens [28,30]. The simulations showed that optimization of certain parameters is possible in order to achieve wider range of dynamic optical powers.

A case considering the impact of dielectric permittivities of materials forming the hidden layer was studied. We have shown the possibility to create a similar system using double dielectric layer materials with the same permittivities but considerably different conductivities. Temperature dependence of the optical power provided by this lens was calculated.

This is an interesting and promising design which uses a flat uniform liquid crystal cell and flat electrodes simplifying manufacturing. These lenses have demonstrated sufficient optical powers to perform mobile imaging tasks.

1.1 Résumé

Analyses théoriques d'une lentille adaptative à cristaux liquides avec une double couche diélectrique optiquement cachée

Dans cette étude nous faisons l'analyse théorique des tendances de performance d'une lentille à cristaux liquides basée sur le principe de la double couche diélectrique optiquement cachée. Nous démontrons des moyens possibles d'optimiser la lentille en fonction des paramètres des matériaux et des paramètres géométriques utilisés. L'impact des constantes diélectriques relatives, des conductivités et des dimensions des composants de la couche diélectrique cachée, ainsi que l'épaisseur et la température du matériau de cristaux liquides sont démontrés. Les compromis correspondants sont brièvement discutés.

1.2 Abstract

In this work we theoretically analyze the performance trends of a liquid crystal lens based on the optically hidden dielectric double layer principle. We demonstrate possible ways to optimize the lens as a function of the material and geometric parameters used. The impacts of relative dielectric constants, conductivities, and dimensions of the components of the hidden dielectric layer, as well as the thickness and the temperature of the liquid crystal material, are demonstrated. Corresponding trade-offs are briefly discussed.

1.3 Introduction

Among many electrically variable lens solutions available today [6], tunable liquid crystal lenses (TLCLs) represent an approach that enables the lowest power consumption (at the order of 10 μ W) and manufacturing cost [50], while also imposing some trade-offs, particularly related to optical performance (e.g., optical aberrations). Indeed, most TLCLs are designed to obtain spherical wave fronts with electrically variable curvature and a significant effort must be devoted to minimize the wave front errors (deviations from the spherical form [36]). However, in some applications, other types of dynamic wave fronts (e.g., aspheric or prism-like) may be required. The challenge here is to ensure that the ground state (default mode, when the voltage is switched off) of the element is optically neutral. This means that we have to “decouple” the dynamic wave front modulation function from the ground state optical properties of the TLCL. An interesting TLCL design that can perform such a decoupling was suggested [51]. However, this design uses curved electrodes that are not desirable from a manufacturing perspective. An alternative design was introduced later that was based on the use of a “double dielectric optically hidden” (DDOH) layer [28,30]. This TLCL can dynamically generate arbitrary predetermined wavefronts without compromising the optical quality in the ground state of the lens, using uniform (flat) electrodes and liquid crystal (LC) layers. Figure 1.1 schematically shows the design of such a TLCL.

The bottom substrate 1 of the LC cell is a simple substrate (e.g., glass) that is coated with a uniform transparent electrode (often indium tin oxide, ITO), while the top substrate is a laminated sandwich of a DDOH layer between two substrates (2 and 3), only the upper of which (substrate 3) bears a uniform electrode (ITO). In the simplest implementation, the DDOH layer is composed of a lens-like material 2 (we call it a core lens (CL)) and of a surrounding material 1 that is an optically index matched layer (IML). Those materials (1 and 2) have the same dielectric constants at optical frequencies $\epsilon_1(10^{14} \text{ Hz})=\epsilon_2(10^{14} \text{ Hz})$. Thus, the doublet structure is optically hidden (since they have the same refractive indices $n_1=n_2$, in contrast with [29]).

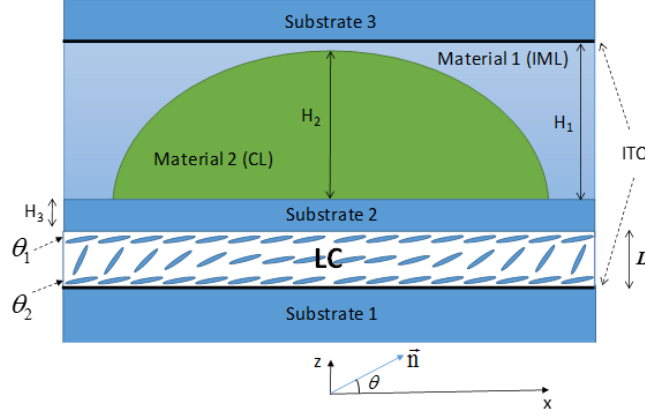


Figure 1.1. Schematic of the DDOH layer lens [30].

However, those materials are chosen to possess different dielectric constants at low frequencies $\epsilon_1(10^3 \text{ Hz}) \neq \epsilon_2(10^3 \text{ Hz})$, which are typically used to dynamically reorient LC molecules [1,9]. This property (along with the principle of voltage division, discussed later) is used to build the non-uniform electric field inside the LC layer (while applying uniform ITO electrodes). Indeed, as illustrated in Figure 1.2, the drop of the electric potential U (that is, creating the voltage applied between top and bottom ITO electrodes), will be split into drops of potentials U_1 and U_2 on those two dielectrics, depending upon the ratio of dielectric constants (ϵ_1, ϵ_2) and local (along the x axis, Figure. 1.1) thicknesses (d_1, d_2).

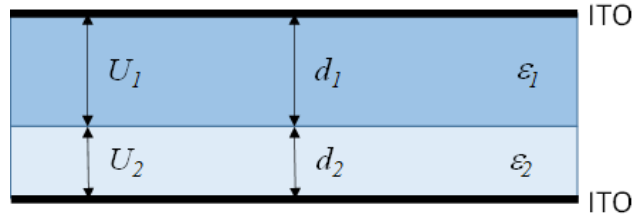


Figure 1.2. Schematic of the dielectric divider concept.

Thus, the voltage applied, for example, to material 2 would be expressed [30] as

$$U_2 = \frac{U}{\left(1 + \frac{\epsilon_2 d_1}{\epsilon_1 d_2}\right)}. \quad (1.1)$$

We can thus easily imagine (referring to Figure 1.1) that the spatial shape (along the x axis) of the interface between those two dielectrics (1 and 2) would define the profile of the electric field inside the LC layer (since the local potential drop U_{LC} on the LC will be defined by the local potential drops on materials 1 and 2 and on substrate 2). Thus, the DDOH layer can be designed to have any

desired form, ranging from spherically symmetric to a prism-like structure. The voltage split will then enable the dynamic formation of a corresponding LC reorientation pattern (for example, to create a prism), while the entire structure will always appear as an optically uniform laminated plate in the ground state (when $U=0$) as a result of the optical hiding condition $n_1=n_2$. Let us emphasize that all these properties are achieved by using uniform transparent electrodes and uniform LC layers, which is an important advantage from a manufacturing point of view. Those advantages (neutral default state, arbitrary wave forms, and easy manufacturing) make these lenses very attractive.

Such lenses (using DDOH layers) have been fabricated and characterized [30] (see, e.g., Figure 1.3), followed by a brief theoretical analysis [28].

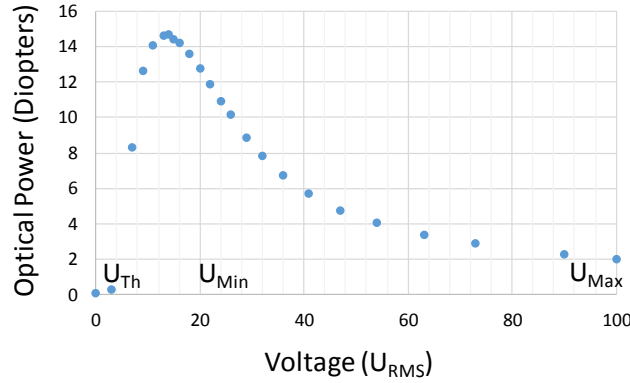


Figure 1.3. Example of experimentally measured dependence of OP of the lens versus the applied RMS voltage. U_{th} , U_{min} , and U_{max} are the threshold, minimum, and maximum considered voltages, respectively.

In the particular case of the spherical interface between materials 1 and 2, the final “accumulated” drop of the potential on the DDOH layer creates an electric field profile inside the LC cell that generates a corresponding reorientation of LC molecules (Figure 1.1). Such reorientation may create a dynamic gradient index lens with spherical wavefront retardation. The optical power (OP) can be approximated [6,15] as

$$OP = 2 \cdot \frac{\Delta n \cdot L}{r^2}, \quad (1.2)$$

where the OP (measured in diopters (D) or inverse meters (1/m)) is the inverse of the focal distance F of the lens (measured in m), r is the radius of the clear aperture, Δn is the difference of effective refractive indexes between the center ($x=0$, Figure 1.1) and the periphery ($x=\pm r$, Figure 1.1) of the lens, and L is the thickness of the LC layer.

It was demonstrated in [30] that, in the case of $\varepsilon_1(10^3 \text{ Hz}) > \varepsilon_2(10^3 \text{ Hz})$, as well as positive dielectric and optical anisotropies of the LC material used ($\Delta\varepsilon_{LC}(10^3 \text{ Hz}) > 0$ and $\Delta n_{LC}(10^{14} \text{ Hz}) > 0$), the electric field and the corresponding reorientation of LC molecules are stronger at the periphery of the lens (Figure 1.1). Such lenses generate positive (focusing) OP at voltages just above the experimental threshold voltage U_{th} (Figure 1.3). However, light scattering and optical aberrations are rather high just above the threshold. That is why there is a minimal voltage U_{min} starting from which the focusing properties of the lens may be practically used. Further increase of the voltage gradually reduces the OP since the molecules of LC also start to be reoriented in the areas close to the center of the lens ($x=0$), which clearly reduces the optical path difference between the central and peripheral optical rays. In this way, the dynamic range of the focal tuning (or the dynamic variation range of the OP) is defined by the difference of OPs for U_{min} (corresponding to the maximal OP) and U_{max} (corresponding to the minimal or “residual” OP), the latter being defined by the acceptable maximal voltage that can be used to generate an almost uniformly reoriented LC layer and, thus, the lowest possible OP. In some cases, another type of residual OP may be present (in the ground state, $U=0 \text{ V}$) if the index matching (between materials 1 and 2) is imperfect or if the lens is deformed (there are no such contributions in the TLCL example shown in Figure 1.3).

The obtained results were very interesting [28,30]; however, there was no detailed study of how various design parameters might influence the performance of the lens. For example, it is obvious that the insertion of the DDOH layer increases the distance between the top and bottom electrodes (see H_1 in Figure 1.1), which thus increases the required operating voltages. A legitimate question then occurs: can we use stronger contrast of dielectric constants $\varepsilon_1/\varepsilon_2$ (at 10^3 Hz) and reduce the H_1 ? Similarly, if we apply the dielectric division concept (see Eq. (1.1)) to the entire structure of the lens, can we reduce the required voltages by increasing the relative thickness (L) of the LC? This work intends to fill that gap and to establish the tendencies, limits, and optimal operation conditions of such lenses. In fact, the theoretical tool that we have developed in this work may also be used to estimate manufacturing tolerances and define optimal TLCL parameters for specific applications.

1.4 Theoretical simulation of the lens geometry variations

A detailed description of the theoretical approach that we use is given in our previous article [28]. Everywhere in the present work, unless stated otherwise, the initial (or reference) parameters (dimensions, permittivity, conductivities, dielectric anisotropy, etc.) are those used in experimental and theoretical works mentioned above (see also Table 1.1) [28,30]. Those experimental parameters were optimized to target the application of TLCLs in miniature phone cameras (with small clear

apertures of 1.5 to 2 mm). A two-dimensional cylindrical LC lens is considered. We assume strong anchoring of the LC director (the average orientation of long molecular axes of the NLC [1]) near glass substrates 1 and 2. The following system of coupled second order partial differential equations, describing the electric potential and director orientation distribution (in the xOz plane), is solved numerically:

$$\begin{aligned} & \theta_{xx}(K_{11} \sin^2 \theta + K_{33} \cos^2 \theta) + \theta_{zz}(K_{11} \cos^2 \theta + K_{33} \sin^2 \theta) + \\ & + (K_{33} - K_{11}) \left[(\theta_z^2 - \theta_x^2) \sin \theta \cos \theta + \theta_{xz} \sin 2\theta + \theta_x \theta_z \cos 2\theta \right] + \\ & + \varepsilon_0 \varepsilon_a \left(\sin \theta \cos \theta (E_z^2 - E_x^2) + E_x E_z \cos 2\theta \right) = 0 \end{aligned} \quad (1.3)$$

$$\begin{cases} \nabla(\hat{\varepsilon} \varepsilon_0 \nabla U_{re}) - \frac{\sigma}{\omega} \nabla^2 U_{im} = 0 \\ \nabla(\hat{\varepsilon} \varepsilon_0 \nabla U_{im}) + \frac{\sigma}{\omega} \nabla^2 U_{re} = 0 \end{cases}, \quad (1.4)$$

where θ is the director reorientation angle in the xOz plane, K_{ii} ($i=1, 3$) are the elastic constants of LC, U_{re} and U_{im} are the real and imaginary components of electric potential, respectively, $\hat{\varepsilon}$ is the permittivity tensor, σ is the material conductivity, and ω is the angular frequency of the electric field. The corresponding boundary conditions are presented in Equation (1.5):

$$\begin{cases} \theta(x, z=0) = \theta_2 & U(x, z=0) = 0 \\ \theta(x, z=L) = \theta_1 & U(x, z=L+H_1+H_3) = U_0 \end{cases} \quad (1.5)$$

Some of simulation parameters are listed in Table 1.1.

Table 1.1. Experimental parameters used hereafter as reference for simulations.

	Value	Description
L	40 μm	LC layer thickness
H_1	195 μm	Height of IML (H_{IML})
H_2	185 μm	Height of CL (H_{CL})
H_3	100 μm	Thickness of the glass substrate 2
d_a	1.75 mm	Lens aperture diameter
$\theta_1 = \theta_2$	2.5°	Pretilt angle (planar orientation)
K_{11}	21.5 pN	Splay elastic constant
K_{33}	23.9 pN	Bend elastic constant
U	20-40 V _{rms}	Range of applied voltages (sinusoidal)
ν	0.1 kHz, 0.5 kHz, 1 kHz	Frequencies used to drive the lens
λ	632.8 nm	Wavelength of the probe beam
T_{test}	20 °C	Temperature of the lens during tests.

Before discussing the impact of various physical parameters of the lens, we would like to establish the limits of voltages that should be used in our analysis. It was already experimentally demonstrated that the optical performance (particularly lens aberrations) is compromised close to the reorientation threshold of the LC [30]. Our theoretical simulations confirm those experimental observations. Figure 1.4 demonstrates the deviation of the wavefront obtained by simulations (square dots) from the desired wavefront (solid line) for two values of driving voltages: one very close to the threshold (at 10 V_{rms}, Figure 1.4 (a)) and another well above it, at 30 V_{rms} (Figure 1.4 (b)).

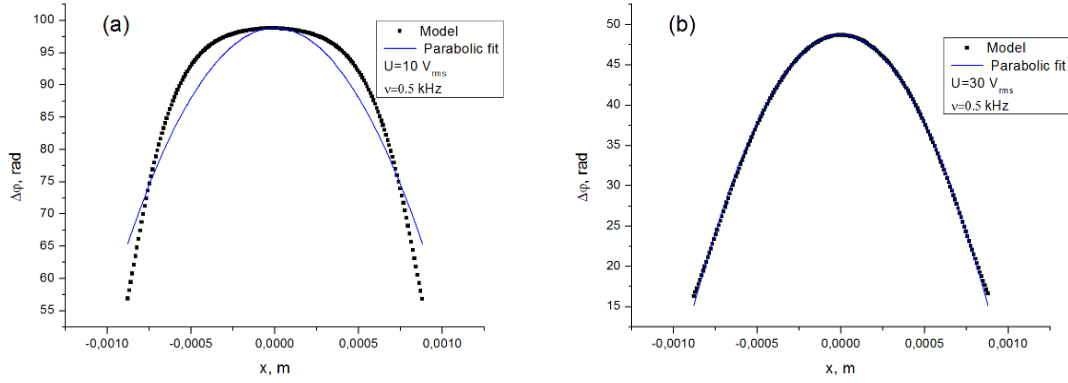


Figure 1.4. Parabolic approximation of optical phase retardation. Control voltage was (a) 10 V_{rms} and (b) 30 V_{rms}.

In addition, we have calculated the root mean square (RMS) deviation values between the simulated optical phase retardation and the desired parabolic form by using the following formula:

$$f_{rms} = \sqrt{\frac{\sum_{i=1}^N (\Delta\varphi_{\text{model}} - \Delta\varphi_{\text{fit}})_i^2}{N}} \quad (1.6)$$

We find that the RMS deviation is ≈ 3.35 rad for 10 V_{rms}, while it is lower by an order of magnitude (0.32 rad) for 30 V_{rms}. The above considerations and the experimental data, reported earlier in reference [30], help us establish the starting value of voltages (above 20 V_{rms}) that we shall consider in our further simulations.

Obviously, the final decision (choice) must be made after integrating the lens into a specific imaging system (camera, including base lens and image sensor) where we can measure the modulation transfer function (MTF). However, in the framework of this research we shall “focus” on the performance of the individual TLCL that can already provide good indications for the future camera integration.

1.4.1 Impact of the LC thickness

Another key parameter is the thickness L of the LC layer. We can establish the lower limit to satisfy the 10 cm minimal focal distance (or 10 diopters of OP) requirement often imposed on miniature cameras with $r \approx 1$ mm radius (2 mm clear aperture) [6]. Thus, by using Equation (1.2), we can estimate the corresponding thickness L of the LC layer (e.g., with optical birefringence of $\Delta n \approx 0.2$) as equal to $L \approx 30 \mu\text{m}$ (the experimental value of L was $40 \mu\text{m}$, given in Table 1.1).

With those two limits established (U_{min} and L_{min}), we can start the analysis of the possible lens performance optimization for different LC thicknesses and driving voltages (applied to the top and bottom electrodes).

The typical way to present the dynamic OP is to measure the value for a given voltage and then subtract the residual OP (0 V) from it [30]. This is how we define the clear optical power (COP). Figure 1.5 shows the dependency of the theoretically calculated COP on the LC thickness for various driving voltages U .

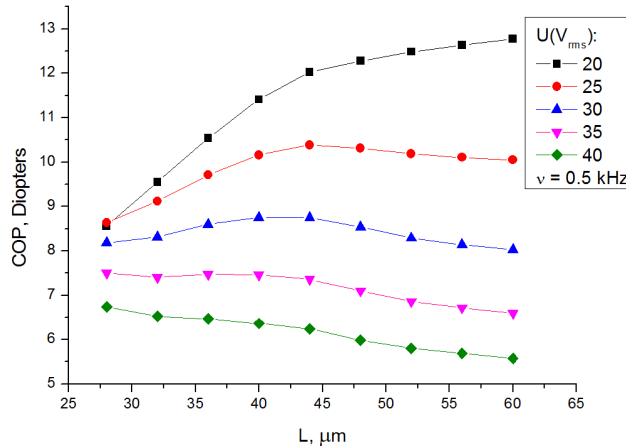


Figure 1.5. COP as a function of LC cell thickness and driving voltage.

The applied voltage range is maintained below $40 V_{rms}$ (for present theoretical considerations), as many mobile applications are very sensitive to the complexity and electric power consumption of the lens driver. As we have already mentioned, in those conditions, the dynamic range of OP (DROP) for a given value of L may be found by subtracting the OPs for minimal ($20 V_{rms}$) and maximal ($40 V_{rms}$) voltages. We could also consider higher voltages (Figure 1.3) to further reduce the OP and thus increase the DROP, but this would not change the tendencies that we try to identify here by just considering the range of voltages up to $40 V_{rms}$.

Thus, as can be seen from Figure 1.5, OP values are higher for relatively lower voltages (≥ 20 V_{rms} ; when mainly peripheral molecules are reoriented), and they decrease for higher voltages (40 V_{rms}) because then even central molecules are reoriented, reducing the phase contrast. For each LC thickness L , the operation of the lens may be represented by following the vertical line corresponding to that value L . For example, for $L \approx 32$ μm , the lens would provide $\text{OP} \approx 9.5$ D at 20 V_{rms} and $\text{OP} \approx 6.5$ D at 40 V_{rms} . Thus, the DROP of this lens would be about 3 D. It is clear (from Figure 1.5) that the DROP grows with increasing L (from ≈ 2 D at $L=28$ μm up to ≈ 7 D at $L=60$ μm). Those results may be understood by the fact that the LC reorientation mode in thicker cells requires less energy (the elastic energy being proportional to $\sim 1/L^2$) and also by using the same dielectric division principle (Equation (1.1)) showing that we obtain more relative drop of potential on the LC layer (U_{LC} is higher) with the increase of L .

However, this does not mean that the LC thickness L should be chosen to be as high as possible. In particular, it is well known [1] that the thermal fluctuation of the average molecular orientation in LCs may generate rather significant light scattering. This scattering increases exponentially ($\sim \exp(\alpha L)$) with the LC cell thickness L , where α is the scattering cross section of the LC material (mainly defined by birefringence Δn and elastic deformation constant K). As an example, the scattering may represent $\approx 5\%$ of transmitted light for values of $L \geq 50$ μm . In addition, there is the question of the speed. Thus, for the reference design (40 μm), the excitation and relaxation times are ≈ 100 and ≈ 500 ms, respectively. It is well known that the characteristic transition times (both relaxation $\sim \tau_r$ and excitation $\sim \tau_e$) will increase quadratically as the thickness increases ($\tau_r \sim L^2 \gamma / K$ and $\tau_e \sim \tau_r / (V^2 / V_{th}^2 - 1)$, where γ is the rotational viscosity of the LC) [52]. Therefore, the choice of L must be performed very carefully by taking into account the specific target application of the TLCL (the required OP, the acceptable voltage ranges, relaxation times, and scattering levels).

Finally, it is also worth mentioning that the thickness L of the LC layer is usually very well controlled during the manufacturing (less than ± 3 μm for $L \approx 40$ μm). In this case, using Figure 1.5, we can conclude that the manufacturing error of L is not a critical parameter because it would generate an approximate error of ± 0.5 D in the worst case scenario (at 20 V).

1.4.2 Hidden layer dimensions

In this section we analyze the impact of the dimensions of CL and IML, which together compose the DDOH layer. As we have already described, the DDOH layer is the “heart” of the lens, which is necessary to create spatial modulation of the electric field in the LC layer. We shall try among others to minimize the overall thickness of the DDOH layer by reducing the height of the core

lens (H_{CL}) starting with the experimental value (see Table 1.1). At the same time, we will recalculate the curvature R of the interface between the CL and IML to keep R_{CL} (CL base radius) unchanged so that the clear aperture diameter $d_a=1.75$ mm is fixed. The scheme of the DDOH layer and the corresponding variables are shown in Figure 1.6.

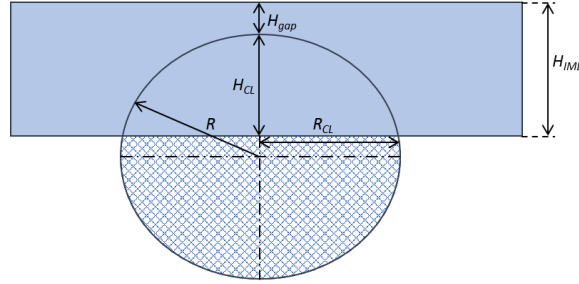


Figure 1.6. Schematics of the double dielectric hidden layer.

The following equations relate the radius of the sphere that forms the CL with the height and CL base radius:

$$R = \frac{H_{CL}^2 + R_{CL}^2}{2H_{CL}} \text{ and } H_{IML} = H_{CL} + H_{gap}, \quad (1.7)$$

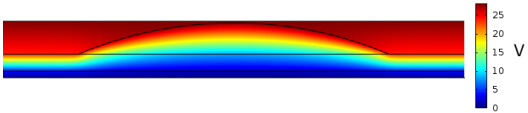
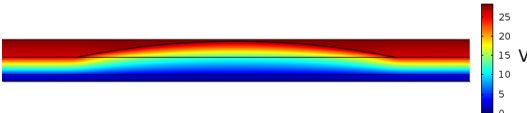
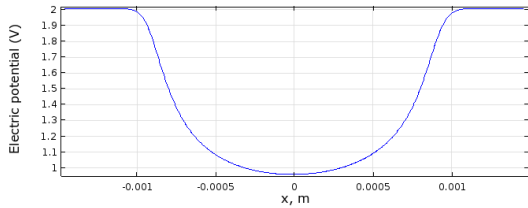
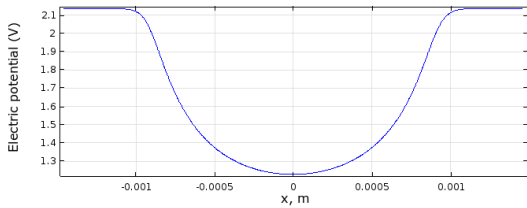
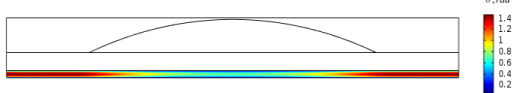

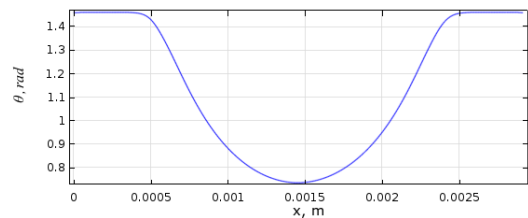
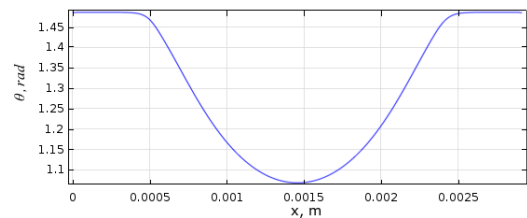
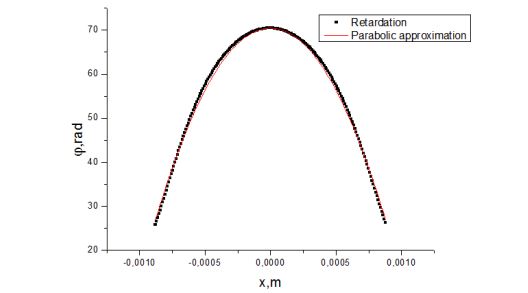
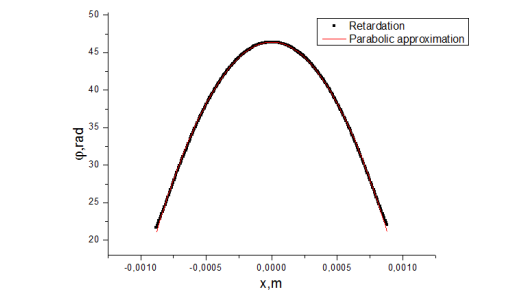
where H_{gap} is considered to be a constant (10 μm) height of the gap between IML and CL. Experimental values of CL and IML relative permittivities (Table 1.1) were used for our simulations in this section. The applied voltage considered for the simulation is 20 V_{rms} , at 1 kHz driving frequency.

Table 1.2 shows the comparison of simulations using experimental value of H_{CL} (185 μm) and H_{CL} reduced by 50%.

Deviation between simulated optical phase retardation and an ideal parabolic wavefront for the experimental value H_{CL} is 0.76 rad (and $\text{OP} \approx 11.4$ D), while it is 0.19 rad for 50% decreased H_{CL} ($\text{OP} \approx 6.6$ D). Thus, for higher values of H_{CL} we have higher OP, but worse wave front shape.

We may conclude that for the value of 92.5 μm , the electric potential inside the LC layer is higher, causing more LC director reorientation across the cell. The results for the calculated OP are presented in Figure 1.7.

Table 1.2. Comparison of simulations for $H_{CL}=185 \mu\text{m}$ and $H_{CL}=92.5 \mu\text{m}$.

$H_{CL}=185 \mu\text{m}$	$H_{CL}=92.5 \mu\text{m}$
1. Electric potential profile	
	
2. Electric potential at the middle of the LC cell	
	
3. Director reorientation	
	
4. Director reorientation in the middle of the LC cell	
	
5. Phase retardation	
	

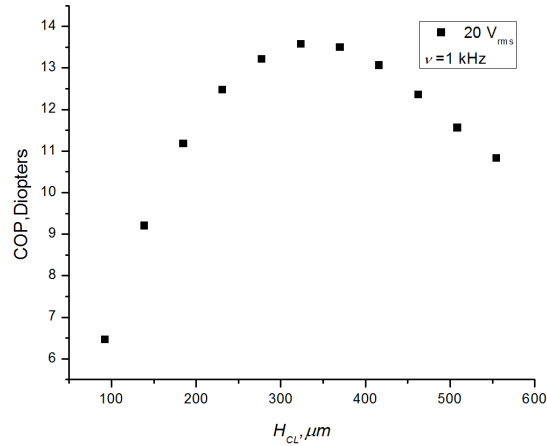


Figure 1.7. OP dependence on changes of the height H_{CL} of the CL (varied from 50% to 300% of the experimental value).

The OP increases with the H_{CL} since the spatial modulation depth of the field is increasing. However, this cannot be sustained further because this also increases the distance between the two electrodes and thus the driving voltages required. As a consequence, the OP starts dropping if we continue increasing the values of H_{CL} for a given driving voltage (Figure 1.7).

Our experience shows that, in contrast to the thickness of the LC layer, the height H_{CL} of the CL is more difficult to control. This requires more precautions, for example, for the values of H_{CL} around 185 μm , since a 10% variation of H_{CL} can bring up to ± 1 D of OP variation, which is already noticeable.

Now let us consider different radii of the CL. Here we increase the experimental value ($R_{CL}=925 \mu\text{m}$) by 15% and 30% for these simulations. The aperture of the lens remains fixed at 1.75 mm. The CL height is considered to be 185 μm . Schematic representation of this situation is shown in Figure 1.8.

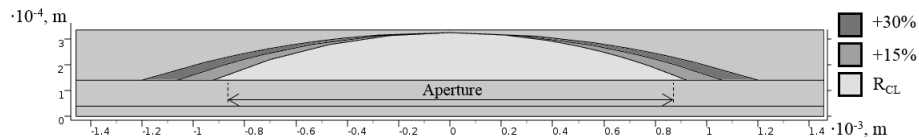


Figure 1.8. Variation of the base radius of the CL.

The obtained results are shown in Figure 1.9.

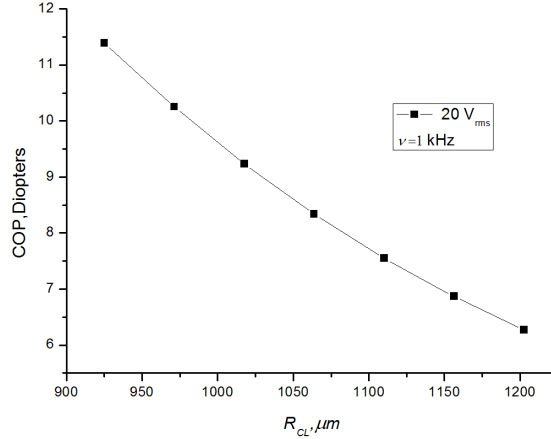


Figure 1.9. OP versus base radius of the CL.

As we can see, the COP of the lens decreases with the increase of the diameter of CL. This might be expected because (as can be seen from the Equation (1.1)) the relative contrast of the electric field (measured at the periphery and at the center of the lens) is reduced when the base radius of the CL is increased.

As we have already mentioned, the developed tool may be used to quickly estimate the performance of TLCL for various applications. One of them, the adaptive endoscopy, is attracting more and more attention (see [47] and references therein). Thus, a quick estimation shows that, by using an optimized DDOH, we can obtain huge OPs (on the order of 300 D) for clear apertures of the endoscope of 0.5 mm. This may be further increased by increasing the LC thickness since, very often, the changes of the scene here are slow (e.g., migration of stem cells [47]) and we can use digital software to reduce the impact of additional scattering.

We would like to address a very interesting question (we are thankful to the referee for raising this question) about the possibility of strong reduction of the lateral size of the CL, for example, to fabricate micro lens or micro prism arrays. A quick analysis shows that the depth of modulation of the electrical field (inside the LC layer) decreases significantly (depending upon the lateral size of the CL) when the R_{CL} becomes the same order of magnitude as the thickness L of the LC layer. This phenomenon (we might probably call this also an “MTF”) will prohibit the fabrication of fine modulation structures of the electric field using the DDOH approach, and we shall analyze it in a forthcoming article.

1.5 Variations of material parameters of the lens

1.5.1 Increase of the relative permittivity of IML

The ratio of dielectric constants of CL and IML defines the spatial gradient of the electric field inside the LC layer for the given profile of the CL. In this section, we explore the impact on the lens performance by increasing the relative permittivity of the IML (with respect to the permittivity of the CL, $\epsilon_2 \equiv \epsilon_{CL} = 3.9$). As we can see from Figure 1.10, the OP of the lens increases and saturates with the increase of the dielectric constant of IML $\epsilon_I \equiv \epsilon_{IML}$ (fixed conductivities of CL and IML materials are $\delta_{IML} = 3 \cdot 10^{-7}$ S/m and $\delta_{CL} = 1 \cdot 10^{-13}$ S/m).

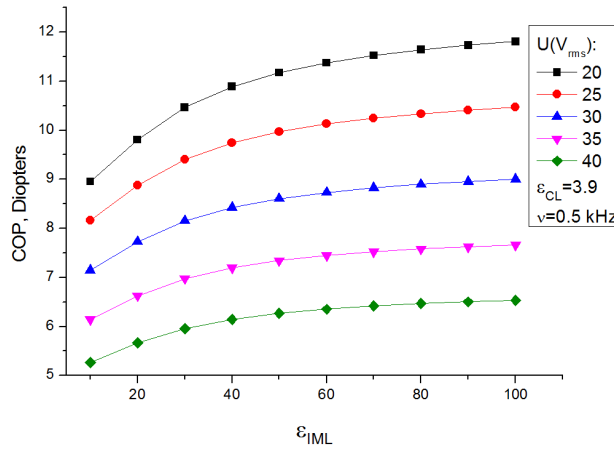


Figure 1.10. OP dependence on the relative permittivity of index matching layer. The relative permittivity of the CL was fixed to 3.9.

The corresponding DROP grows from ≈ 3.75 D at $\epsilon_{IML} = 10$ to ≈ 5.75 D at $\epsilon_{IML} = 100$. The mechanism of the saturation trend (at high ϵ_{IML} values) can be understood here by considering the ultimate situation when ϵ_{IML} is infinitely high. In this case, the IML no longer represents a noticeable drop of potential (with the further increase of its permittivity); therefore, the contrast cannot be increased further.

1.5.2 Increase of the conductivity of IML

Another mechanism of optimizing the OP of the lens may be the use of materials for IML and CL that have the same permittivity but considerably different conductivities σ at the driving frequency (1 kHz). For example, we can use a fluorinated polymer for the CL and we can fill the space around it with ion-doped liquid that has the same permittivity as the polymer (IML) at kHz

frequencies. Another approach could be the use of the same polymer material for both CL and IML parts but dope them differently: one to increase the conductivity and the second to only adjust the refractive index. Table 1.3 shows two examples of “similar” materials with quite different conductivities.

Table 1.3. Examples of conductivity values for two different materials.

Material	σ (S/m) at 20 °C
Sea water	4.80 [53]
Deionized water	$5.50 \cdot 10^{-6}$ [54]

In this way, we can achieve the same lensing effect as presented before for the case of the difference in dielectric constants. The obtained results are shown in Figure 1.11.

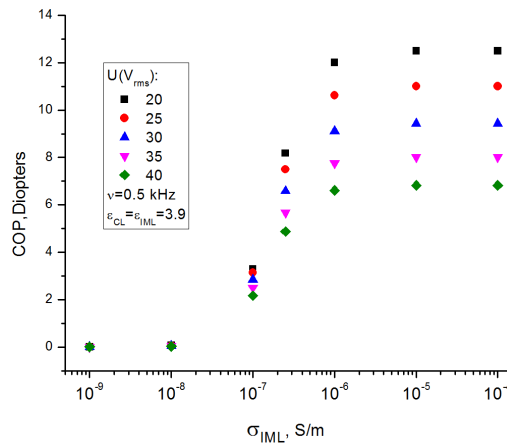


Figure 1.11. OP dependence on the conductivity of index matching layer. Relative permittivity is the same for CL and IML. Conductivity of CL was constant: $\sigma_{CL}=1 \cdot 10^{-13}$ S/m.

Here also we can see a tendency of OP increase and saturation. The mechanism of the saturation (at high σ_{IML} values) can be understood here by considering the extreme situation when the σ_{IML} is very high. In this case, the effective form of the top electrode would be transformed from uniform into a curved one that “embraces” the CL and middle glass substrate. It will then represent no further increase of OP, even for higher conductivities of the IML.

1.6 Environmental (temperature) dependence

Finally, we can also analyze the influence of the main environmental factor (the temperature) on the performance of the lens. To converge to the desired focal plane fast enough, TLCLs must

operate at relatively high temperatures from the beginning (many flat panel displays operate at $\approx 45^\circ\text{C}$). For such temperature ranges (from 20°C to 45°C), the relative dielectric properties of polymers used for the construction of the DDOH may be considered almost unchanged. In this case, the main contribution to the change of OP would be related to the optical birefringence $\Delta n \equiv n_{\parallel} - n_{\perp}$, the dielectric anisotropy $\Delta \varepsilon \equiv \varepsilon_{\parallel} - \varepsilon_{\perp}$, and the elastic constants K_{11} and K_{33} of the LC used. For this simulation, we used the well-known LC materials 5CB [55,56] and LC E49 [57], since the temperature dependencies of their physical parameters are available in the scientific literature (see Table 1.4).

Table 1.4. Simulation parameters.

	E49	5CB
ν	5 kHz	3.03 kHz
λ	632.8 nm	650 nm
T	25-95 $^\circ\text{C}$	25.1-33.8 $^\circ\text{C}$

Obviously, the lens operation will be lost above the nematic-isotropic phase transition temperature T_{N-I} ($T_{N-I} \approx 97^\circ\text{C}$ for E49 and $T_{N-I} \approx 35.1^\circ\text{C}$ for 5CB). Please note that the measurements of parameters (in references [55–57]) were made for slightly different wavelengths and electric field frequencies (those are data we could find in the scientific literature).

The corresponding results are shown in Figure 1.12.

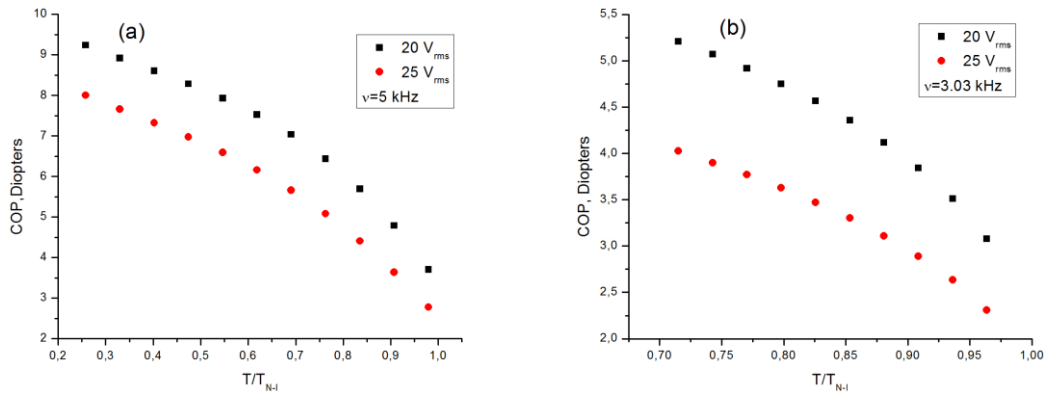


Figure 1.12. Temperature dependence of OP for (a) E49 and (b) 5CB LCs. Nematic-isotropic transition temperatures (T_{N-I}) for E49 and 5CB were about 97°C and 35.1°C , respectively.

As we can see, the increase of operation temperature reduces the lens OP significantly.

Obviously, the OP at high voltages will also decrease with the increase of the temperature, and the same will happen with the dynamic range. Thus, one could imagine that lower temperatures would be favored. However, the transition times [52] will then also increase almost exponentially, $\tau_r \sim \gamma/K \sim \exp(-T)$, and this must be a trade-off between the maximal dynamic range and focusing speed.

1.7 Summary and conclusions

We demonstrated that the OP of the LC lens using a DDOH layer may be increased by increasing the LC thickness and that a trade-off must be made between this increase and the transition speed and scattering. We also showed that the OP of the lens increased and then saturated when we tried to optimize performance with the contrast of dielectric and conductive parameters of the DDOH layer. Finally, we also demonstrated that the OP of the lens may be increased for larger DDOH layer thicknesses, which in turns raised the question of acceptable voltages to drive such a lens. Indeed, we think that the DDOH layer concept is very interesting overall and useful, since it allows us to obtain arbitrary (predetermined) electrically variable wave fronts without compromising the default mode of the device (the optical neutrality). However, the main drawback of this approach is the voltage increase due to the thickness of the DDOH layer.

1.8 Acknowledgment

We thank the Canada Research Chair in LCs and Behavioral Biophotonics, held by T. G., who received the Manning Innovation Award 2014. We are grateful to the R&D teams of LensVector Inc. and TLCL Optical Research Inc. and particularly to Dr. K. Asatryan for his valuable advice.

Chapter 2 Modulation transfer function of liquid crystal microlenses and microprisms using double dielectric layer

Oleksandr Sova¹, Victor Reshetnyak² and Tigran Galstian^{1,3}

¹Université Laval, Département de physique, de génie physique et d'optique, Centre d'optique, photonique et laser, Pav. d'Optique-Photonique, 2375 Rue de la Terrasse, Québec G1V0A6, Canada

²Physics Faculty, Taras Shevchenko National University of Kyiv, Volodymyrska Street 64, Kyiv 01601, Ukraine

³Lensvector Inc., 6203 San Ignacio Ave. Suite 110, San Jose, California 95119, USA

*Corresponding author: galstian@phy.ulaval.ca

Applied Optics, Vol. 57: pp. 18-24, 2018

Continuing the exploration of hidden double dielectric divisor principle, this chapter presents our theoretical study of microlens and microprism structures. The chapter is based on a manuscript published in Applied Optics.

In our simulations we varied the spatial frequency of sine and sawtooth structures forming the dielectric layer. Corresponding optical phase modulation contrasts have been evaluated. Root mean square deviations from desired wavefront shapes were calculated. For the case of microlenses we have identified an optimal spatial frequency (clear aperture size), providing maximal optical power. Degradation of wavefront modulation was observed as the result of fringing electric fields. A comparison with a standard interdigital electrode approach has been made.

This design demonstrates that a tunable wavefront of potentially arbitrary predefined shape could be obtained. The advantages of discussed technology are in simplicity of experimental assembly, molding of the hidden layer being the most complex part, and zero optical power ground state.

2.1 Résumé

Fonction de transfert de modulation des microlentilles et des microprismes à cristaux liquides utilisant une double couche diélectrique

Nous examinons des microlentilles et des microprismes à cristaux liquides à réglage électrique qui sont basés sur des doubles couches diélectriques optiquement cachées. Une étude théorique comparative des limites de résolution spatiale de la création d'un champ électrique spatialement modulé par la double couche diélectrique est réalisée. La profondeur de la modulation de phase optique et son écart par rapport au front d'onde désiré sont obtenus pour les géométries sinus et en dents de scie de la structure diélectrique cachée. Une comparaison avec l'approche de réorientation moléculaire standard en utilisant des électrodes à motifs est fournie.

2.2 Abstract

We investigate electrically tunable liquid crystal (LC) microlenses and microprisms based on double dielectric optically hidden (DDOH) layers. Comparative theoretical study of the spatial resolution limits in the creation of spatially modulated electric field by the DDOH layer is conducted. Both the depth of the resulting optical phase modulation and its deviation from the desired wavefront are obtained for sine and sawtooth geometries of the DDOH layer's structure. A comparison is provided with the standard LC reorientation approach using patterned electrodes.

2.3 Introduction

There are many electrically variable or tunable liquid crystal lens (TLCL) approaches [6,15,22,32,36,58]. We have recently reported the theoretical analyses [28,44] of one specific approach [30] that uses a double dielectric optically hidden (DDOH) layer to modulate the electric field in the layer of the liquid crystal (LC). While the main tendencies and tradeoffs have been analyzed, one question (raised by the referee) remained unanswered: how small features may be used in the DDOH structure to create corresponding electric field distribution and LC reorientation patterns.

The present work describes our additional analyses dedicated to this question. We have considered both sine and sawtooth structures to simulate microlens and microprism cases. As a key parameter, we have used the optical phase modulation contrast (or depth) for optical rays passing through the extremes of the DDOH layer (see hereafter). However, in many applications, the wavefront modulation profile is also important. Thus, we have also used the root mean square deviation (RMSD) from the desired forms in parallel with the modulation depth analyses.

In the case of a single lens implementation [30] (see also Figure 2.1), the DDOH layer is composed of a lens-like material that we call a core lens (CL) and of a surrounding material that is an optically index matched layer (IML). Indeed, those materials have the same dielectric constants $\epsilon_{CL} = \epsilon_{IML}$ at optical frequencies (10^{14} Hz). Thus the doublet structure is optically hidden (since they have the same refractive indexes $n_{CL} = n_{IML}$, in contrast with [29]) making the device optically passive in the default mode (no voltage applied). However, those materials are chosen to possess different dielectric constants $\epsilon_{CL} \neq \epsilon_{IML}$ at low frequencies (10^3 Hz) that are typically used to dynamically reorient LC molecules [1,9]. This property (along with the principle of voltage division [29,30]) is used to build the laterally non-uniform electric field inside the LC layer.

2.4 Simulation details

Three different electro-optical systems have been simulated and analyzed. The methods implemented here have been discussed in details in our previous works [28,44]. Equations for electric potential distribution (see Eq. (10) in [28]) and director's (a unit vector representing the local average orientation of long molecular axes of the nematic LC [1]) reorientation (see Eq. (5) in [28]) are coupled by dielectric tensor and solved simultaneously using Comsol Multiphysics. Table 2.1 contains some parameters used for simulations:

Table 2.1. Simulation parameters.

Parameter	Value	Description
ϵ_{glass}	6.9	Relative permittivity of glass
ϵ_{CL}	3.9	Relative permittivity of CL material
ϵ_{IML}	62	Relative permittivity of IML material
σ_{glass}	$1 \cdot 10^{-13}$ S/m	Conductivity of glass
σ_{IML}	$3 \cdot 10^{-7}$ S/m	Conductivity of IML material
σ_{CL}	$1 \cdot 10^{-13}$ S/m	Conductivity of CL material
ϵ_l	17	Relative permittivity of LC (parallel component)
ϵ_a	10.4	Dielectric anisotropy of LC
n_o	1.52	Ordinary refractive index
n_e	1.77	Extraordinary refractive index
K_{11}	21.5 pN	Splay elastic constant
K_{33}	23.9 pN	Bend elastic constant
$\theta_1=\theta_2$	2.5°	Pretilt angle (planar orientation)
λ	632.8 nm	Wavelength of the probe beam

In this section, we introduce the definitions of calculated values and specifics of each simulation considered.

The modulation transfer function (MTF) usually characterizes optical system's response to the spatial frequency of an input signal. The limited spatial resolution of an optical system leads to modulation depth's degradation of the output signal (image). In the context of our work, it is well known that LC based microlens and microprism arrays may dynamically shape the phase of incident light with the help of a spatially non-uniform electric field. However, the electric field usually extends well beyond the electrodes (used to create this field), its shape in space may depend upon the

environmental and geometrical parameters with respect to those electrodes. In addition, the response of LC materials to external field (including electric one) is non-linear and spatially non-local. Thus, to quantify the final optical modulation efficiency (e.g., versus the spatial frequency of the DDOH layer), we would like to define the functions:

$$\text{MTF}_\theta = \frac{\theta_{\max} - \theta_{\min}}{\theta_{\max} + \theta_{\min}}, \quad \text{MTF}_\varphi = \frac{\varphi_{\max} - \varphi_{\min}}{\varphi_{\max} + \varphi_{\min}}, \quad (2.1)$$

where θ is the LC director's tilt angle and φ is the optical phase retardation of a beam exiting from the LC cell.

In addition, to analyze the wavefront's phase deviation from the parabolic (in the case of microlenses) or linear shapes (in the case of microprisms) we use the following RMS deviation:

$$\text{RMSD}(\varphi) = \sqrt{\frac{\sum_{i=1}^N (\varphi^i_{\text{simulated}} - \varphi^i_{\text{ideal}})^2}{N}} \quad (2.2)$$

To compare the RMSDs for different spatial frequencies and get rid of the influence of absolute values of phase retardations we have normalized them by the maximal phase retardation (y axis) for each clear aperture considered (please note that the aperture size is not the same for RMSDs shown in Figure 2.12 (a) and (b), the case of microprisms).

Obviously, one can expect that the spatial frequency increase (in the CL/IML structure of the DDOH layer) will lead to some changes of RMSD and to the decrease of the electric field modulation depth (in the LC layer), due to the effect of fringing fields. However, it is useful to clarify the corresponding dependences and tendencies.

2.5 Results

2.5.1 Hidden microlens array

We start by considering a system that has a DDOH layer made of sinusoidally distributed (or sine shaped) CL material and IML. We have simulated periodic structures infinite in O_x direction (see Figure 2.1) in order to avoid the influence of vertical edges. The spatial frequency of this sine shape is gradually increased from 1 period per 2000 μm (with the max CL height in the center) up to 10 periods per 2000 μm .

In Figure 2.1 the schematic representation of such a structure is shown for the case of 5 sine CL material periods per 2000 μm . As the relative permittivity of the IML material is much higher

than CL's permittivity, we expect higher voltage value under hidden layer's areas filled mostly with IML material. Thus, higher values of director tilt angle θ are also expected in these regions.

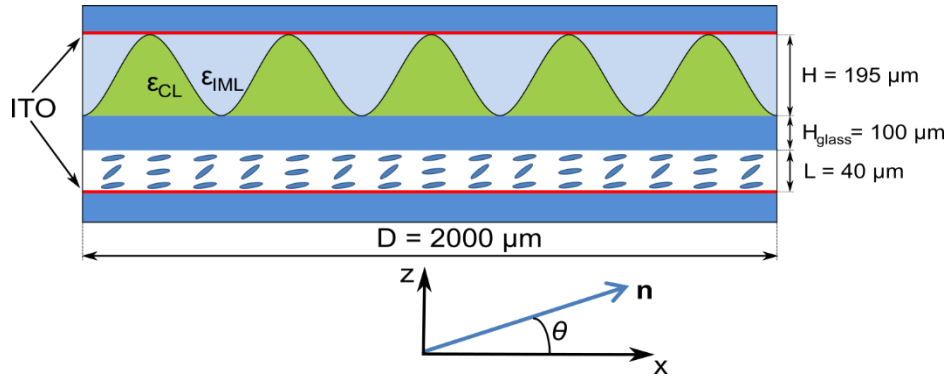


Figure 2.1. Schematics of the simulated microlens array with sinusoidal distribution of the CL material.

We have made simulations, the results of which identify the value of voltage V_{max} , needed to obtain maximal optical power (OP), as being 11 V for $H_{glass}=30 \mu\text{m}$, 14 V for $H_{glass}=100 \mu\text{m}$ and 30 V for $H_{glass}=300 \mu\text{m}$ (see Fig. 2.2).

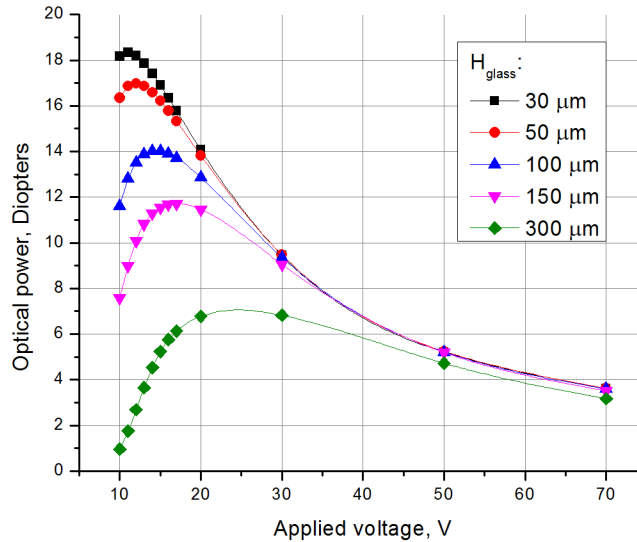


Figure 2.2. Optical power dependence on control voltage (single LC lens), for different thicknesses of middle glass substrate (aperture diameter = 1.75 mm).

Using the 30 μm thick glass is extremely challenging from manufacturing point of view. The 300 μm is much easier, but it requires driving voltages that are too high for mobile imaging applications. That is why the 100 μm thick middle substrate (more reasonable from manufacturing point of view) was chosen for our simulations. We also know from our previous studies [28,30,44]

that the lens performance (aberrations and scattering) is better for voltages that are slightly higher than the V_{\max} . This is the reason why we have chosen $20 V_{\text{rms}}$ (1 kHz) for $100 \mu\text{m}$ thick middle substrate for our simulations. Also, while in principle it might be possible to find a middle glass made from a material that may have different dielectric constants ϵ_{glass} , in general, the increase of the ϵ_{glass} is the equivalent of increasing the applied voltage on the LC layer (since the drop of potential on the middle substrate will then be reduced). Thus, for example, in the case of 10 microlenses per $2000 \mu\text{m}$, if we keep the voltage value the same (e.g., at the decreasing segment of the transfer function, at the right of Fig. 2.2) and increase the value of ϵ_{glass} , then the obtained OPs are 59.87 D; 54.55 D and 44.36 D for $\epsilon_{\text{glass}} = 3.45$; $\epsilon_{\text{glass}} = 6.9$ and $\epsilon_{\text{glass}} = 10.35$, respectively. Obviously, this means that lower voltages would be required to obtain the same OP values if we use higher ϵ_{glass} , which is very desired. However, here also, given that the standard glass (widely used in manufacturing) has the value $\epsilon_{\text{glass}} = 6.9$, we have decided to use this value in our further simulations.

An example of electric potential modulation in the LC cell is demonstrated in Fig. 2.3. The highest value of modulation depth is obtained for one microlens over $2000 \mu\text{m}$ (blue solid line) and it declines rapidly as more periods of CL material are introduced (see green dotted and red dashed lines for 3 and 5 microlenses per $2000 \mu\text{m}$, respectively).

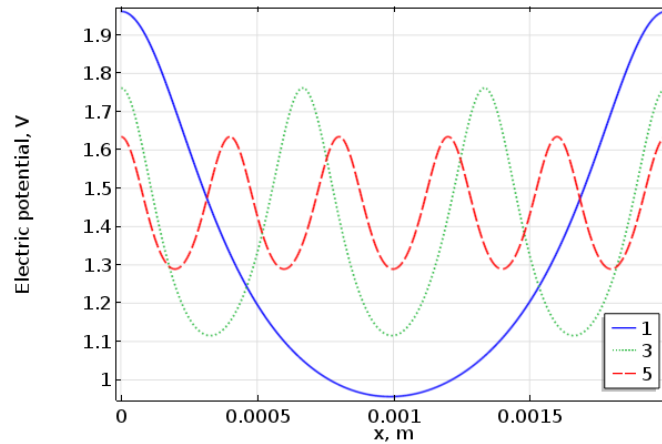


Figure 2.3. Electric potential distribution in the middle of the LC cell for different numbers of microlenses within $2000 \mu\text{m}$ wide simulated system (different spatial frequencies).

Calculated MTFs for both θ and φ rapidly decrease with the spatial frequency's increase (Fig. 2.4). The origin of such degradation may be related to the fringing fields of neighboring zones that reduces the modulation depth of the electric field in the layer of LC.

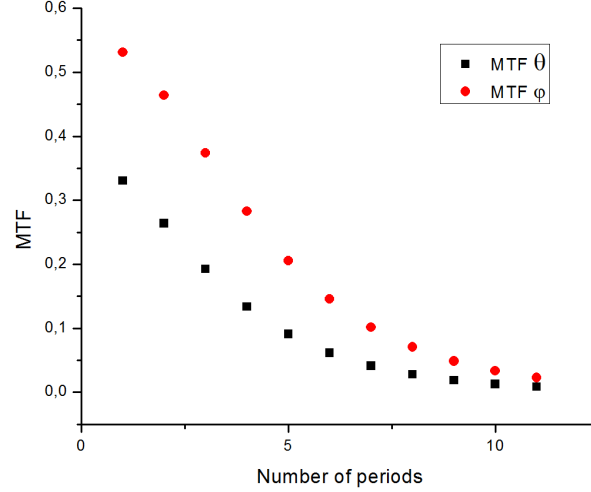


Figure 2.4. Modulation transfer function (the case of sinusoidal CL material).

The OP of an individual microlens is shown in Fig. 2.5. We can see that a maximum of OP ($OP_{max} \approx 97$ D) is reached for 5 periods of the sine shaped CL material, making it an optimal choice of spatial frequency in terms of OP. In our previous work [44] we described a lens which had the $OP_{max} \approx 15$ D, with the clear aperture of 1.75 mm. We would like to stress that OP_{max} is found for a certain set of parameters, but it can be even higher under some circumstances, for example: in the case of higher contrast between CL and IML relative permittivities, optimized structure of hidden layer, smart choice of control voltage or when thinner glass substrates are used. Aperture diameter of a single microlens is presented on this plot as well (the OP_{max} corresponds to the 400 μm aperture diameter). It is worth mentioning that we observe here two counter acting mechanisms. First, the increase of the spatial frequency reduces the value of $\Delta\varphi \equiv \varphi_{max} - \varphi_{min}$. Second, obviously, the radius r of each microlens is reduced at the same time. The non-monotonic behavior of the OP can then be understood if we remember that the reorientation of LC molecules creates a gradient index lens, the OP of which may be described as [6,15]

$$OP \approx \left(\frac{\lambda}{\pi} \right) \frac{\Delta\varphi}{r^2}, \quad (2.3)$$

where λ is the light wavelength in vacuum.

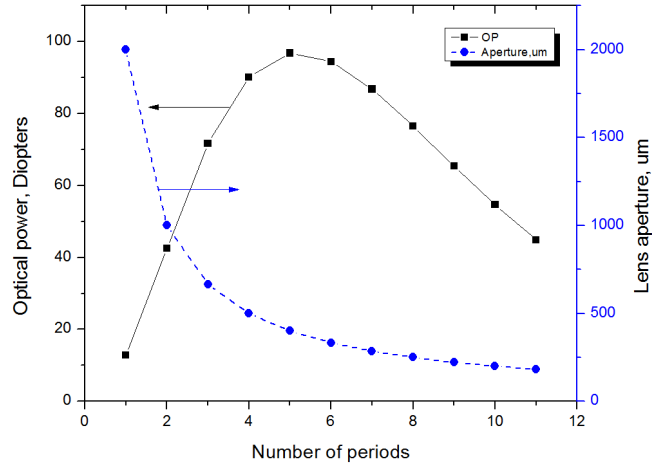


Figure 2.5. Dependence of the optical power and lens aperture diameter of each microlens versus the number of CL units (the case of sinusoidal CL material).

The most important aspect of the lens performance is the image quality that it can provide in a camera. To qualify the wavefront's shape, created by a single microlens in the array, we have calculated the corresponding normalized RMS deviation from parabolic fit (Fig. 2.6). Here we observe a gradual decrease of $\Delta\varphi$ for higher spatial frequencies, when RMSD increases and saturates. Thus, the final choice of the DDOH layer's spatial frequency must be made by taking into account the desired OP (Fig. 2.5) and RMSD (Fig. 2.6) values. For example, the OP_{max} would correspond to 5 units of CL and the RMSD would then be ≈ 0.197 .

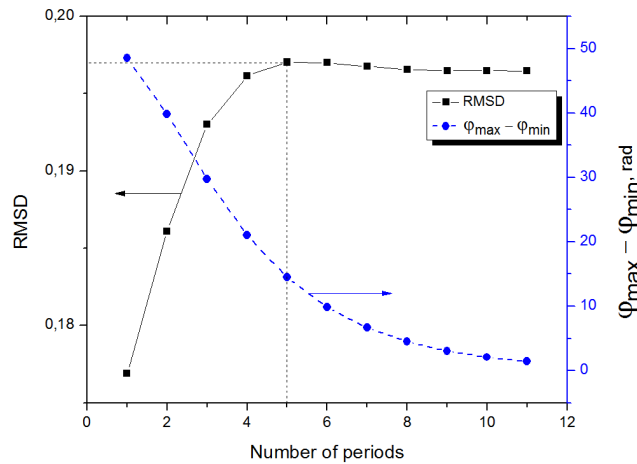


Figure 2.6. Normalized RMS phase retardation deviation from ideal parabolic shape and difference between max and min phase retardation (the case of sinusoidal CL material) versus the number of CL units.

2.5.2 Hidden microprism array

Another interesting geometry of DDOH structure corresponds to microprisms. Tunable microprism arrays can be used as laser beam steering devices [50]. Simulations for this case were done under the same conditions as for microlens arrays. An example of a simulated system with 5 microprisms per 2000 μm is shown below (Fig. 2.7)

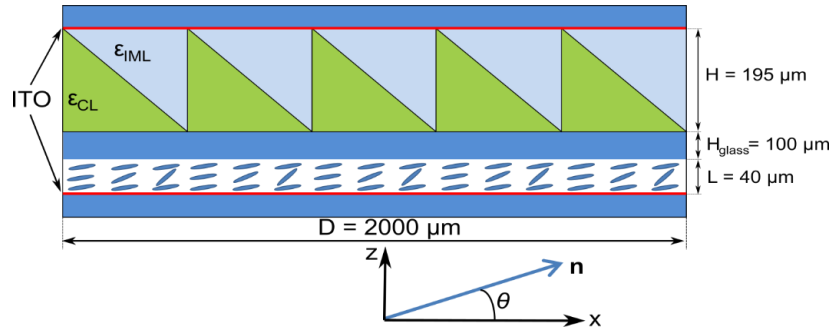


Figure 2.7. Schematics of the simulated microprism array.

Here also the electric field modulation depth decreases with the increase of the prism-shaped CL material's spatial frequency (Fig. 2.8). It can be noticed that at $x=2000 \mu\text{m}$ (extreme right corner of Fig. 2.8) there is a decrease of the electric potential (beyond C), even in the case of one prism. As was mentioned above, we maintain periodic boundary conditions at vertical boundaries, so the decrease of electric potential can be explained by the influence of the next (neighboring) prism. We can also see that the desired “asymmetric” shape of phase modulation has significant undesired non-monotonic zones (between A and C) at the extremums of the prism structure (it is not linear as desired).

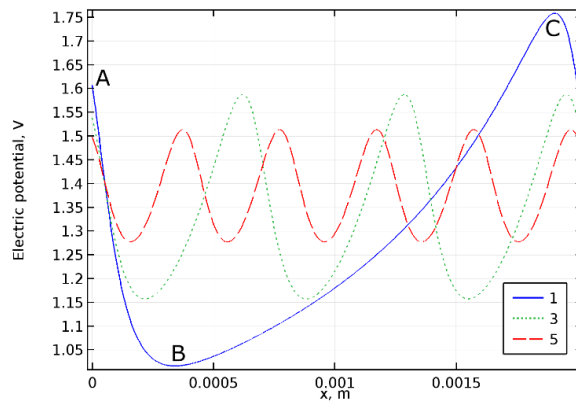


Figure 2.8. Electric potential distribution in the middle of the LC cell for different numbers of microprisms within 2000 μm wide simulated system (different spatial frequencies).

Finally, it is clear that this asymmetry is almost lost already for 5 microprisms and the array operates rather like a microlens array instead of a microprism array.

Here the maximal calculated MTF values are smaller (for both MTF θ and MTF φ) than in the previous case, but the rate of decrease is slightly smaller as well (Fig. 2.9).

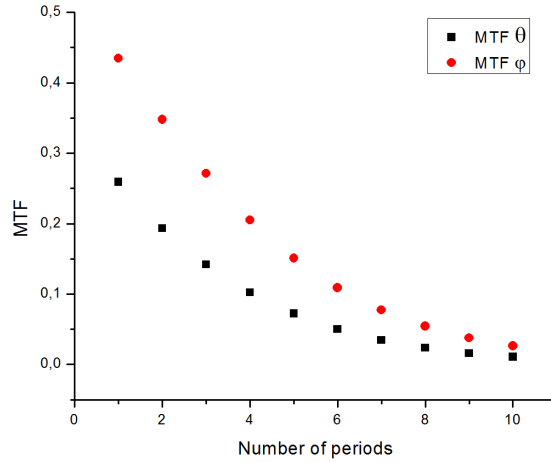


Figure 2.9. Modulation transfer function (the case of microprism array).

The corresponding nonlinear response of the LC director's tilt angle and of the output phase shift are depicted, respectively, in Figs. 2.10 (a) and 2.10 (b).

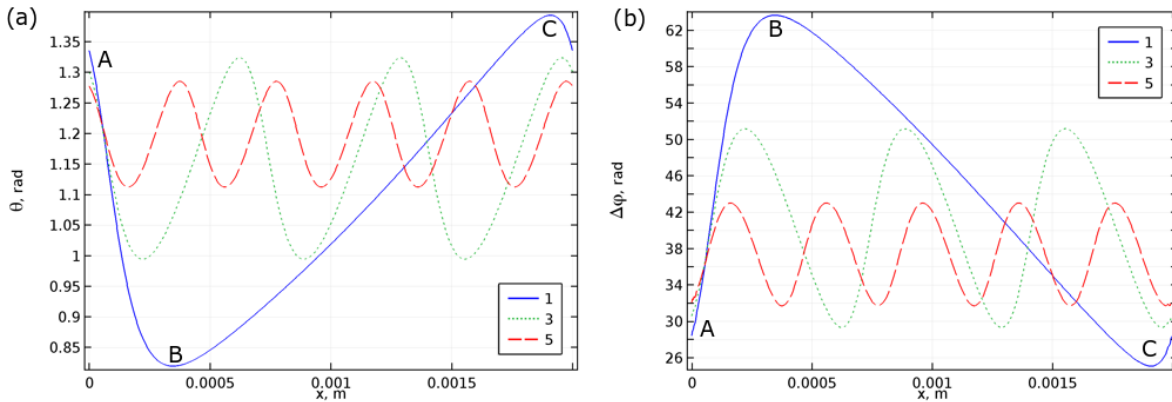


Figure 2.10. (a) Director tilt angle in the middle of the LC cell for 1, 3 and 5 microprisms over $2000 \mu\text{m}$ and (b) the corresponding phase shifts.

As it is well known, in the case of a plane wave passing through a set of regular glass microprisms, the phase retardation gradually decreases along the base of each prism until it reaches a minimal value and then increases abruptly at the beginning of the next microprism. Thus, the

function of phase retardation has sharp transitions. In contrast, for our system, these transitions are “blurred” by the effect of fringing fields (see Fig. 2.10 (b), the red (dashed) line for 5 microprisms per 2000 μm , for example). Therefore, we have “dead zones” (between A and B), the areas that would tilt a part of light in the opposite (to the desired) direction. The percentage of the structure’s length that contributes to the “dead zone”, depending upon the spatial frequency of the prism shaped CL material, is shown in Fig. 2.11:

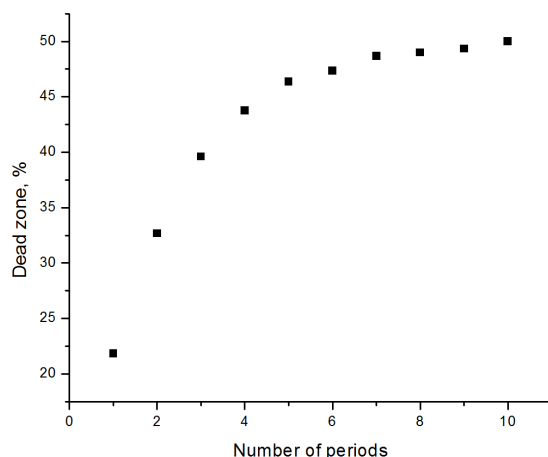


Figure 2.11. Percentage of the prism width in the “dead zone” due to fringing fields versus the number of microprisms per 2000 μm .

It increases and saturates at approximately 50% for 10 prisms per 2000 μm , so at this point it becomes impossible to distinguish the “dead zone” from the “active zone”. The device here acts like a microlens array (focusing light) instead of a microprism array (tilting light).

We have performed linear fit (in the least-squares sense) within the “active zone” (between B and C, Fig. 2.10 (b)) as well as within the entire aperture of the microprism (between A and C, Fig. 2.10 (b)) and calculated normalized RMS deviation of phase retardation from linear approximations. The corresponding results are shown in the Figs. 2.12 (a) and (b). Obviously, from the practical point of view, the most important is the second case (the entire aperture, Fig. 2.12 (b)).

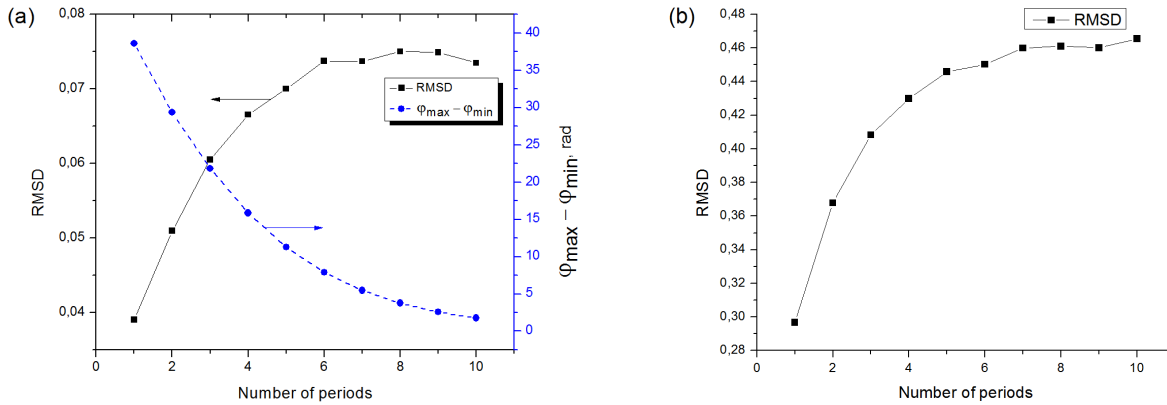


Figure 2.12. Normalized RMS phase retardation deviation from the (desired) linear form and the difference between max and min phase retardation values versus the number of microprisms over 2000 μm within the (a) “active zone” of single microprism and (b) in the entire clear aperture of the microprism (covering both active and passive zones).

However, in some cases, the blocking of the “passive zone” may be acceptable. Then the “active zone” can perform rather well (see low normalized RMS aberrations in Fig. 2.12 (a)). But we have to be careful with this comparison since only the “active zone” is considered here.

We can see here that the RMSD also increases as we increase the number of periods per 2000 μm and reaches saturation (while $\Delta\varphi$ decreases).

2.5.3 Out of plane switching

Only for comparison purposes, we have also simulated (using the same approach) a simple planar oriented LC in between uniform (grounded) bottom and periodic top electrodes (parallel “interdigital” electrodes with the same electric potential of 2 V_{rms} at 1 kHz frequency on each of the top electrodes), traditionally used for an “out of plane” modulation scheme (Fig. 2.13). This type of microlens arrays have several advantages, for instance, low operating voltage and simple manufacturing (etching of ITO versus molding of the DDOH layer). This electrode configuration provides electric field that is strong directly under top electrodes and gradually decreases towards the gaps in between any two neighboring electrodes. Therefore, the director’s tilt angle approaches its maximum (for a certain control voltage) near the centers of top electrodes and is smaller in the areas of the gaps. Each of top electrodes has a fixed width of 10 μm , the gaps among electrodes are varied from 100 μm up to 500 μm . The system is considered infinite in O_x direction, like in both previous cases.

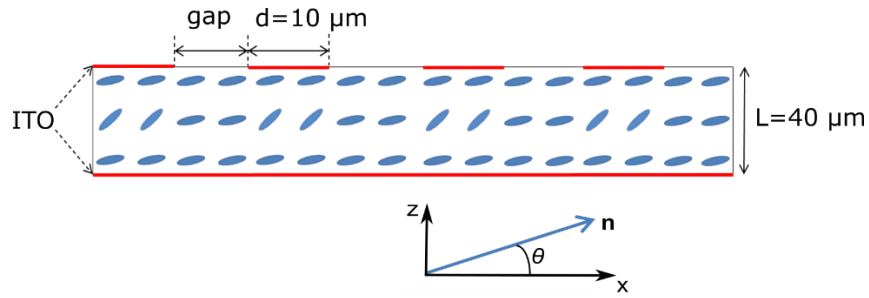


Figure 2.13. Schematics of the “out of plane” switching.

MTF θ reaches up to 0.9 for relatively wide gaps and saturates (Fig. 2.14). This can be easily explained. The LC is reoriented in the regions under interdigital electrodes and the electric field in the intermediate gap regions decreases gradually with their increase. At some point the critical distance (about 300 μm in our case) among electrodes is reached and the electric field becomes not strong enough to orient LC molecules. No further gap increase makes any difference and so the MTF saturation takes place.

Phase retardation φ has higher values in gap regions and decreases when areas under top electrodes are approached. MTF φ saturates much faster, starting from the gap width of 150 μm .

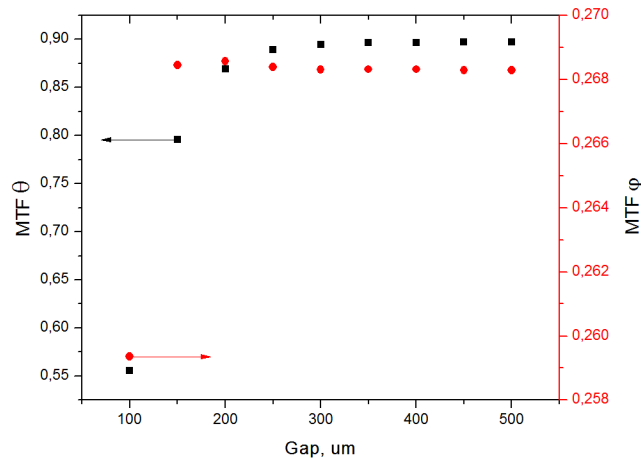


Figure 2.14. Modulation transfer function (the case of “out of plane” switching using patterned electrodes).

The OP’s dependence of a single microlens on gap’s width is depicted below (Fig. 2.15). In this case also, as the aperture is expanded we observe a drop of OP ($\sim 1/r^2$). However, the choice of geometrical parameters here is such that the 100 μm gap would correspond to the optimal ratio of gap versus the top and bottom electrodes separation (≈ 2.5 , [59]) for which the modulation depth and the wavefront are already optimal for the microlens. Further increase of the gap results in the gradual

increase of wavefront’s normalized RMS deviation from the parabolic shape (Fig. 2.16). The value of $\Delta\varphi$ is also increasing (with the increase of the gap), but it is faster, followed by saturation. Obviously, in the case of wide gaps between neighboring electrodes, most part of the LC remains unused and the reorientation profile becomes step-wise. Thus, here also, the final choice of the geometry must take into account the desired OP (Fig. 2.15) and RMSD (Fig. 2.16) values.

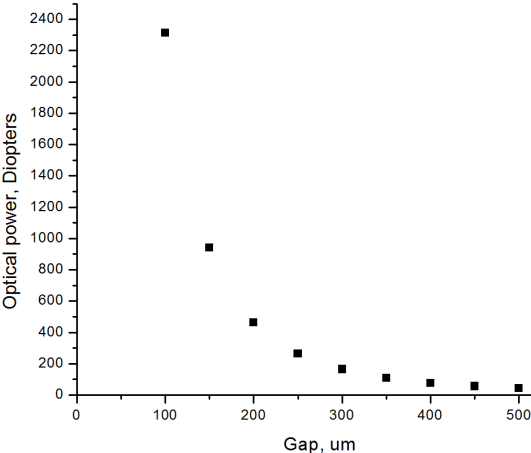


Figure 2.15. Optical power of each microlens depending upon the gap between two neighboring electrodes (the case of “out of plane” switching using patterned electrodes).

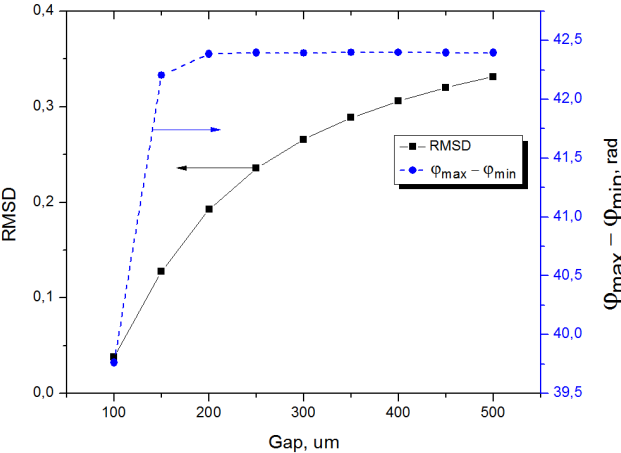


Figure 2.16. Normalized RMS phase retardation deviation from ideal parabolic shape and difference between max and min phase retardation (the case of “out of plane” switching using patterned electrodes).

2.6 Summary and conclusions

We have performed simulations of electrically variable micro arrays based on two approaches (hidden layer and patterned electrode). It is interesting to compare those two approaches, for example,

for the case of microlens arrays. As we can see, from Fig. 2.4 and Fig. 2.14, the MTFs degrade in both cases with the increase of spatial frequency. However, the case of patterned electrodes (the “out of plane” switch) is more “robust” since its MTF is decreasing noticeably only for the spatial scale of $\lambda \leq 150 \mu\text{m}$ (Fig. 2.14), while the DDOH layer approach (Fig. 2.4) shows almost twice smaller MTF already for 3 periods over $2000 \mu\text{m}$ ($\lambda \leq 650 \mu\text{m}$).

The OP of a single microlens (see Fig. 2.5) is non-monotonic. It increases with the increase of spatial frequency and reaches the maximum of 97 D for 5 periods over $2000 \mu\text{m}$ (as aperture radius decreases, see Eq. (2.3)). Further increase of spatial frequency leads to optical power decline (as the phase shift decreases, see Fig. 2.6 and Eq. (2.3)). The optical power’s behavior in the case of patterned electrodes Fig. 2.15) can be explained by analogy.

Obviously, the simple patterned electrode approach can not allow obtaining microprism effect and thus we can not compare two approaches. However, we can see (from Fig. 2.8) that the microprism effect (obtained by the DDOH layer approach) disappears already at $\lambda \leq 400 \mu\text{m}$ (5 periods over $2000 \mu\text{m}$).

2.7 Acknowledgment

This work was made possible thanks to the Canada Research Chair in Liquid Crystals and Behavioral Biophotonics, held by T. G., who received the Manning Innovation Award 2014. We are grateful to the R&D team of Lensvector Inc. and TLCL Optical Research Inc. for their valuable advices.

Chapter 3 Liquid crystal lens with optimized wavefront across the entire clear aperture

Oleksandr Sova¹, Tigran Galstian^{1,2}

¹Center for Optics, Photonics and Laser, Department of Physics, Engineering Physics and Optics, Laval University, Pav. d'Optique-Photonique, 2375 Rue de la Terrasse, Québec, G1V 0A6, Canada

²TLCL Optical Research Inc. and Lensvector Inc., Pav. d'Optique-Photonique, 2375 Rue de la Terrasse, Québec, G1V 0A6, Canada

Optics Communications, Vol. 433: pp. 290-296, 2019

In this chapter we present a study of modal control tunable liquid crystal lens. The concept of modal control was first introduced in the late 90s by Naumov et al. [31]. We have done a theoretical exploration of modifications made to this design, searching for performance improvement. The current chapter consists of the article summarizing our work, which has been published in Optics Communications.

We have built a standard modal control liquid crystal lens of 3 mm clear aperture diameter and characterized it. We have achieved a good agreement between simulation and experimental data after parametric fitting of the sheet resistance of weakly conductive layer was made. Then theoretical model of a 4 mm lens with additional electrodes was considered. The influence of each electrode on resulting wavefront was explained. A design with supplementary floating disk electrode has been successfully implemented in a mobile camera [36,37]. The 4 mm diameter lens was simulated pursuing the goal of creating a relatively wide aperture tunable lens for ophthalmic applications. An example of such a device is an intraocular implant for vision correction [49].

Finally, a modification of conventional design possessing both a floating disk electrode and a powered concentric ring electrode was suggested. Simulations show that significant reduction of aberrations is possible if appropriate control method is used. Aberrations were evaluated by means of comparing simulated wavefront with an ideal one (parabolic). A combination of powering regimes was recommended.

The design that we have proposed demonstrates much better optical performance than traditional approach. At the same time only one additional step of photolithography is required. The resistive-capacitive nature of electric field modulation provides another degree of freedom to control the lens, as both voltages and frequencies are used to tune optical power.

3.1 Résumé

Lentille à cristaux liquides avec front d'onde optimisé à travers la pleine ouverture

Une analyse théorique comparative des performances de trois conceptions de lentilles adaptatives à cristaux liquides est effectuée. Les configurations d'électrode traditionnelle à motif de trou ainsi que d'électrode flottante et d'électrode annulaire supplémentaire sont envisagées dans le cadre d'une lentille de contrôle modal. Le mode de contrôle de ces électrodes et le choix de tension et de fréquence des signaux électriques appliqués sont optimisés pour obtenir un profil sphérique du retard de phase optique à travers la pleine ouverture de la lentille. Cela permettrait l'utilisation efficace de la lentille adaptative en combinaison avec des lentilles à focales fixes de plus grandes ouvertures. Il est montré que nous pouvons améliorer considérablement la plage de variation dynamique acceptable (à faibles aberrations) de la puissance optique de la lentille en changeant le mode de contrôle.

3.2 Abstract

Comparative theoretical analysis of performances of three electrically variable liquid crystal lens designs is conducted. Traditional hole patterned electrode, additional floating and inner-ring electrode configurations are considered within the framework of a modal control lens. The control mode of those electrodes and the choice of the voltage and frequency values of the driving electric signals are optimized to obtain spherical profile of the optical phase retardation across the entire clear aperture of the lens. This would allow the effective use of the tunable lens in combination with larger aperture fixed focus lenses. It is shown that we can improve significantly the acceptable (with low aberrations) dynamic variation range of the optical power of the lens by switching the control mode of electrodes.

3.3 Introduction

3.3.1 Basic design of the lens

Tunable liquid crystal (LC) lenses (TLCLs) [6,23,59,60] have been shown to be very promising candidates for mobile imaging [6,37] and endoscopy [47,61,62] applications. Those demonstrations were covering optical clear apertures (CA) ranging from 0.5 mm to 2 mm. In many other optical systems (which are used in ophthalmology [34,63,64] and augmented reality [65,66]), larger CA values are required where the optical power (OP) variation range of TLCLs is significantly reduced. In those cases, we may consider the combination of a TLCL with larger CA “fixed-focus” optics. However, very high optical quality of TLCL is necessary across its entire CA (see hereafter for details). Before describing those requirements and the solution we propose, let us briefly introduce the operation principle of such lenses: the majority of them are based on the dynamic generation and control of the spatial profile (gradient) of orientation of local anisotropy axis of the LC (the so called director \mathbf{n} , [1]), which in turn, shapes the effective refractive index of the LC material, preferably, in the parabolic form (as gradient index or GRIN lenses):

$$n_{GRIN}(r) = n_c - \frac{r^2}{2fL}, \quad (3.1)$$

where r is the transversal coordinate, n_c is the effective refractive index in the center of the lens, L is the thickness of the LC and f is the focal distance of the lens (measured in meters, the inverse of its OP, measured in diopters, D).

One of the most straightforward approaches (used to generate such a profile) is the combination of uniform and hole patterned electrodes [59]. To reduce the electrical power

consumption of such TLCLs, closest possible position of the above mentioned two electrodes is desired, which necessitates the use of a weakly conductive layer (WCL) [31,67] that is cast over the hole patterned electrode (to avoid using complex multiple concentric electrodes). However, there are several inherent drawbacks (typical for TLCLs) that must be carefully handled in accordance with particular application. One of them (probably the most challenging one) is the non-perfect profile (deviations from Eq. (3.1)) of the obtained refractive index across the entire CA of the lens that is responsible for the generation of its spherical aberrations [36].

The present work aims to resolve this problem. To illustrate its importance, we use here the so called “modal control” (MC) lens [31], shown in Fig. 3.1. The theoretical and experimental analysis of this lens has been widely discussed in the scientific literature [32]. Let us give only a brief description of its design and operation principle. The MC lens is built by using two glass substrates: the bottom substrate is covered with a uniform transparent electrode (UTE), typically made of indium tin oxide (ITO). The top substrate is covered with a WCL (see the green layer in Fig. 3.1) and a hole patterned electrode (HPE, also made of ITO or of a metal, by using photolithography technique). To ensure homogenous (ground state) orientation of LC molecules, a layer of polyimide (not shown here) is cast on internal surfaces of both glass substrates (using spin coating technique), followed by the mechanical “anti-parallel” rubbing (see, e.g. [68]). Those two substrates are then glued together ensuring a uniform gap by means of spacers. The cell is then filled with an LC using capillary effect.

The mechanism responsible for creation of electric field profile may be imagined by considering the UTE, WCL and LC forming a distributed RC circuit, with LC defining the equivalent electric capacitance and resistance (due to the LC’s dielectric losses) and the WCL representing another contribution into the equivalent resistance [31]. This leads to a lag between changes of control voltage in the center of the lens and at the periphery [35], which therefore results in root mean square (RMS) voltage distribution that is close to a parabola (stronger in the periphery than in the center of the lens). The RMS voltage profile can be controlled with frequency changes, enabling not only a voltage control of the resulting refractive index profile and corresponding OP, but a frequency control as well [69].

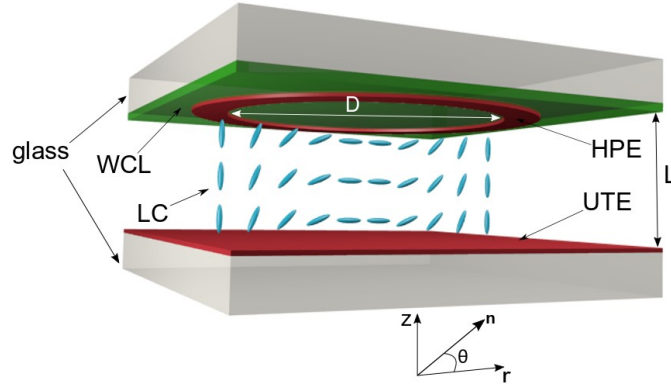


Figure 3.1. Conventional modal control LC lens design, WCL – weakly conductive layer, HPE – hole patterned electrode, UTE – uniform transparent electrode, LC – liquid crystal of thickness L .

3.3.2 Wavefront deformations across the entire clear aperture

As we have mentioned above, this design generates a non-parabolic wavefront that is responsible for spherical aberrations of the lens. In fact, there are two zones over the CA of the lens where the main deviations (from the Eq. (3.1)) appear. As we can see in Fig. 3.2, the generated wavefront (solid line; simulated for a lens with CA=3 mm) is flat in the center of the lens (in the range from 0 to 0.8 mm) as well as in its peripheral regions (in the range from 1.2 mm to 1.5 mm) compared to the desired parabolic form, shown by the blue dashed line.

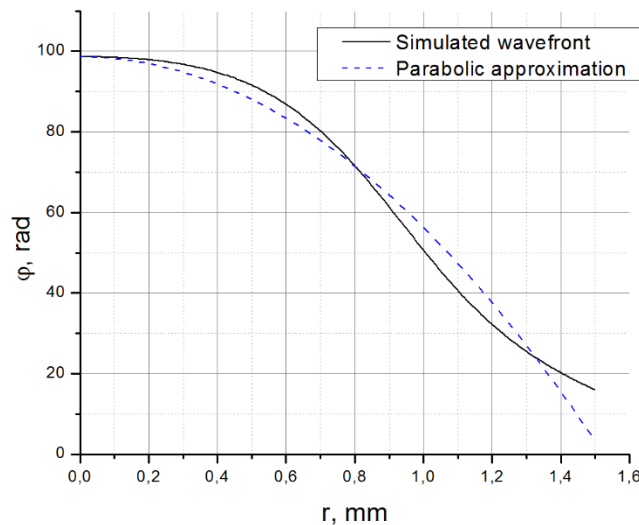


Figure 3.2. Simulated wavefront generated by a standard modal control lens (black solid line) versus the ideal parabolic fit (blue dashed line). $r = 0$ is the center of the lens, while $r = 1.5$ mm is its periphery.

We have already demonstrated [36,37] that the addition of a conductive uncontrolled layer (floating electrode) to the standard MC design can noticeably improve the RMS aberrations, particularly by correcting the wavefront in the center of the lens. In the case of using those lenses in miniature cameras (e.g., in a mobile phone camera), the deviations of the wavefront in the periphery of the lens can be simply hidden behind a diaphragm. This will obviously reduce the effective CA of the TLCL. Thus, the only trade-off here is the larger (compared to the used CA) diameter of the HPE, which, in turn, reduces the OP variability range (although, the remaining CA appears to be very close to the parabolic form [36,37]).

However, for certain optical systems (such as those used in ophthalmology and augmented reality) larger CAs are required. The inherent nature of the GRIN TLCL imposes a quadratic reduction of its OP variability range with the increase of its CA. Thus, the TLCL cannot be used for those purposes (we do not consider here the case of diffractive TLCLs because of their wavelength dependence and discrete character of control, while they can perform very well for some specific applications [70,71]). Fortunately, it is quite possible to combine a TLCL of small CA (e.g., from 3 mm to 4 mm) with a fixed lens of larger CA (e.g., from 6 mm to 10 mm) to build the above-mentioned optical systems with large CAs. The use of a diaphragm (as in a mobile phone camera) becomes highly undesired here. In this case, it is very important to have the best possible (parabolic) wavefront profile across the whole CA of the TLCL.

In the current work, we perform a detailed theoretical analysis of several TLCL designs (with modifications of the MC lens design) and show that the appropriate configuration of electrodes and the correct choice of the voltage and frequency values of the driving electric signal may improve significantly the acceptable (with low aberrations) dynamic variability range of the OP. In particular, we identify conditions (by switching the control mode) allowing to obtain spherical profile of the optical phase retardation across the entire CA of the lens.

3.4 Analysis of the modal control lens

3.4.1 Theoretical model

We have used a previously discussed procedure [37] for the theoretical analysis of this lens. Thus, we have derived the following system of coupled partial differential equations that describes the reorientation of LC's molecules in the presence of an external electric field E :

$$\begin{cases} \theta_{zz} + \frac{\varepsilon_0 \varepsilon_a}{2K} \sin(2\theta) E_z^2 = 0 & (3.2a) \\ \nabla \left(\left(\varepsilon_0 \varepsilon + i \frac{\sigma}{\omega} \right) \nabla V \right) = 0, & (3.2b) \end{cases}$$

where θ is the director's tilt angle (see also Fig. 3.1), K is the elastic constant (one constant approximation is used; $K_{33}=K_{11}=K$), ε_0 is the dielectric constant of vacuum, ε_a is the LC's dielectric anisotropy, σ is the conductivity, V is the electric potential and ω is the angular frequency of the electric field. A cylindrical coordinate system is considered here. We also assume strong anchoring of LC molecules at the interfaces with glass substrates. The above mentioned system of partial differential equations is solved numerically using Comsol Multiphysics finite element analysis software and MATLAB numerical computing environment. Equation (3.2a) is solved only in the LC material domain, while Eq. (3.2b) is solved in all domains (LC, WCL, glass). In an isotropic medium ε is a constant while, for the LC layer, it is a tensor of second order $\varepsilon_{ij} = \varepsilon_{\perp} \delta_{ij} + \varepsilon_{\parallel} n_i n_j$ (where \mathbf{n} is the director; ε_{\perp} and ε_{\parallel} are complex valued, see the next section). As the diameter of the lens (between 0.5 mm - 5 mm) is much larger than the thickness of the LC layer (50 micrometers), we neglect all radial components in our equations.

Knowing the spatial distribution of LC's director \mathbf{n} , we calculate the effective refractive index and phase retardation that a normally incident extraordinary polarized beam acquires at the exit of the cell [72]:

$$n_{eff} = \frac{n_o n_e}{\sqrt{n_e^2 \sin^2 \theta + n_o^2 \cos^2 \theta}}, \quad (3.3)$$

$$\varphi = \frac{2\pi}{\lambda} \int_0^L n_{eff}(r, z) dz, \quad (3.4)$$

where z is the longitudinal coordinate (light propagation direction) and r is the transversal coordinate (in the plane of cell substrates). Then OP and RMS wavefront errors are determined from fitting the obtained phase retardation profile with a parabolic function:

$$\varphi(r) = \varphi(0) - \frac{\pi r^2}{\lambda f}, \quad (3.5)$$

where $\varphi(0)$ is the phase retardation in the center of the lens, λ is the incident beam's wavelength, f is the focal length of the lens. The total RMS wavefront error was calculated (it accounts only for RMS spherical aberrations (SAs) due to the axial symmetry of our system) using the following formula [73]:

$$RMS SA = \sqrt{\frac{1}{N} \sum_{i=1}^N (\Delta W_i)^2 - \left(\frac{1}{N} \sum_{i=1}^N \Delta W_i \right)^2}, \quad (3.6)$$

where $\Delta W_i = W_i^{ideal}(r_i) - W_i^{simulated}(r_i)$ is the difference between the ideal and simulated wavefront surfaces at r_i , N – number of steps along the r coordinate; $W_i = (\lambda/2\pi)\phi$.

3.4.2 Comparison with experimental results

For the purpose of model validation, we have created a standard MC lens and characterized it. An experimental setup, shown in Fig. 3.3, was used for the measurements of the OP and spherical aberrations of our lenses. The first polarizer (2) was used to control the intensity of the probe beam (obtained from a CW He-Ne laser (1), operating at $\lambda = 632.8$ nm), while the second polarizer (2) was used to align its polarization (parallel to the rubbing direction of the LC cell's substrates). Then the beam was expanded (3) before its normal incidence on the TLCL (5), which was controlled by the HP Agilent 33120A function generator (4). A relay lens (6) was used to image (with an adjusted spot area) the output of the TLCL on the input of the Thorlabs WFS10-7AR Shack-Hartmann sensor (7).

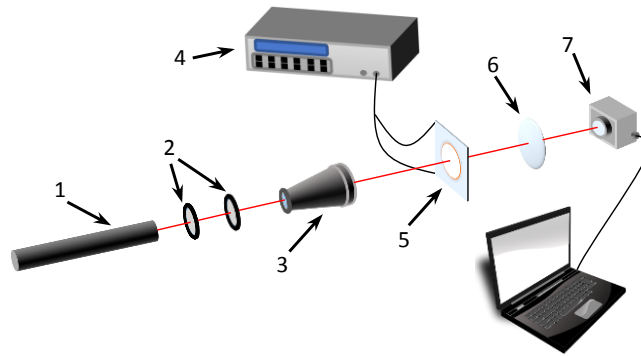


Figure 3.3. Schematic representation of the experimental setup used for measuring the OPs and SAs of TLCLs: 1) He-Ne laser, 2) polarizers, 3) beam expander, 4) function generator, 5) TLCL, 6) relay lens, 7) Shack-Hartmann wavefront sensor.

The measurement procedure consisted of the following steps: 1) the TLCL is placed on a stage and aligned; 2) a reference measurement is taken with the Shack-Hartmann sensor in the ground state of the lens; 3) a control voltage (at 1 kHz) is applied; 4) the frequency of the control voltage is increased (from 1 kHz) and the values of Zernike coefficients are recorded in real time using sensor's software; 5) obtained data is processed by a computer (OPs and RMS SAs are calculated). Each measurement was repeated three times.

To take into account the dielectric losses and the dispersion of relative permittivities, we have developed an experimental set-up and procedure to measure them. The setup consists of a signal generator, digital multimeter, custom-made printed circuit board (PCB) and oscilloscope. A planar oriented LC cell is connected in series with a pair of adjustable resistor R and capacitor C (in parallel), which are mounted into the PCB. An input signal that passes through the R - C pair with known values and the LC cell (which can be equivalently represented as R and C in series) is provided. The amplitudes of two output signals and phase difference between them are measured (one signal is measured between ground and known R - C pair, the other one is measured between ground and R - C pair with LC cell connected in series). The capacitance and resistance values of the LC are calculated from the collected data for a range of voltages and frequencies. The dependences of real and imaginary relative permittivities at low voltages (planar orientation of LC, corresponds to the perpendicular component of permittivity ϵ_{\perp}) and high voltages (well above the reorientation threshold [1,9] providing homeotropic orientation of the LC; corresponds to the parallel component of permittivity ϵ_{\parallel}) were obtained (Fig. 3.4, see also [74]).

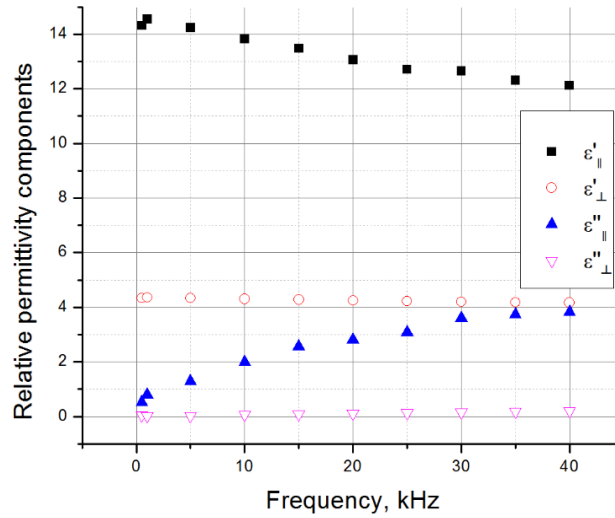


Figure 3.4. Experimentally measured dependences of real and imaginary relative permittivities (parallel and perpendicular components) of LC material upon applied signal's frequency.

These dependences were approximated with linear functions and implemented in our model. The elastic constant K_{11} was determined from measurements of transmission's dependence upon the voltage applied to a planar LC cell (placed between crossed polarizers and oriented at 45° relative to the rubbing direction of the cell). The only unknown parameter was the sheet resistance R_s of the WCL (changing from part to part). We have used it as a fitting parameter in our model. Table 3.1 summarizes the input data for our further simulations:

Table 3.1. Parameter values used for simulations.

Parameter	Value	Description
λ	630 nm	Wavelength
L	60 μm	Cell thickness
D	3 mm	Diameter of HPE
U_{ce}	5 V_{rms}	Voltage (sine wave) applied to the HPE, named furthermore as control electrode (CE)
θ_l	3°	Pretilt angle
K	13.38 pN	Elastic constant
R_s	31.61 MOhm/sq	Sheet resistance of the WCL (value obtained from fitting)
ϵ_{WCL}	20	Permittivity of the WCL
n_o	1.519	Ordinary refractive index of the LC
n_e	1.738	Extraordinary refractive index of the LC

Despite the fact that this model is rather simplified, after finding the value of R_s (using the Nelder-Mead algorithm, see [75]), we obtain a good quantitative agreement with our experimental results (Fig. 3.5 (a)) for the OP's dependence upon the electrical driving frequency (at fixed driving voltage of $U_{ce}=5 V_{\text{rms}}$). At the same time, a rather good qualitative agreement is also obtained for the corresponding RMS SAs (Fig. 3.5 (b)). The objective of fitting was to find a value of R_s that would minimize the difference between simulated and measured values of OP at 28 kHz (the value of R_s is defined by the material properties of the WCL and does not change during operation of the TLCL).

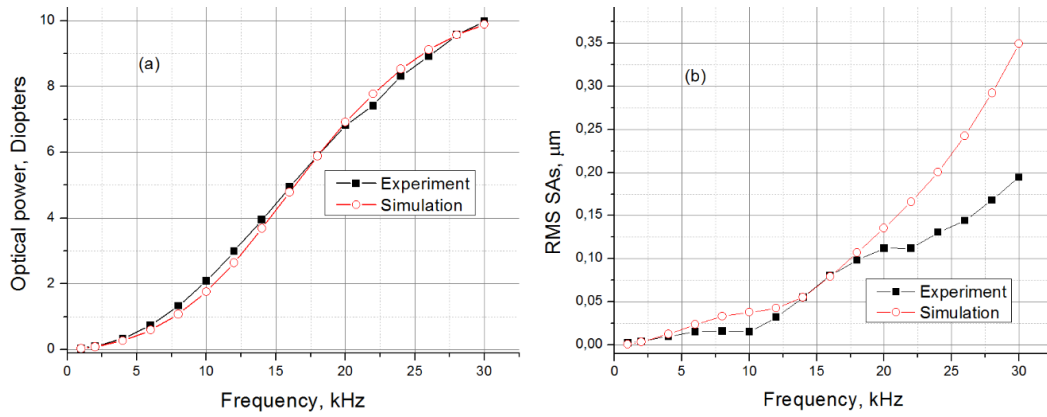


Figure 3.5. (a) Comparison of simulated (open circles) and measured (filled squares) dependences of the OP of the standard modal control TLCL upon the driving frequency. (b) Comparison of corresponding RMS spherical aberrations vs frequency. Applied voltage is 5 V_{rms} . The clear aperture is 3 mm.

There are several factors that can be at the origin of the mismatch between the simulated and measured values of RMS SAs. Some parameters (e.g., permittivities) can vary due to impurities present in the LC; we also use several approximations (mentioned above) to facilitate our numerical calculations, etc. Nevertheless, we consider that the obtained overall agreement validates our model and we can thus use it to introduce and to analyze several modified TLCL designs trying to improve the wavefront's shape across the CA.

3.5 Wavefront improvement

3.5.1 Proposed design modification

The suggested modifications of the MC lens design are schematically shown in Figs. 3.6 (a)-(c). In Fig. 3.6 (a) we present the first modification where the main difference (compared to the standard MC lens) is an additional “inner ring” electrode (inside the HPE), that is controlled (independently from the HPE) via a small opening in the HPE [76].

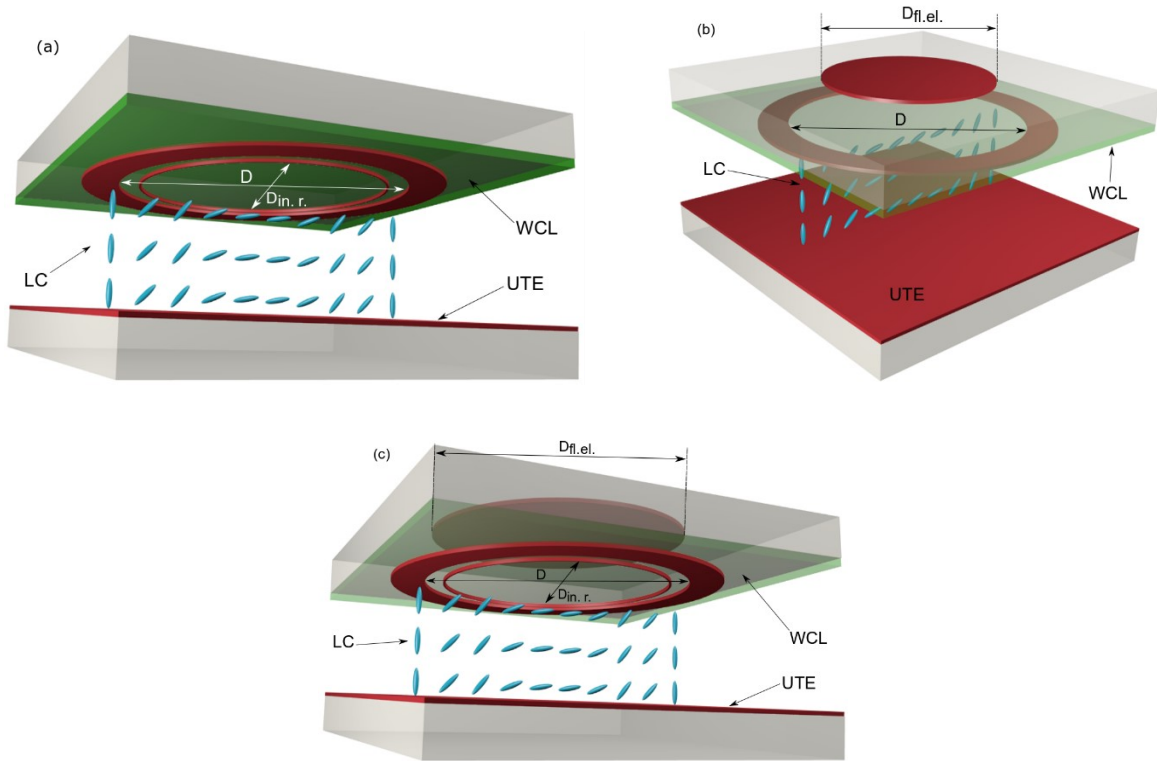


Figure 3.6. Schematics of modified modal control lens designs. (a) MC lens with inner ring electrode ($D_{in.r.}$ – diameter of the inner ring electrode); (b) MC lens with a floating electrode ($D_{fl.el.}$ – diameter of the floating electrode); (c) a design combining components of (a) and (b).

For further discussions, we shall call the HPE a “control electrode” (versus the “inner electrode”, introduced here). This change provides an additional control tool that reshapes the wavefront in the periphery of the lens, reducing its deviation from an ideal form (see Fig. 3.2).

In Fig. 3.6 (b) we show another design, based on a floating electrode [36]. This approach introduces additional capacitance for the equivalent electric circuit, which changes the effective impedance of the structure and therefore redistributes the electric potential in the LC cell. This design reduces the flatness of the wavefront in the center of the lens (see Fig. 3.2).

Finally, Fig. 3.6 (c) demonstrates the combination of two previous modifications (inner and floating electrodes).

In the context of ophthalmic applications, we are interested in TLCLs with larger CA (>3 mm, given that the minimum diameter of the pupil at high illumination conditions is ≈ 3 mm in average) that must provide OP variation from zero up to the range of 2.5 – 3 diopters (given that the global loss of accommodation by the average population is ≈ 3 D, see [77]). In addition, the RMS SA values of this lens must remain below $0.1 \mu\text{m}$ over the entire range of OP variations. To simulate the behavior of such a lens, we start by considering a standard MC lens with a $D=4$ mm diameter of the HPE and LC layer of $L=40 \mu\text{m}$ (Fig. 3.7). The rest of simulation parameters, used here, are listed in Table 3.1.

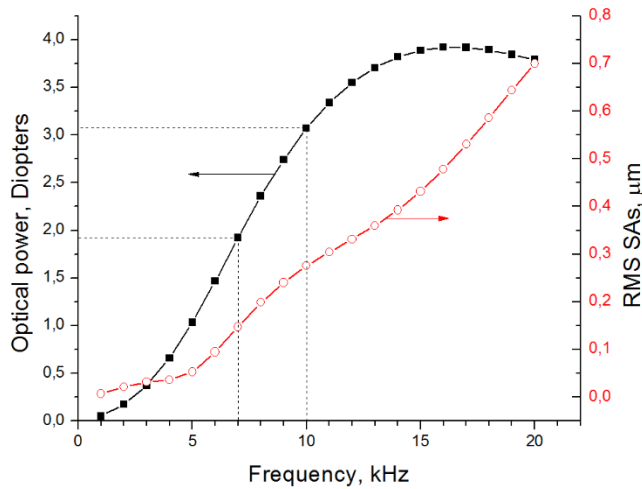


Figure 3.7. Optical power (filled squares) and RMS SAs (open circles) simulated for a standard modal control lens with 4 mm clear aperture.

Obtained results show that the $OP \approx +2$ D is achieved at about $f=7$ kHz, while the $OP \approx +3$ D is achieved at $f=10$ kHz (the voltage applied to the control electrode is $U_{ce}=5$ V_{rms} in both cases; this choice was made as an approximate tradeoff between the achievable OP and aberrations, without detailed optimization).

In order to meet the requirement of low SA (≤ 0.1 μm), we ran a series of simulations, using the Nelder-Mead multivariable optimization method, with constrained input variables (based on Matlab's "fminsearch" function). All parameters resulting from this optimization are listed in Table 3.2.

Table 3.2. Optimization parameters and constraints.

Design	Optimized values		Constraints	
			min	max
MC + inner ring	$R_{in.r.}$	1.76 mm	1.4 mm	1.9 mm
	$U_{in.r.}$	3.65 V _{rms}	1 V _{rms}	10 V _{rms}
	U_{ce}	10.36 V _{rms}	3 V _{rms}	20 V _{rms}
MC + floating electrode	$R_{fl.el.}$	1.35 mm	0.1 mm	1.6 mm
	U_{ce}	3.23 V _{rms}	1 V _{rms}	20 V _{rms}
MC + inner ring + floating electrode	$U_{in.r.}$	2.76 V _{rms}	1 V _{rms}	10 V _{rms}
	$R_{in.r.}$	1.75 mm	1.4 mm	1.9 mm
	$R_{fl.el.}$	1.35 mm	0.1 mm	1.8 mm
	U_{ce}	5.08 V _{rms}	1 V _{rms}	20 V _{rms}

For correct evaluation of wavefront quality, we have normalized them and compared with ideal parabolas. Without normalization the Nelder – Mead method would gradually increase the voltage on the control electrode (U_{ce}) with each iteration, until it would have reached predetermined upper limit. This happens because with the increase of U_{ce} all molecules in the LC become reoriented ($\theta \approx 90^\circ$) practically in the entire cell (considering that we are using constant value of frequency). Therefore, the effective refractive index is almost the same in the center and at the periphery of the lens, causing the RMS SAs to decrease. On the other hand, by using normalized wavefronts, we have observed that the optimal values of considered parameters could be found within established reasonable limits. For all simulations solver's stopping criteria were achieved (with default values of "TolFun" and "TolX" parameters used by "fminsearch" function).

3.5.2 Comparison of aberrations

Figure 3.8 demonstrates optimized RMS SAs versus the OP for previously discussed electrode geometries. As we can see, the traditional MC lens has a useful dynamic range (RMS SA $\leq 0.1 \mu\text{m}$) of OP variation up to 1.5 D that is certainly not good enough. The use of an additional inner ring electrode extends this zone up to 2 D; while the floating electrode alone extends this zone up to 2.8 D. This last approach can already be acceptable for the target application. However, the use of the combination of the floating and inner ring electrodes seems to be capable of extending it up to 3.6 D (see discussions hereafter).

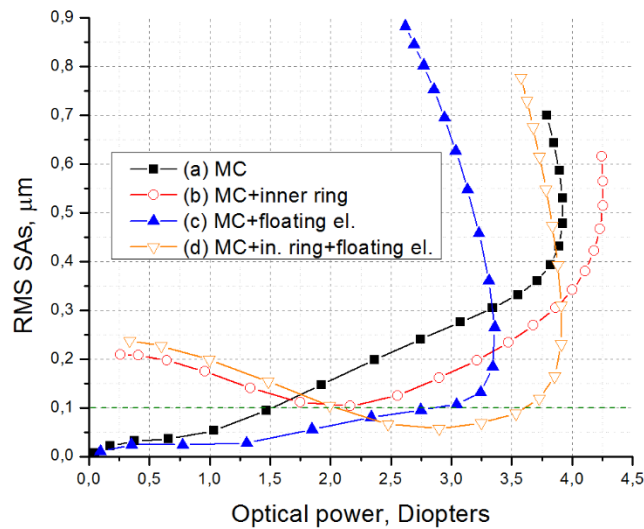


Figure 3.8. Comparison of RMS spherical aberrations vs optical power for different designs of optimized MC lenses: (a) MC; (b) MC+inner ring; (c) MC+floating electrode; (d) MC+inner ring+floating electrode.

To visualize the impact of each approach on the phase of the incident beam, we use the normalized wavefronts (Fig. 3.9 (I)) and deviations from spherical phase retardations (Fig. 3.9 (II)) that were calculated for the example of control frequencies corresponding to the OP of +3 D for each case.

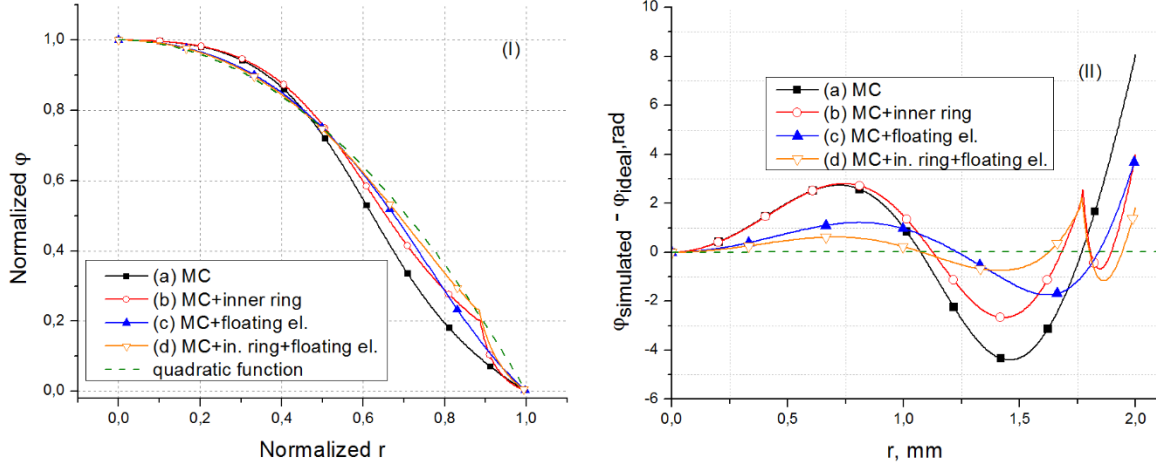


Figure 3.9. (I) Normalized wavefronts and (II) deviations of phase retardation from the ideal shape: (a) MC; (b) MC+inner ring; (c) MC+floating electrode; (d) MC+inner ring+floating electrode.

Design (b) corrects wavefront's shape at the periphery of the lens due to director's reorientation caused by the voltage applied to the inner ring ($U_{in.r.}$). At the same time, we notice the deviation from the ideal shape (green dashed line, Fig. 3.9 (I)) appearing in the center (between 0.2 and 0.4 values of normalized r coordinate). On the other hand, design (c) makes the wavefront approach the quadratic function in this zone and at the periphery simultaneously. Although designs (b) and (c) are clearly better than conventional MC design (a), we can further decrease the SAs by combining inner ring and floating electrodes. Design (d) shows the advantage of this concept and, as one would expect, improves wavefront's shape in both zones, thus providing the lowest spherical aberrations across the entire CA of the lens.

3.6 Discussion

Figure 3.8 clearly shows that each design has unique dependences of RMS SAs upon the OP values. Thus, we should take this into account when choosing the way how to drive those lenses for specific applications. For example, design (d) (see Fig. 3.8) has low RMS SAs for optical powers between +2.25 D and +3.5 D, but design (c) is better for $OP < +2.25$ D. Therefore, we think that one possible way of obtaining rather large OP variation range with low RMS aberrations would be to build a lens having both electrodes and then to "switch" the control mode between these two designs. To demonstrate the feasibility of such an approach, we have simulated a lens with both inner ring and floating electrodes, but for optical powers below +2.5 D, we consider our inner ring as a floating electrode and for optical powers above +2.5 D, we apply to it an optimal voltage (the same as found in our previous calculations). Interestingly enough the optimized values of radii $R_{in.r.}$ and $R_{fl.el.}$ of

design with combined electrodes appear to be approximately the same as in two other designs, where only one additional electrode is used (see Table 3.2). In the case when both electrodes are floating, we obtain slightly higher aberrations than when we use a floating disk electrode alone. Nevertheless, RMS SAs still do not exceed $0.1 \mu\text{m}$, as shown in Fig. 3.10. By powering the inner ring electrode, we can switch to a regime where the RMS SAs start decreasing (see blue filled triangles for $OP > +2.25$ D) instead of increasing (black filled squares for $OP > +2.25$ D).

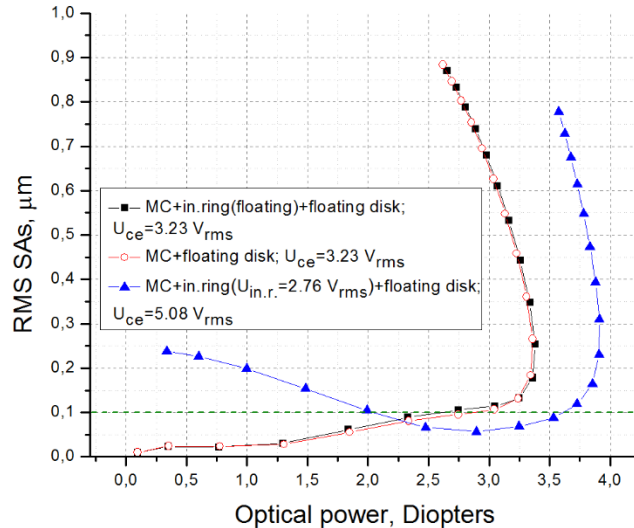


Figure 3.10. RMS SAs of optimized lens with combined additional electrodes.

3.7 Conclusions

Three alternative designs of MC TLCLs were analyzed. Optimal control parameters were found for each modification. Dynamic range of OP with low RMS SAs that are suitable for ophthalmic applications ($< 0.1 \mu\text{m}$) can be significantly increased if an appropriate design and control modality (proposed here) are used. The influence of each additional electrode (powered inner ring electrode, floating disk electrode and their combination) on resulting phase retardation has been characterized. The best configuration and control process have been identified to obtain closely parabolic wavefront across the entire clear aperture of the lens. The suggested design and control technique introduce a modified MC lens with 4 mm clear aperture, very low RMS spherical aberrations ($< 0.1 \mu\text{m}$) and a dynamic range of 3.5 diopters.

3.8 Acknowledgments

We thank the Optics Laboratory of LensVector Inc. for the use of their lenses and equipment. This research was also supported by the Canada Research Chair in Liquid Crystals and Behavioral Biophotonics, held by T. G., who also has received the Manning Innovation Award 2014.

Chapter 4 Modal control refractive Fresnel lens with uniform liquid crystal layer

Oleksandr Sova¹, Tigran Galstian^{1,2}

¹Center for Optics, Photonics and Laser, Department of Physics, Engineering Physics and Optics, Laval University, Pav. d'Optique-Photonique, 2375 Rue de la Terrasse, Québec, G1V 0A6, Canada

²TLCL Optical Research Inc. and Lensvector Inc., 2375 Rue de la Terrasse, Québec, G1V 0A6, Canada

Optics Communications, Vol. **474**: 126056, 2020

One of the biggest challenges of tunable liquid crystal lenses is the creation of a wide aperture lens without the loss of optical power. In this chapter we address this problem continuing the use of modal control principle. The solution that we propose is a refractive modal control Fresnel lens.

An existing switchable liquid crystal-based Fresnel lens introduced by Bos et al. [27] requires the use of numerous electrodes. Furthermore, several photolithography steps complicate the experimental process and increase the unit price of such a lens. We propose a Fresnel lens where the abrupt jump of optical phase is achieved using a pair of thin concentric ring electrodes. Similar to the lens described in the previous chapter, the weakly conductive layer defines electric field potential distribution within LC cell.

We have constructed a prototype of such a lens and performed a series of tests combining it with a commercially available camera. The lens was also characterized using interferometric-polarimetric measurements. Obtained results show that higher optical power can be reached in comparison with a reference lens of the same diameter. A theoretical model of modal control Fresnel lens was presented. Although aberrations of the first prototype are rather high, theoretical optimization of control voltages and frequencies gives the possibility of achieving better image quality. This chapter is based on the article published in Optics Communications. The discussed approach is very promising as it allows to create wide aperture lenses with thin cell gaps, thus avoiding the issues of scattering and long excitation times. Moreover, the optical power can be maintained at the same level despite the increase of lens diameter.

4.1 Résumé

Lentille de Fresnel réfractive de contrôle modal avec une couche uniforme de cristaux liquides

Nous présentons l'étude expérimentale et théorique d'une conception de lentille de Fresnel réfractive basée sur le principe de contrôle modal. La comparaison de sa performance avec une lentille similaire mais à l'ouverture unique (6 mm) montre que la lentille de Fresnel suggérée peut atteindre des puissances optiques plus élevées (supérieures à 3 dioptries). Un mode de contrôle combiné est proposé afin d'optimiser son fonctionnement pour les distances focales différentes. La modélisation théorique démontre la possibilité d'améliorer encore les aberrations grâce à une technique de contrôle optimisée.

4.2 Abstract

We present the experimental and theoretical study of a refractive Fresnel lens design based on the “modal control” principle. Comparison of its performance with a similar but single aperture (6 mm) lens shows that the suggested Fresnel lens can achieve higher optical powers (above 3 diopters). A combined control mode is suggested to optimize its operation for different focal ranges. Theoretical modeling demonstrates the possibility of further improvement of its aberrations by means of an optimized driving technique.

4.3 Introduction

Typical electrically tunable liquid crystal (LC) lenses (TLCLs) have optical apertures ranging from 0.3 mm to 2 mm, adapted for such applications as endoscopy [47,78,79], mobile imaging [4,5], and ophthalmology [34,49,70,80–82]. However, several emerging applications, including augmented reality [83,84], near to eye devices [64,85] or intraocular implants [42,49], require larger clear apertures (up to 8 mm, as the pupil size of human eye varies from 2 to 8 mm, depending upon person’s age and illumination conditions [86]). At the same time, it is well-known that with the increase of the clear aperture’s radius (R_{ca}), the maximal achievable optical power (OP) of a single aperture refractive gradient index (GRIN) TLCL decreases quadratically [15,23,60]:

$$OP_{\max} = \frac{2(n_c - n_p)L}{R_{ca}^2}, \quad (4.1)$$

where n_c and n_p are the effective refractive index values, respectively, in the center and at the periphery of the lens and L is the thickness of the LC layer.

One possible way to compensate the loss of OP, occurring with the increase of TLCL’s aperture, is to increase the thickness of LC. However, this leads to a quadratic increase of excitation (τ_{excit} , Eq. (4.2)) and relaxation (τ_{relax} , Eq. (4.3)) times [18] of the molecular reorientation:

$$\tau_{excit} = \frac{\tau_{relax}}{\left| \left(\frac{V}{V_{th}} \right)^2 - 1 \right|}, \quad (4.2)$$

$$\tau_{relax} = \frac{\gamma_1 L^2}{\pi^2 K}, \quad (4.3)$$

where γ_1 is the rotational viscosity of the LC, K is the elastic constant (under the small angle and single constant approximation: $K=K_{11} \approx K_{33}$, where K_{11} and K_{33} are, respectively, the splay and bend elastic constants) of the LC, V_{th} is the threshold voltage and V is the applied voltage. More detailed

discussion on the estimation of excitation and relaxation times of molecular reorientation may be found in [87]. In addition, undesired scattering effects, which diminish the image quality, become more pronounced [1,37,88].

There is an alternative approach of *diffractive* Fresnel lenses, that can operate with rather small values of L [71]. They have several advantages including short focal lengths (e.g., several cm), large diameters (e.g., from a few mm to several cm), and fast response times (few milliseconds). Their weaknesses are the strong chromatic aberrations, the absence of continuous focus-tuning and the high precisions required during manufacturing (the work on reducing the chromatic aberration [89] and on providing multiple discrete focal length options continues). A number of difficulties (even more complex manufacturing) are also present for alternative solutions using non-uniform LC gap [90–94]. To eliminate the above-mentioned problems, all flat (with uniform LC gap) *refractive* Fresnel lenses have been studied [27,95]. However, this approach also has drawbacks, particularly the large number of required electrodes.

To reduce the number of electrodes, an alternative approach of *refractive* Fresnel lens was suggested without a detailed study [96]. In the present work, we have modeled, built and characterized such a lens as one possible solution of challenges described above. Namely, we propose a GRIN refractive Fresnel type TLCL with relatively large clear aperture ($D_{ca} = 6$ mm) and small (3) number of control electrodes. This approach is based on a well-known “modal control” TLCL (MC-TLCL) [31]. We are presenting experimental results, showing that the proposed TLCL can achieve higher OP values compared to the conventional MC-TLCL of the same aperture size. A combined control mode is then suggested to optimize its operation for different focal ranges. Theoretical modeling is also presented demonstrating the possibility of further improvement of its root mean square (RMS) aberrations by means of optimized driving.

4.4 Experimental method and materials

We shall start with a description of a conventional MC-TLCL [31] that will help to introduce the proposed lens. The most important element of this lens is a semiconductor layer that is cast on one of substrates of the lens, forming a highly resistive or weakly conductive layer (WCL). Then this substrate is covered with a thin layer of a hole patterned electrode (concentric ring electrode (CRE), made e.g., from indium tin oxide (ITO)) obtained by photolithography. A uniform transparent electrode (UTO, made of ITO) is cast on the second substrate. Thin polyimide films are also spin-coated on both substrates, baked and rubbed to ensure a homogeneous orientation of LC molecules. Then, these substrates are glued together by means of a UV curable adhesive, containing spacers to

control the gap between them (defining the thickness of the LC). Finally, the cell is filled with a nematic LC (NLC) and external electric connections are fabricated by using conductive adhesives. Such MC-TLCL can be described as a spatially distributed RC circuit, with WCL representing mainly the equivalent resistance and the NLC representing a resistance and capacitance in parallel [31,33]. The attenuation (in space) of the electric potential with the help of this RC circuit is the mechanism of creating nearly quadratic refractive index distribution in this design (see also [67]). Unlike most TLCL designs, here the OP value can be adjusted not only with the electric potential variations, but also by changing the frequency of the applied voltage [31,33,37,96].

In this paper we are exploring a modified version of the MC-TLCL, which has two supplementary electrodes (see Fig. 4.1). These concentric ring electrodes divide the lens into two zones: inner zone, where an incident plane wave acquires (at the exit of the cell) the main parabolic phase distribution and an outer zone, which provides extra phase retardation. Thus, we are dealing with a refractive type Fresnel lens with one additional zone and, most importantly (for the ease of fabrication), without any surface relief structures inside the NLC's cavity. We could further call it a Fresnel MC-TLCL (or F-MC-TLCL). Indeed, the main difference of this design (originally proposed in [96], but neither studied nor reported) from previous implementations is the use of a uniform NLC layer (flat LC gap) [25] and a very small number of electrodes (compared, for example, with [27]) thanks to the presence of the WCL (see hereafter). Obviously, there is also a transition zone that is slightly larger (due to the fringing field) than the widths of inner electrodes and the gap between them combined.

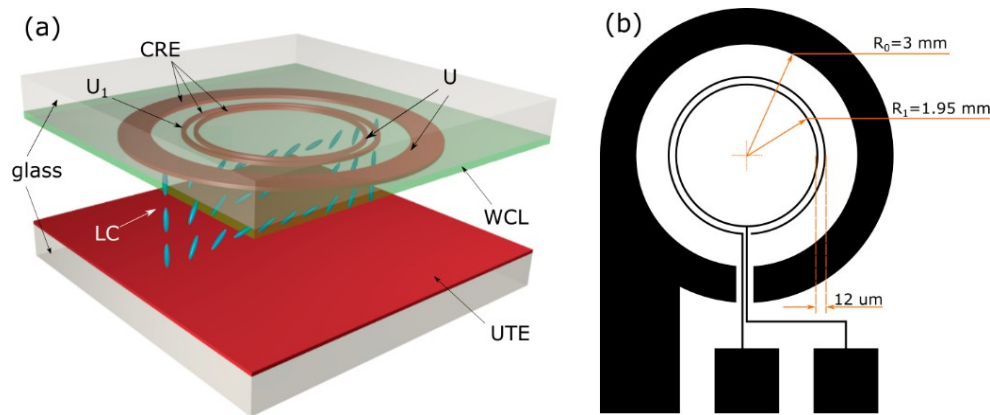


Figure 4.1. Schematic presentation (a) and top substrate electrode pattern (b) of the studied Fresnel lens; WCL - weakly conductive layer, CRE – concentric ring electrodes, UTE - uniform transparent electrode, LC – liquid crystal.

This lens offers very rich control possibilities, but to start with, we have applied the same voltage U to the innermost and outermost electrodes, while the voltage, applied to the middle electrode, was kept lower ($U_I < U$). This ensures a jump of the electric potential within the aperture, creating a zone where the direction of the NLC's local average molecular orientation (the so called *director* [1]) changes relatively abruptly. Consequently, a phase retardation profile of a Fresnel lens is obtained.

To fabricate such a structure, a 100 μm thick top glass substrate was first coated with a WCL (TiOx layer with approximately 20 MOhm/sq of sheet resistance R_s , see hereafter). Then a 50 nm layer of chrome was deposited on the top of the WCL using thermal evaporation method. Then, three concentric ring electrodes were obtained (from the chrome layer) by using a standard photolithography technique. The total width of two inner ring electrodes with the gap in between was of about 12 μm . A small opening of 20 μm was made in the outermost ring electrode to provide electric connections to two inner rings. The bottom 500 μm thick substrate was coated with a uniform layer of ITO. Then layers of polyimide (Nissan SE-150 PI) were spin coated on both substrates and baked. The obtained PI layers were then rubbed in antiparallel directions. Nordson Asymtek fluid dispenser machine was used to precisely distribute UV glue mixed with 60 μm spacers to ensure uniform cell gap. Finally, two substrates were sandwiched together and the cell was filled with 5CB NLC using capillary method. The choice of 5CB was made in view of easier comparison of our experimental and theoretical results since the needed parameters of this LC are well known [55,97].

4.5 Experimental results

4.5.1 Interferometric-polarimetric measurements

In order to characterize the optical performance of the lens, an interferometric-polarimetric method was used. The lens was placed between crossed polarizers of a polarizing microscope (with the rubbing direction oriented at 45° relative to polarizers (see, e.g., [68]). The lens was powered using two separate sine wave generators. One of them was connected to the innermost and the outermost ring electrodes and the other one was connected only to the middle electrode. The bottom substrate (covered with uniform ITO) was used as a common ground for both generators. Voltage applied to the innermost and outermost electrodes was chosen to be $U = 4 V_{\text{rms}}$ and two different values of voltages ($U_I = 0.35 V_{\text{rms}}$; $2 V_{\text{rms}}$) were applied to the middle electrode. Since the MC-TLCLs can be also controlled by frequency [32,36], a range of frequencies, varying from 1 to 30 kHz (with 1 kHz steps), was chosen for our measurements. Several examples of interference fringes with different combinations of voltage and frequency are shown in Fig. 4.2:

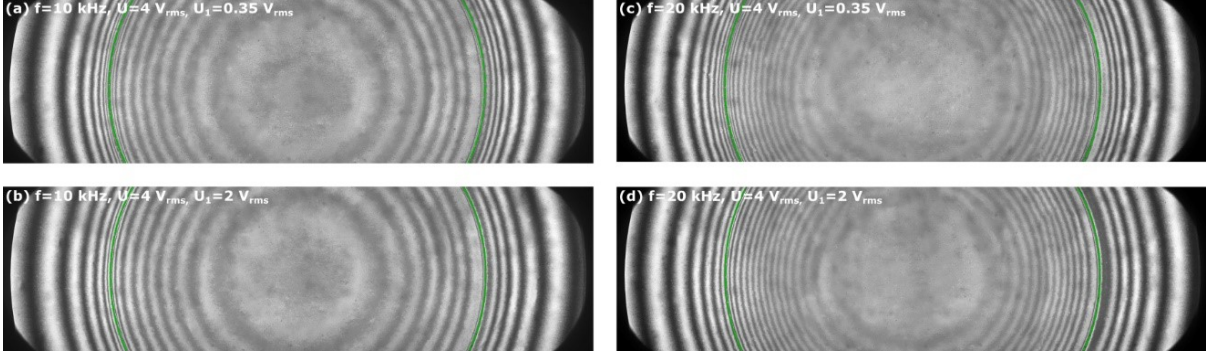


Figure 4.2. Observed interference fringes obtained with the F-MC-TLCL placed between crossed polarizers. Green dashed lines separate inner and outer zones. $U = 4 \text{ V}_{\text{rms}}$, (a) $f=10 \text{ kHz}$, $U_i=0.35 \text{ V}_{\text{rms}}$; (b) $f=10 \text{ kHz}$, $U_i=2 \text{ V}_{\text{rms}}$; (c) $f=20 \text{ kHz}$, $U_i=0.35 \text{ V}_{\text{rms}}$; (d) $f=20 \text{ kHz}$, $U_i=2 \text{ V}_{\text{rms}}$.

A 10X/0.25 plan achromatic objective (Olympus) with working distance of 10.6 mm was used to better distinguish interference fringes in the proximity of inner electrodes. Due to objective's limited field of view and the large size of F-MC-TLCL's aperture, six consecutive overlapping pictures of interference fringes were recorded and joint (stitched) together during image processing. The movement of the lens (secured by the stage) was controlled with MAC 5000 automation controller system (Ludl Electronic Products). In Fig. 4.2 (a)-(d), the rubbing direction of the PI layer is from left to right. Knowing that the phase delay between two neighboring interference minima or maxima is 2π , we can reconstruct the wavefronts (see Fig. 4.3).

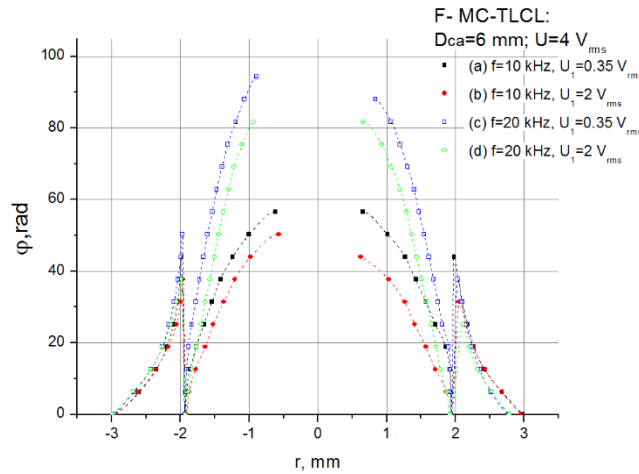


Figure 4.3. Reconstructed phase profiles for the proposed F-MC-TLCL. Dashed lines are for eye guiding only.

It should be noticed that the recorded wavefronts (in Fig. 4.3) are slightly asymmetric. This asymmetry is observed because the measurements are made along the director's ground state orientation plane (rubbing direction) and it is the consequence of the director's "pretilt" angle [68] (the ground state angle with respect to glass surfaces) that ensures the absence of disclinations. Another factor, contributing in the asymmetry is the design of middle ring electrode on the top substrate. No data point could be retrieved in proximity to $r=0$ (in Fig. 4.3) because no further 2π phase steps were present in this zone (Fig. 4.2).

Using a parabolic approximation (Eq. (4.4)) of reconstructed phase profiles

$$\varphi(r) = \varphi_0 - OP \cdot \left(\frac{\pi}{\lambda}\right) r^2, \quad (4.4)$$

where φ_0 is phase retardation in the center of the aperture, we have obtained the dependences of OP and RMS wavefront errors upon driving frequency shown in Fig. 4.4.

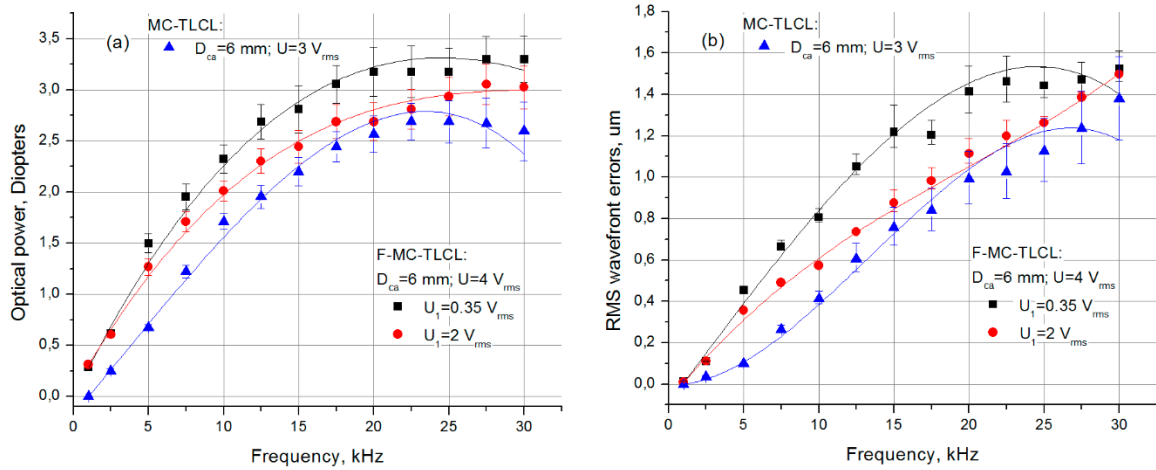


Figure 4.4. Optical characterization for the reference (classic MC-TLCL) and the proposed here (F-MC-TLCL) lenses. (a) OP vs frequency, (b) RMS wavefront errors vs frequency. Solid lines are third order polynomial approximations used for eye guiding only.

The RMS wavefront errors were calculated as follows [73]:

$$RMS \text{ wavefront error} = \sqrt{\frac{1}{N} \sum_{i=1}^N (\Delta W_i)^2 - \left(\frac{1}{N} \sum_{i=1}^N \Delta W_i \right)^2}, \quad (4.5)$$

where $\Delta W_i = W_i^{ideal}(r_i) - W_i^{measured}(r_i)$ is the difference between the ideal and measured wavefront surfaces at r_i , N is the number of steps along the r coordinate; $W_i = (\lambda/2\pi)\varphi$.

A conventional MC-TLCL of the same diameter was fabricated as a reference and measured using the same technique. Optimal control voltage and frequency for this reference lens (maximal OP and minimal RMS aberrations) were chosen from Shack-Hartmann measurements.

We have calculated standard errors for φ_0 and OP (see error bars in Fig. 4.4 (a)) as square roots of diagonal elements of variance-covariance matrix [98] that was constructed during fitting procedure. Based on the values of these standard errors, we have estimated errors for corresponding RMS aberrations (Fig. 4.4 (b)).

Usually, we recommend working slightly below the maximal achievable OP values (to have better RMS aberrations, speed and scatter levels). Thus, we can see that with this inquiry, we obtain approximately 23% higher OP values with the F-MC-TLCL, while its aberrations are slightly higher compared to the conventional MC-TLCL. In what follows, we shall try to evaluate the corresponding advantages and drawbacks by exploring the imaging quality obtained with these two TLCLs.

4.5.2 Tests with Fresnel MC-TLCL and raspberry pi camera

We realize that the use of only one additional zone cannot increase dramatically the OP of the lens. However, the simplicity of the proposed solution (both during its manufacturing as well as its dynamic control) can still provide better performance in some circumstances.

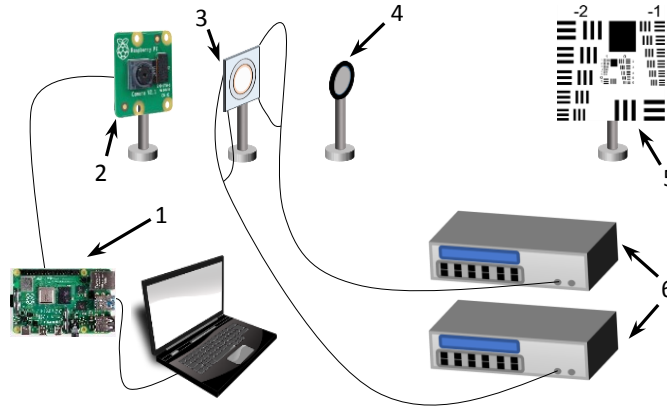


Figure 4.5. Schematics of the experimental setup used for comparison of image quality between MC-TLCL and F-MC-TLCL: (1) raspberry pi v4 [100], (2) raspberry pi camera v2 [101], (3) F-MC-TLCL or MC-TLCL, (4) polarizer, (5) USAF resolution chart, (6) function generators.

To confirm that better imaging (thanks to higher OP values) can be reached with the proposed here F-MC-TLCL, we have built a simple experimental setup (Fig. 4.5) consisting of a raspberry pi camera

(focused to infinity), TLCL, polarizer (since only one LC layer is used for demonstration, see e.g., [37]) and a USAF resolution chart [99]. The target was placed at 0.33 m from the camera with TLCL attached to it.

First, a picture with unpowered conventional MC-TLCL was recorded (Fig. 4.6 (a)). Then, knowing the dependence of OP upon driving frequency, we have applied an excitation signal of $U=3 \text{ V}_{\text{rms}}$; $f=22.5 \text{ kHz}$ that corresponds to the maximal achievable OP ($\approx 2.7 \text{ D}$) of such a lens (Fig. 4.6 (b)). Finally, the reference MC-TLCL was replaced with the F-MC-TLCL and a picture of the same target was recorded (Fig. 4.6 (c)) with $U=4 \text{ V}_{\text{rms}}$; $U_I=0.35 \text{ V}_{\text{rms}}$, $f=22.5 \text{ kHz}$, corresponding to OP $\approx 3.2 \text{ D}$.

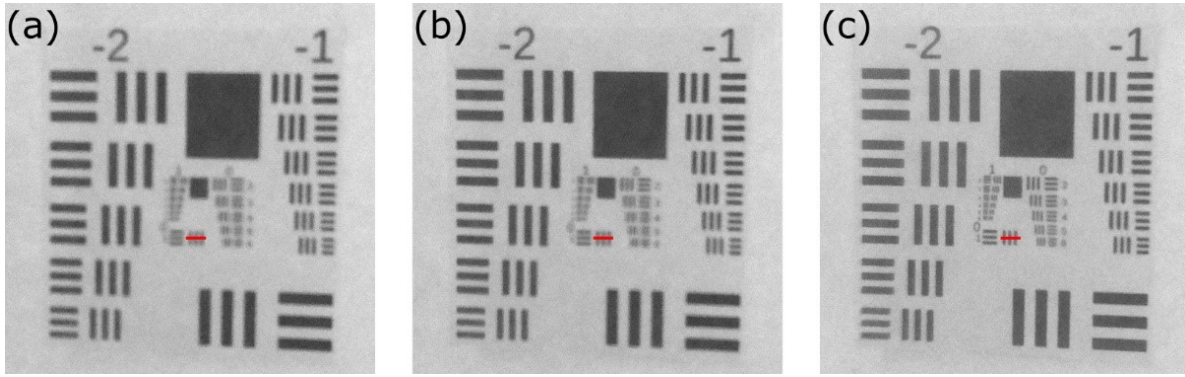


Figure 4.6. Pictures of the USAF resolution chart recorded by using the raspberry pi camera with (a) conventional MC-TLCL (unpowered); (b) MC-TLCL with $U=3 \text{ V}_{\text{rms}}$, $f=22.5 \text{ kHz}$; (c) F-MC-TLCL with $U=4 \text{ V}_{\text{rms}}$, $U_I=0.35 \text{ V}_{\text{rms}}$, $f=22.5 \text{ kHz}$. The small horizontal red line (in the centers of pictures) is used for intensity scan and analyses (see Fig. 4.7).

A noticeable improvement of the image quality can be seen in Fig. 4.6 (c) in comparison with Fig. 4.6 (b), since only the F-MC-TLCL was capable of reaching the OP necessary to have the image in focus, despite the fact that the RMS aberrations of the F-MC-TLCL are rather high. To quantify this difference, we have built contrast plots for all three cases mentioned above (Fig. 4.7). Gray values were taken for the same group of bars on the chart along the small red dashed line shown in Fig. 4.6. As we can see, the contrast obtained with the F-MC-TLCL (173/106) is significantly higher compared to other two cases (approximately 144/123).

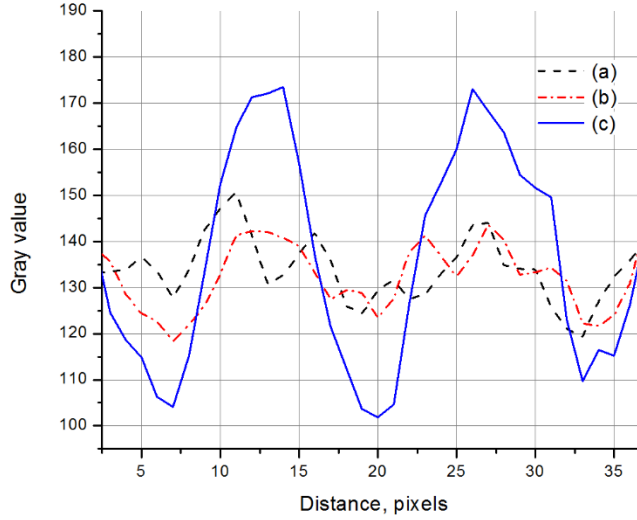


Figure 4.7. Contrast plots (a) conventional MC-TLCL (unpowered); (b) MC-TLCL with $U=3 V_{\text{rms}}$, $f=22.5 \text{ kHz}$; (c) F-MC-TLCL with $U=4 V_{\text{rms}}$, $U_I=0.35 V_{\text{rms}}$, $f=22.5 \text{ kHz}$.

For further characterization of the proposed F-MC-TLCL, the USAF chart was replaced by the Koren lens test chart [102] shown in Fig. 4.8. The spatial frequency on the sensor continuously increased from 4 to 400 lp/mm (sensor size of raspberry pi camera is 3.68 x 2.76 mm; pixel size is 1.12 μm).

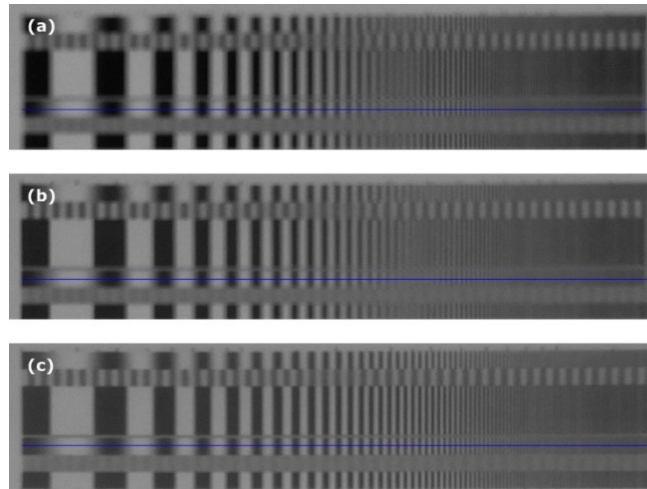


Figure 4.8. Picture of a target with increasing spatial frequency (in lp/mm) (a) without TLCL, when the raspberry pi camera is focused to infinity; (b) using MC-TLCL with $U=3 V_{\text{rms}}$, $f=22.5 \text{ kHz}$; (c) using F-MC-TLCL with $U=4 V_{\text{rms}}$, $U_I=0.35 V_{\text{rms}}$, $f=22.5 \text{ kHz}$. Blue horizontal lines are used for following intensity scans (see Fig. 4.9).

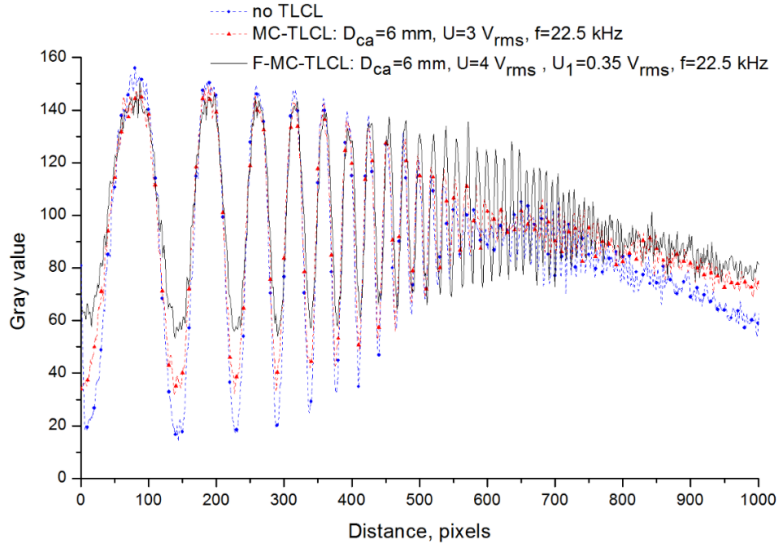


Figure 4.9. Contrast comparison for various spatial frequencies along the blue horizontal line (see Fig. 4.8) without TLCL, raspberry pi camera is focused to infinity (dashed blue line with circles); using conventional MC-TLCL (red dashed line with triangles) and F-MC-TLCL (black solid line).

The corresponding comparison of the obtained contrasts (along blue horizontal lines, shown in Fig. 4.8) are demonstrated in Fig. 4.9.

We can clearly see that two approaches have complementary performance: that is, the low spatial frequencies are better imaged with the help of a traditional MC-TLCL, while higher frequencies are better imaged by the F-MC-TLCL (high frequencies are better visible in Fig. 4.8 (c) rather than in Fig. 4.8 (b)). The situation may be different for a different initial focus setting, but, when needed, we can imagine a driving regime, where the inner electrodes can be actively driven (as in the present case) or left “floating” (in which case the F-MC-TLCL will perform as a standard MC-TLCL) depending upon the type of the image or the type of the details we are interested in. Double recording (in two different modes) and then image processing also might be possible. This once again indicates the interesting potential of our lens to be explored further.

Finally, we have made another performance comparison of F-MC-TLCL with the conventional MC-TLCL and the camera without variable focus capability by recording pictures of 3D objects, as shown in Fig. 4.10.

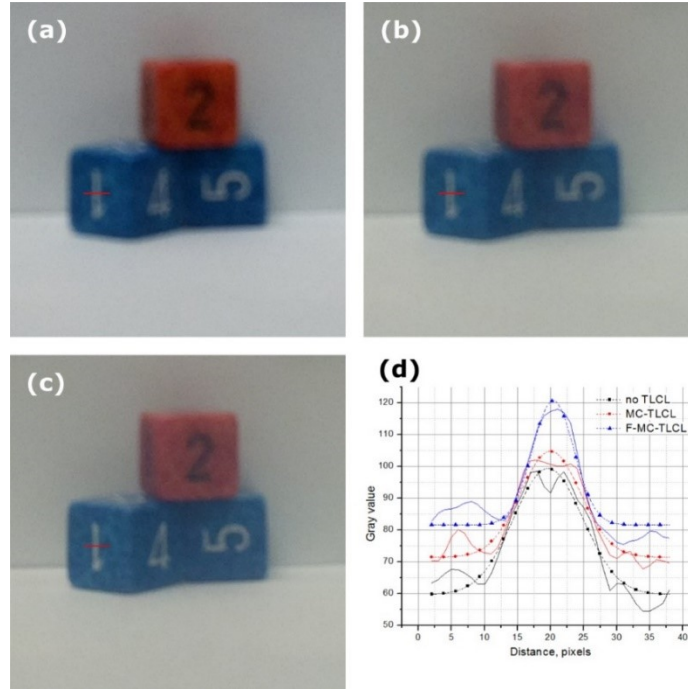


Figure 4.10. Pictures of objects taken with raspberry pi camera focused to infinity (a) without TLCL, (b) MC-TLCL with $U=3 V_{\text{rms}}$, $f=22.5 \text{ kHz}$; (c) F-MC-TLCL with $U=4 V_{\text{rms}}$, $U_I=0.35 V_{\text{rms}}$, $f=22.5 \text{ kHz}$; (d) – solid lines are gray values measured along red lines shown in (a)–(c), lines with symbols are corresponding Gaussian fits.

We have built the plots of gray values along red lines marked in Figs. 4.10 (a)-(c) for these three cases (Fig. 4.10 (d)). The distributions of gray values have been fitted with Gaussian functions. Obtained full widths at half maximums (FWHM) are the following: in the case of the camera only (without the TLCL) (a) $\text{FWHM} \approx 12 \text{ pixels}$; (b) $\text{FWHM} \approx 11 \text{ pixels}$ for conventional MC-TLCL; (c) $\text{FWHM} \approx 7 \text{ pixels}$ for F-MC-TLCL. This comparison shows that the sharpest image has been recorded by using the F-MC-TLCL. It is worth to mention that considering the width of number “1” (along which we measured the gray value), we see similar tendency for contrast levels as in Fig. 4.9 at low spatial frequencies (no TLCL – the lowest values for black, MC-TLCL – gray values for black are higher, F-MC-TLCL – the highest gray values for black due to scattering [88]). At the same time, we have observed that off axis image quality for F-MC-TLCL is slightly degraded in comparison with MC-TLCL, due to higher aberrations.

4.6 Theoretical model

4.6.1 Comparison with experiment

In this section we present the results of our numerical simulations for the F-MC-TLCL that are based on a previously discussed model of a classic MC-TLCL [37,42]. Here we took into account the additional concentric ring electrodes that were responsible for creating a phase jump.

We considered a 2-D axially symmetric geometry. Strong anchoring of the NLC molecules with substrates was assumed in our calculations. We also used one elastic constant approximation. In order to simplify simulations, we keep only the E_z electric field component in equations for the director (see Fig. 4.1), as this component dominates in the entire aperture, excluding a small zone just under the inner ring electrodes. The system of partial differential equations (PDEs), that needs to be solved to find director's configuration in the presence of external electric field, is shown below [1,9,37]:

$$\left\{ \begin{array}{l} \theta_{zz} + \frac{\epsilon_0 \epsilon_a}{2K} \sin(2\theta) E_z^2 = 0 \end{array} \right. \quad (4.6a)$$

$$\left\{ \begin{array}{l} \nabla \left(\left(\epsilon_0 \epsilon + i \frac{\sigma}{\omega} \right) \nabla V \right) = 0. \end{array} \right. \quad (4.6b)$$

Our simulation parameters can be found in Table 4.1:

Table 4.1. Simulation parameters.

Parameter	Value	Description
λ	550 nm	Wavelength
L	60 μ m	Cell thickness
R_o	3 mm	Clear aperture radius
R_l	1.95 mm	Radius of the innermost electrode
w	12 μ m	Width of inner electrodes with gap in between
θ_l	3°	Pretilt angle
K	8.58 pN	$K=(K_{11}+K_{33})/2$ Average elastic constant [55]
ϵ_{WCL}	20	Permittivity of the WCL
n_o	1.5398	Ordinary refractive index of 5CB LC [97]
n_e	1.7238	Extraordinary refractive index of 5 CB LC [97]

We have used a set-up and method, already discussed in [42], to measure the frequency dependences of real and imaginary values of relative permittivities of 5CB. Results of these

measurements were included in simulations and are shown in Fig. 4.11 (dots) along with their interpolations (solid lines):

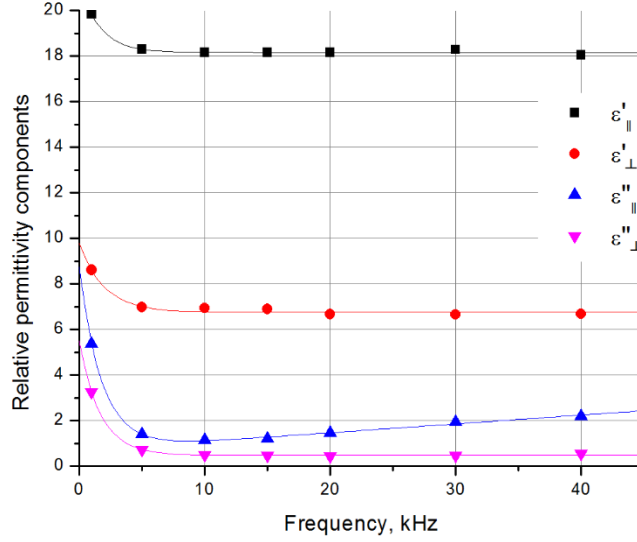


Figure 4.11. Experimental measurements of 5CB’s real and imaginary relative permittivity components at different applied signal’s frequencies.

Having obtained the distribution of director’s reorientation angle, we can calculate the phase retardation that a probe beam undergoes as it passes through the cell:

$$\varphi = \frac{2\pi}{\lambda} \int_0^L n_{eff}(r, z) dz, \quad (4.7)$$

where n_{eff} is the local extraordinary refractive index defined as [9]

$$n_{eff} = \frac{n_o n_e}{\sqrt{n_e^2 \sin^2 \theta + n_o^2 \cos^2 \theta}}. \quad (4.8)$$

To interpret the wavefront, we “lift” the inner portion of obtained phase retardation to the height of phase reset ignoring the portion of the “dead zone”. This part of the wavefront in between minimal and maximal points of phase retardation jump does not contribute to focusing effect. Then the curve is approximated with a parabolic function and values of OPs and RMS spherical aberrations (SA) are obtained (as defined by Eq. (4.4) and Eq. (4.5)).

Since the sheet resistance R_s of the WCL could not be measured precisely, we used it as a fitting parameter. Rough estimations (transmission line method [103,104]) of R_s for our F-MC-TLCLs showed that its value should be around 20 MOhm/sq.

Our preliminary simulations also have shown that, if the voltage applied to the middle electrode (U_I), is $0.35 V_{rms}$ then the heights of theoretically obtained phase resets are much higher than those experimentally measured. This makes us assume that the voltage on the middle electrode was higher than the presumed $0.35 V_{rms}$. We consider this to be a rather accurate assumption as the distance between innermost and middle electrodes is very small ($4 \mu m$), allowing the presence of a leaking electric current between them. Considering this, we have introduced an effective voltage U_{Ieff} that, along with R_s , was chosen to be a fitting parameter. We have used Nelder-Mead method [75] to minimize the RMS deviation between experimental and simulated wavefronts to find the optimal values of R_s and U_{Ieff} . The fitting algorithm was applied simultaneously only at three frequencies ($f=10, 20, 30$ kHz) for the purpose of facilitating calculations. Simulation results were evaluated and compared with experimental wavefronts obtained at $U=4 V_{rms}$, $U_I=0.35 V_{rms}$ and the same set of frequencies.

Found optimal parameters are the following: $R_s=30.03$ MOhm/sq (which is close to the value that we have initially considered) and $U_{Ieff}=1.61 V_{rms}$, which agrees with our assumption as well. Figures 4.12 (a) and (b) compare dependences of OPs and RMS aberrations upon the frequencies of applied signals obtained from experimental data and data simulated with fitting parameters:

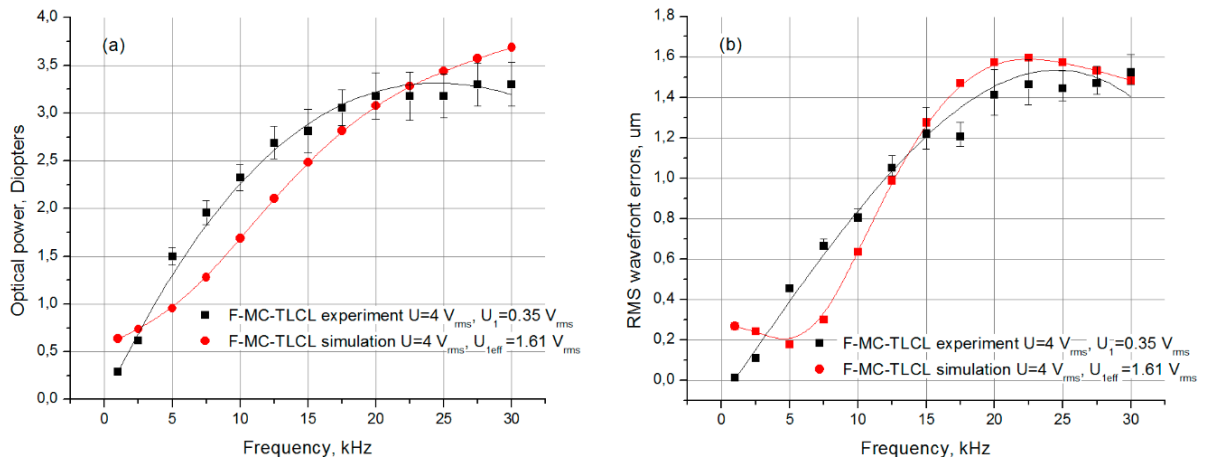


Figure 4.12. Comparison of (a) OPs and (b) RMS aberrations (total RMS wavefront errors in case of experiment and RMS SAs in case of theory) between experimentally acquired data and results obtained through simulations with fitting parameters.

From our experience of working with this type of lenses we know that the main contribution into deterioration of image quality comes from spherical aberrations. Even though only RMS SAs (axially symmetric model) are considered in simulations and total RMS wavefront errors coming

from several aberrations are estimated in experiment, it is still interesting to compare them. The differences between curves in Fig. 4.12 can be explained by model simplifications and made assumptions. We can also see a reasonable qualitative agreement for the model with fitting parameters.

4.6.2 Control optimization

We decided to further explore the performance limits of the F-MC-TLCL by using our theoretical model. Applying simplex optimization method [42,75], we searched for the best combinations of driving parameters U , U_{1eff} and f . The dependence of RMS SAs on achievable OPs (Fig. 4.13) demonstrates that aberrations can be greatly reduced (by a factor of about 2.5, comparing maximal values of simulated SAs with and without optimization) as a result of control improvement.

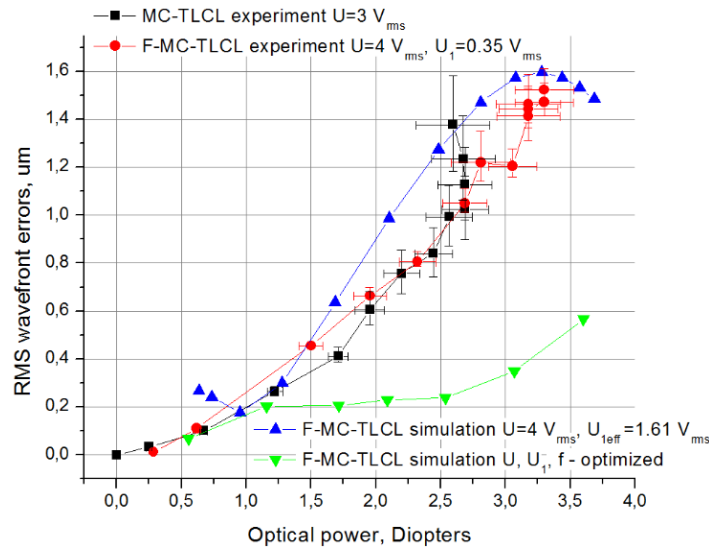


Figure 4.13. RMS wavefront errors vs OPs. Experimental results for MC-TLCL ($U=3 \text{ V}_{\text{rms}}$) – black line with squares, experimental result for F-MC-TLCL ($U=4 \text{ V}_{\text{rms}}$, $U_1=0.35 \text{ V}_{\text{rms}}$) – red line with circles, simulation of F-MC-TLCL ($U=4 \text{ V}_{\text{rms}}$, $U_{1eff}=1.61 \text{ V}_{\text{rms}}$) – blue line with up triangles, simulation of F-MC-TLCL (optimized driving) – green line with down triangles.

Moreover, optimized driving is also power efficient (see Table 4.2), as maximal frequencies are more than two times lower than those applied experimentally.

Table 4.2. Optimized control parameters and corresponding calculated OPs.

U, V_{rms}	U_I, V_{rms}	f, kHz	OPs, D
3.31	1.96	3.02	0.55
3.08	1.44	4.34	1.15
2.15	1.2	4.54	1.71
1.55	0.87	4.14	2.08
1.50	0.65	6.7	2.53
1.72	0.49	8.6	3.07
1.95	0.29	12.58	3.60

However, as we could see from the example of our prototype, for the moment, it is challenging to maintain a low value of voltage on only one inner electrode (due to the leaking current), for example $U_I = 0.3 V_{\text{rms}}$, in proximity (about $4 \mu\text{m}$ apart) to another electrode with significantly higher voltage applied to it, for example $U = 2 V_{\text{rms}}$.

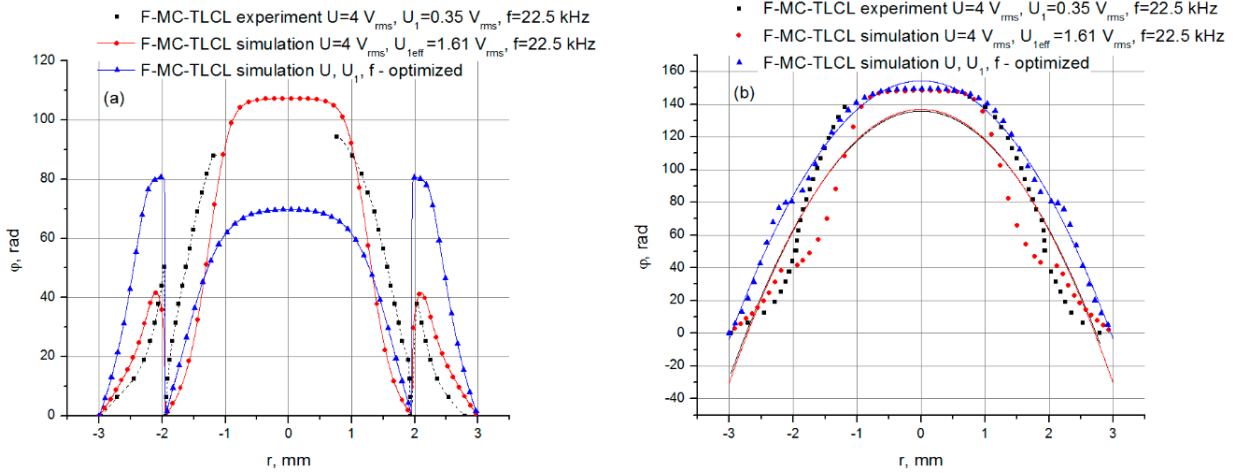


Figure 4.14. Wavefront comparisons (a) and processed wavefronts (b) with parabolic approximations (solid lines): experimentally obtained wavefront for F-MC-TLCL ($U=4 V_{\text{rms}}, U_I=0.35 V_{\text{rms}}, f=22.5 \text{ kHz}$) – black line with squares; simulated F-MC-TLCL ($U=4 V_{\text{rms}}, U_{I\text{eff}}=1.61 V_{\text{rms}}, f=22.5 \text{ kHz}$) – red line with circles; simulated F-MC-TLCL (optimized driving) – blue line with triangles.

Figures 4.14 (a) and (b) demonstrate why control optimization leads to a decrease of aberrations. There is a flat zone in the central part of the wavefront for both experimental F-MC-TLCL (black line with squares) and corresponding simulated wavefront (red line with circles).

However, the optimized wavefront (blue line with triangles) has a shape closer to the quadratic function in that area. Figure 4.14 (b) clearly shows that for the lens with optimized driving configuration we can obtain more gradual decrease of phase in the peripheral zone (from 2 mm to 3 mm). This also contributes into better image quality. In Fig. 4.14 (b) we cut-out the portion of wavefront from the “dead zone”, because light coming from this zone of the aperture is not focused.

4.7 Summary and conclusions

A prototype of wide aperture refractive Fresnel lens was created and analyzed. The interferometric characterization has shown that the lens can operate at higher OPs than the one of conventional design and the same aperture size. A series of optical tests was conducted. Analyses of images recorded by using an ordinary MC-TLCL and the proposed F-MC-TLCL confirmed that newly introduced lens exceeds the maximal OP of MC-TLCL. In this first demonstration of our prototype, the obtained RMS aberrations of the F-MC-TLCL are rather high, however there are known techniques (for example additional floating electrode and control optimization, discussed in detail in our previous works [37,42]), that will allow reducing them further. Also, our numerical modeling showed that an optimal driving regime can significantly improve image quality (once we reduce the leaking current). The suggested design requires relatively simple experimental procedure with only one photolithography step. The design also enables us to switch between Fresnel TLCL and ordinary TLCL by leaving inner electrodes floating when needed.

4.8 Acknowledgments

We would like to thank Professor Nasser Peyghambarian for the information about the diffractive Fresnel lenses. We also thank the R&D group of LensVector Inc. for the use of their equipment. We acknowledge the financial support of the Natural Sciences and Engineering Research Council of Canada (NSERC 05888 and NSERC 507007). We also thank Canada Research Chair in Liquid Crystals and Behavioral Biophotonics (CRC 230212) and Manning Innovation and INO-CAP foundations for their support. We also thank the Sentinel North of NSERC/Laval University for the Ph.D. scholarship O.S.

Summary and conclusions

Our research had a goal of exploring new tunable liquid crystal lens designs using experimental and theoretical techniques. We were searching for original approaches permitting to overcome some well-known weaknesses of commercially available liquid crystal lenses: aberrations, narrow tunability range, production complexity, high power consumption, etc. The results of this work are arranged in chapters 1-4. Throughout the thesis two different mechanisms of electric field shaping have been considered. Systems presented in chapters 1 and 2 are based on optically hidden dielectric layer principle and lenses in chapters 3 and 4 use modal control design.

The article that forms chapter 1 is a theoretical study of hidden layer liquid crystal tunable lens. Simulation results showed that the increase of liquid crystal cell's gap leads to a wider dynamic range of optical powers. But scattering and excitation time increase as well. Thus, a compromise should be found between reorientation speed and tunability range. Explored temperature dependence of optical power using 5 CB and E49 liquid crystals demonstrated the decrease of maximal achievable optical power with the rise of temperature. The obtained dependences allow to predict the behavior of the lens and compensate optical power variations using microheaters. The exploration of relative permittivities of two dielectric materials forming the hidden layer demonstrated that after reaching a certain ratio ($\epsilon_{IML}/\epsilon_{CL}$) optical power remains constant. At the same time, we can conclude that the lens of this type can be realized even when the relative permittivities of materials composing hidden layer are equal, but significant difference between their conductivities exists. We have shown that an optimal value of the height of the core lens could be found, providing maximal optical power.

Chapter 2 is the inserted article which investigates the possibility of creating arrays of microlenses and microprisms using hidden layer principle. In this part of the thesis we evaluated the dependences of optical modulation efficiencies on the spatial frequency of considered dielectric structures. Deviation of wavefronts from desired ideal shapes was also quantified. The dependence of optical power of microlenses on spatial frequency is non-monotonic. This enables us to choose an optimal aperture size of microlenses to obtain the highest optical power. In the case of microprism structures, the effect of light steering quickly disappears with the increase of their spatial frequency and the device starts to act similar to microlenses. This degradation is caused by fringing electric fields from neighboring microprisms.

The main disadvantage of hidden layer lens design is the requirement of relatively high voltages due to the presence of dielectric layers, although power consumption is still comparable with

other designs. On the other hand, this approach has several advantages such as zero optical power in unpowered state, flat liquid crystal gap, no light reflection on material interfaces. Moreover, the concept allows to obtain tunable wavefronts of predefined shapes.

In chapter 3 we have presented the results of modal control lens study. We have built a custom set-up to measure frequency dependences of liquid crystal dielectric permittivities. A theoretical model of the traditional modal control lens was constructed. A good agreement with experimental data was achieved. This model was used to explore several modifications of the standard modal control lens. Results of simulations have demonstrated that the presence of an additional powered ring electrode at the periphery of the aperture helps to correct the wavefront in this area. Another modification utilizing a floating disk electrode causes redistribution of electric potential, extending the range of tunable optical power and keeping low RMS SAs. Furthermore, a combination of two design modifications and optimal powering provides the possibility of switching between two regimes of operation. Thus, the dynamic range of optical power can reach up to 3.5 D (with RMS SAs $<0.1 \mu\text{m}$) making this lens suitable for the use in ophthalmology.

In chapter 4 we introduced a new design of a refractive tunable liquid crystal Fresnel lens. It requires only one photolithography step, which greatly simplifies the experimental procedure. Unlike existing switchable liquid crystal Fresnel lenses, our design provides continuous optical power variation. Conducted experimental tests showed the increase of optical power in comparison with a reference lens. A theoretical model of this design was created and discussed. Although the prototype lens has rather high aberrations, the same techniques of image quality improvement that were described in chapter 3 can be implemented in this case. Optimization of control voltages and frequencies, performed with our numerical model, predicts noticeable decrease of aberrations and power consumption. This is a promising approach of creating fast wide aperture tunable liquid crystal lens without reduction of maximal optical power.

To summarize, every tunable liquid crystal lens design studied in our work aimed at specific application. Built theoretical models were used to perform engineering optimizations to improve initial lens configurations. All our lenses require relatively simple experimental assembly, therefore lowering the cost of each unit. Only flat cell gaps were used, avoiding possible defect formations. Achievable ranges of optical power are sufficient for desired tasks (autofocus, zoom, vision correction). We have tested several methods that improve image quality and could be used in future designs of liquid crystal lenses. The overall performance of our devices makes them competitive with existing tunable optics solutions.

Appendix A Nelder-Mead method

The Nelder-Mead method is a popular and computationally effective simplex numerical algorithm proposed by John Nelder and Roger Mead, which finds a local minimum or maximum of a function of several variables [105].

Let us assume that we want to find a minimum value of a function that depends on 2 variables. In this case, the method will construct a triangle (3 vertices) in parametric space and compare function values at the vertices. For a higher number of function variables (N) this approach will build a simplex (a generalized triangle) with N+1 vertices in N dimensional space. The worst vertex, where function takes maximal value, is replaced with a new vertex. The algorithm creates a sequence of simplexes (triangles for the case of two independent variables), where the size of each new simplex is reduced until a predefined stopping criteria is fulfilled and a point in parametric space which corresponds to the minimum of the function is found. This direct search method is often used for nonlinear optimization problems, for which function derivatives are not known [106].

Table A.1 gives a description of method's logical decisions [75] using a two-dimensional problem as an example. The following definitions are introduced to explain the algorithm:

B = (x_1, y_1) – coordinates of the best vertex (function value is minimal for this set of parameters)

G = (x_2, y_2) – coordinates of a good vertex (next to the best vertex)

W = (x_3, y_3) – the worst of three vertices

For these points we have an inequality:

$$f(\mathbf{B}) < f(\mathbf{G}) < f(\mathbf{W}), \quad (\text{A.1})$$

where $f(\mathbf{X})$ is evaluated function, \mathbf{X} is a point in parametric space.

$$\mathbf{M} = (\mathbf{B} + \mathbf{G} + \mathbf{W})/3 \text{ – midpoint,} \quad (\text{A.2})$$

$$\mathbf{R} = 2 \cdot \mathbf{M} - \mathbf{W} \text{ – reflection point,} \quad (\text{A.3})$$

$$\mathbf{E} = 2 \cdot \mathbf{R} - \mathbf{M} \text{ – extension point,} \quad (\text{A.4})$$

$$\mathbf{C} = (\mathbf{W} + \mathbf{M})/2 \text{ – contraction point.} \quad (\text{A.5})$$

In this thesis a modification of Matlab's "fminsearch" algorithm (based on Nelder-Mead method) with application of constraints on optimized variables was implemented. Other modifications that allow to find a global minimum of a function within limited search area also exist. We used this method for the search of fitting parameters to achieve the best agreement of data obtained through simulations with experimental results, when precise measurements of required experimental parameters were not possible (see section 4.2 of chapter 3 and section 6.1 of chapter 4). The method was also successfully applied to find optimal geometry and control parameters of tunable liquid crystal lenses (see chapters 3 and 4).

Table A.1. Pseudocode for the Nelder-Mead algorithm.

IF $f(R) < f(G)$, THEN Perform Case (i) {either reflect or extend} ELSE Perform Case (ii) {either contract or shrink}	
BEGIN {Case (i)} IF $f(B) < f(R)$ THEN replace W with R ELSE Compute E and $f(E)$ IF $f(E) < f(B)$ THEN replace W with E ELSE replace W with R ENDIF ENDIF END {Case (i)}	BEGIN {Case (ii)} IF $f(R) < f(W)$ THEN replace W with R Compute $C = (W+M)/2$ IF $f(C) < f(W)$ THEN replace W with C ELSE replace W with $(B+W)/2$ replace G with $(B+G)/2$ ENDIF END {Case (ii)}

Appendix B PSF and MTF calculation

In this section we would like to present some supplementary simulation results regarding modal control tunable lens and its modifications described in chapter 3. These results were not included in the article, but they still present scientific interest, confirming the improvement of image quality following our design suggestions.

We decided to calculate PSF and MTF dependences of a 4 mm traditional modal control lens and compare them with similar calculations for modal control lens bearing a floating disk and a powered ring electrodes.

Simulation parameters for ordinary modal control lens are listed in Table 3.1 with the only difference of diameter of the lens being 4 mm for this calculation. Applied frequency was chosen to be 9.8 kHz which corresponds to approximately +3 D (RMS SAs $\approx 0.27 \mu\text{m}$; see Fig. 3.7). In the case of modal control lens with modifications, we used optimized additional electrodes' dimensions and control voltages, which can be found in the last row of Table 3.2. Applied frequency of 7.3 kHz corresponded to approximately +3 D of optical power (RMS SAs $\approx 0.06 \mu\text{m}$). Therefore, optical powers of compared lenses were identical.

To calculate PSF and MTF we use scalar diffraction theory, assuming that light propagates in linear, isotropic, homogenous, nondispersive and nonmagnetic medium. Knowing phase distribution of light at the exit from LC cell we can calculate the intensity of light at the focal point:

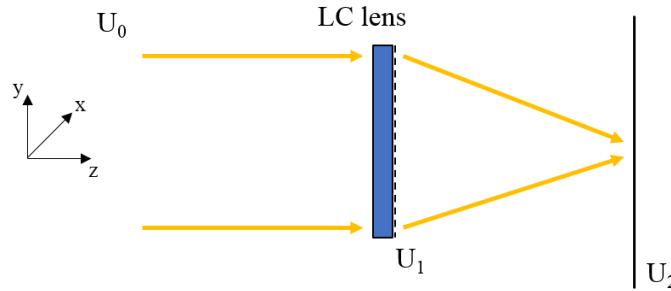


Figure B.1. Schematics of light propagation through LC lens.

The incident light is a monochromatic plane wave propagating in z direction (U_0). We need to consider only the light that passes through the aperture of liquid crystal lens, hence pupil function $A_1(x, y)$ is introduced. Considering that light at the exit of the cell acquires phase distribution φ_1 , we can write down the amplitude of light right after the liquid crystal cell as

$$U_1(x, y) = A_1(x, y) \exp(i\varphi_1(x, y)). \quad (\text{B.1})$$

To find the amplitude of light at the focal plane we perform a Fourier transform and an inverse Fourier transform:

$$U_2(x, y) = \mathfrak{F}^{-1}\{\mathfrak{F}\{U_1\}H\}, \quad (\text{B.2})$$

where $H(f_x, f_y)$ is Rayleigh–Sommerfeld transfer function, f_x, f_y – spatial frequencies.

$$H(f_x, f_y) = \exp\left(jkz\sqrt{1 - (\lambda f_x)^2 - (\lambda f_y)^2}\right). \quad (\text{B.3})$$

Then irradiance distribution at the focal plane can be found by multiplying U_2 by its complex conjugate

$$I_2 = U_2 U_2^*. \quad (\text{B.4})$$

Detailed procedure of MTF and PSF calculation including Matlab scripts can be found in [107].

The distribution of irradiances in two considered cases is presented below:

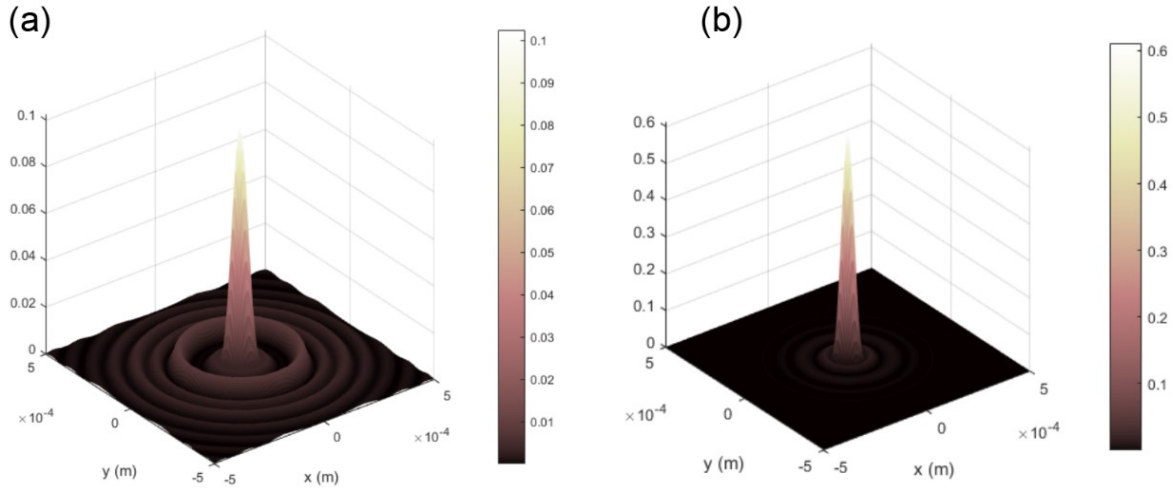


Figure B.2. Point spread function of simulated modal control lenses with 4 mm clear aperture: (a) – traditional approach, (b) – modified lens with improved aberrations.

Performing one more Fourier transform we obtained MTFs of tunable liquid crystal lenses:

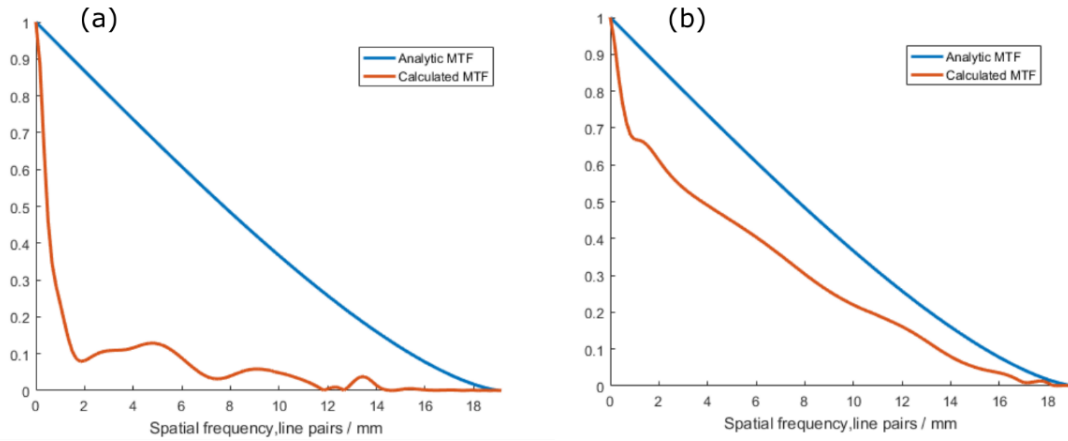


Figure B.3. Modulation transfer function of simulated modal control lenses with 4 mm clear aperture: (a) – traditional approach, (b) – modified lens with improved aberrations.

Figures B.2 and B.3 confirm one more time the advantages of proposed modifications to conventional modal control lens. The lens with additional electrodes demonstrates PSF and MTF dependences that are much closer to the case of non-aberrated ideal lens.

We have also applied the method described above to simulate propagation of light through microprisms (see section 5.2 of chapter 2). For comparison purposes, we have performed similar calculations for ideal microprisms that do not have the “dead zones” (see blue solid lines in Fig. B.4). The maximal phase retardation values for ideal profiles were chosen to be equal to the ones of simulated profiles.

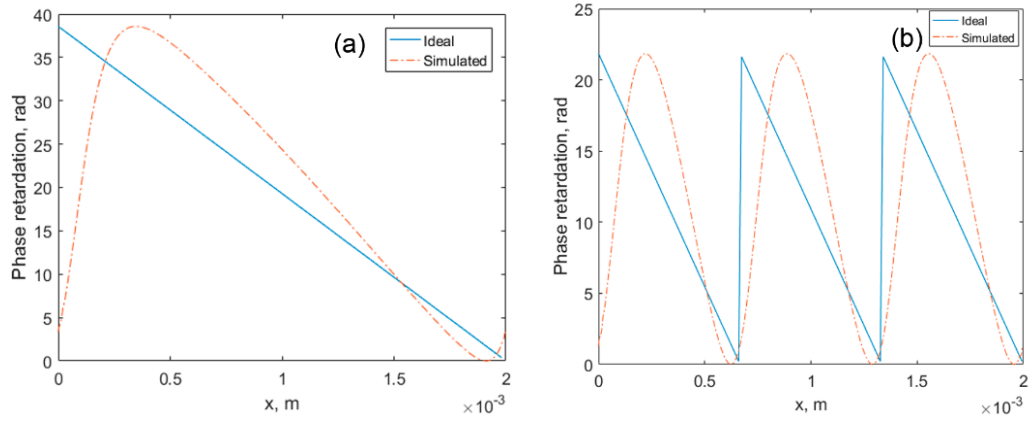


Figure B.4. Simulated phase profiles of microprisms (orange dashed lines) and corresponding ideal profiles (blue solid lines) in the case of (a) 1 prism over $2000 \mu\text{m}$ and (b) 3 prisms over $2000 \mu\text{m}$.

Obtained beam propagation results are presented in Figures B.5 (a) and (b) and Figures B.6 (a) and (b).

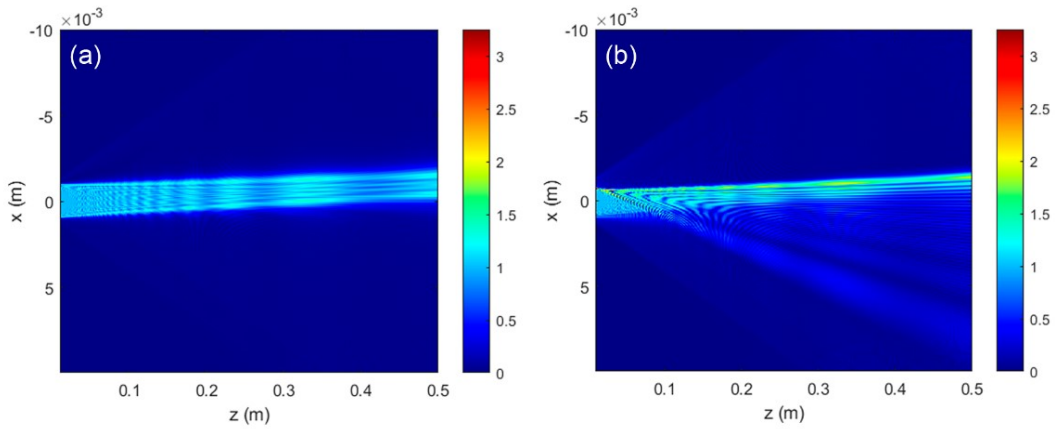


Figure B.5. Light intensity distribution (arbitrary units) along direction of beam propagation (z axis), simulated using (a) ideal prism phase retardation profile, (b) phase retardation profile of a microprism with the “dead zone”. Spatial frequency of the hidden dielectric structure is 1 microprism over $2000 \mu\text{m}$ (see Fig. B.4 (a)).

We can clearly see that the portion of aperture belonging to the “dead zone” contributes to tilting the beam in an undesired direction.

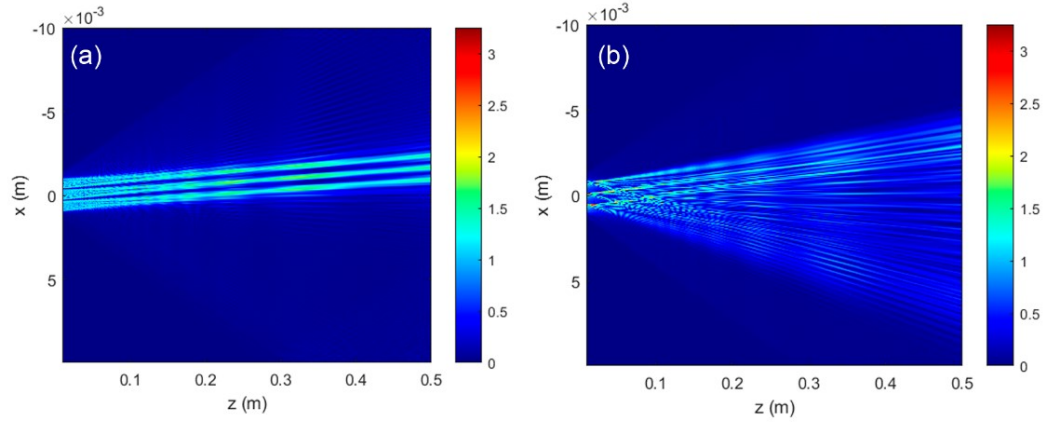


Figure B.6. Light intensity distribution (arbitrary units) along direction of beam propagation (z axis), simulated using (a) ideal prisms' phase retardation profile, (b) phase retardation profile of microprisms with the “dead zone”. Spatial frequency of the hidden dielectric structure is 3 microprisms over $2000 \mu\text{m}$ (see Fig. B.4 (b)).

The effect is more pronounced in the case of three microprisms as relative size of the “dead zone” is larger (approximately 40 % of the aperture) than in the previous case.

Bibliography

- [1] P.G. de Gennes, J. Prost, *The Physics of Liquid Crystals*, 2nd ed., Clarendon Press, 1993.
- [2] S. Chandrasekhar, *Liquid Crystals*, 2nd ed., Cambridge University Press, 1992.
- [3] A. Sonin, *Introduction to the Physics of Liquid Crystals*, Nauka, Moscow, 1983.
- [4] S.-T. Wu, D.-K. Yang, *Fundamentals of Liquid Crystal Devices*, 2nd ed., John Wiley & Sons, Inc., 2015.
- [5] Z. He, F. Gou, R. Chen, K. Yin, T. Zhan, S.-T. Wu, *Liquid Crystal Beam Steering Devices: Principles, Recent Advances, and Future Developments*, *Crystals*. 9 (2019). <https://doi.org/10.3390/cryst9060292>.
- [6] T. V. Galstian, *Smart Mini-Cameras*, CRC Press, 2013. <https://doi.org/10.1201/b15555>.
- [7] Y. Li, D. Luo, Z.H. Peng, Full-color reflective display based on narrow bandwidth templated cholesteric liquid crystal film, *Opt. Mater. Express*. 7 (2017) 16–24. <https://doi.org/10.1364/OME.7.000016>.
- [8] S.-W. Oh, J.-M. Baek, J. Heo, T.-H. Yoon, Dye-doped cholesteric liquid crystal light shutter with a polymer-dispersed liquid crystal film, *Dye. Pigment*. 134 (2016) 36–40. <https://doi.org/10.1016/j.dyepig.2016.06.045>.
- [9] L.M. Blinov, V.G. Chigrinov, *Electrooptic Effects in Liquid Crystal Materials*, Springer New York, New York, NY, 1994. <https://doi.org/10.1007/978-1-4612-2692-5>.
- [10] D. Andrienko, Introduction to liquid crystals, *J. Mol. Liq.* 267 (2018) 520–541. <https://doi.org/10.1016/j.molliq.2018.01.175>.
- [11] I. W. Stewart, Continuum Theory for Liquid Crystals, in: *Handb. Liq. Cryst.*, Wiley-VCH Verlag GmbH & Co. KGaA, Weinheim, Germany, 2014: pp. 1–36. <https://doi.org/10.1002/9783527671403.hlc005>.
- [12] P. Sheng, Introduction to the Elastic Continuum Theory of Liquid Crystals, in: *Introd. to Liq. Cryst.*, Springer US, Boston, MA, 1975: pp. 103–127. https://doi.org/10.1007/978-1-4684-2175-0_8.
- [13] C.W. Oseen, The theory of liquid crystals, *Trans. Faraday Soc.* 29 (1933) 883–899. <https://doi.org/10.1039/tf9332900883>.
- [14] F.C. Frank, I. Liquid crystals. On the theory of liquid crystals, *Discuss. Faraday Soc.* 25 (1958) 19–28. <https://doi.org/10.1039/df9582500019>.
- [15] H. Ren, S. Wu, *Introduction to Adaptive Lenses*, John Wiley & Sons, 2012. <https://doi.org/10.1002/9781118270080>.
- [16] L.M. Blinov, *Structure and Properties of Liquid Crystals*, Springer Netherlands, Dordrecht, 2011. <https://doi.org/10.1007/978-90-481-8829-1>.
- [17] M. Born, E. Wolf, *Principles of Optics: Electromagnetic Theory of Propagation, Interference and Diffraction of Light*, 7th ed., Cambridge University Press, Cambridge, 1999.
- [18] S.T. Wu, Phase retardation dependent optical response time of parallel-aligned liquid crystals, *J. Appl. Phys.* 60 (1986) 1836–1838. <https://doi.org/10.1063/1.337228>.
- [19] I. Gelfand, S. Fomin, *Calculus of Variations*, Prentice Hall Inc., 1963.
- [20] A. Rapini, M. Papoular, Distorsion d'une lamelle nématique sous champ magnétique:

- conditions d'ancrage aux parois, *Le J. Phys. Colloq.* 30 (1969) 54–56. <https://doi.org/10.1051/jphyscol:1969413>.
- [21] J.G. Sivak, Through the lens clearly: phylogeny and development, *Investig. Ophthalmology Vis. Sci.* 45 (2004) 740–747. <https://doi.org/10.1167/iovs.03-0466>.
- [22] S. Sato, Liquid-crystal lens-cells with variable focal length, *Jpn. J. Appl. Phys.* 18 (1979) 1679–1684. <https://doi.org/10.1143/JJAP.18.1679>.
- [23] Y.-H. Lin, Y.-J. Wang, V. Reshetnyak, Liquid crystal lenses with tunable focal length, *Liq. Cryst. Rev.* 5 (2017) 111–143. <https://doi.org/10.1080/21680396.2018.1440256>.
- [24] M. Ye, S. Sato, Optical properties of liquid crystal lens of any size, *Jpn. J. Appl. Phys.* 41 (2002) L571–L573. <https://doi.org/10.1143/JJAP.41.L571>.
- [25] H.-C. Lin, M.-S. Chen, Y.-H. Lin, A review of electrically tunable focusing liquid crystal lenses, *Trans. Electr. Electron. Mater.* 12 (2011) 234–240. <https://doi.org/10.4313/TEEM.2011.12.6.234>.
- [26] B. Wang, M. Ye, M. Honma, T. Nose, S. Sato, Liquid crystal lens with spherical electrode, *Jpn. J. Appl. Phys.* 41 (2002) L1232–L1233. <https://doi.org/10.1143/JJAP.41.L1232>.
- [27] A. Jamali, D. Bryant, Y. Zhang, A. Grunnet-Jepsen, A. Bhowmik, P.J. Bos, Design of a large aperture tunable refractive Fresnel liquid crystal lens, *Appl. Opt.* 57 (2018) B10–B19. <https://doi.org/10.1364/AO.57.000B10>.
- [28] O. Sova, V. Reshetnyak, T. Galstian, K. Asatryan, Electrically variable liquid crystal lens based on the dielectric dividing principle, *J. Opt. Soc. Am. A.* 32 (2015) 803–808. <https://doi.org/10.1364/josaa.32.000803>.
- [29] B. Wang, M. Ye, S. Sato, Lens of electrically controllable focal length made by a glass lens and liquid-crystal layers, *Appl. Opt.* 43 (2004) 3420–3425. <https://doi.org/10.1364/AO.43.003420>.
- [30] K. Asatryan, V. Presnyakov, A. Tork, A. Zohrabyan, A. Bagramyan, T. Galstian, Optical lens with electrically variable focus using an optically hidden dielectric structure, *Opt. Express.* 18 (2010) 13981–13992. <https://doi.org/10.1364/OE.18.013981>.
- [31] A.F. Naumov, M.Y. Loktev, I.R. Guralnik, G. Vdovin, Liquid-crystal adaptive lenses with modal control, *Opt. Lett.* 23 (1998) 992–994. <https://doi.org/10.1364/OL.23.000992>.
- [32] A.F. Naumov, G.D. Love, M.Y. Loktev, F.L. Vladimirov, Control optimization of spherical modal liquid crystal lenses, *Opt. Express.* 4 (1999) 344–352. <https://doi.org/10.1364/OE.4.000344>.
- [33] I.R. Guralnik, M.Y. Loktev, A.F. Naumov, Electrophysics of adaptive LC lens with modal control, in: V.F. Tarasenko, G. V. Mayer, G.G. Petrush (Eds.), *Int. Conf. At. Mol. Pulsed Lasers III*, 2000: pp. 209–218. <https://doi.org/10.1117/12.383457>.
- [34] G. Vdovin, M. Loktev, A. Naumov, On the possibility of intraocular adaptive optics, *Opt. Express.* 11 (2003) 810–817. <https://doi.org/10.1364/oe.11.000810>.
- [35] G. V Vdovin, I.R. Guralnik, S.P. Kotova, M.Y. Loktev, A.F. Naumov, Liquid-crystal lenses with a controlled focal length. I. Theory, *Quantum Electron.* 29 (1999) 256–260. <https://doi.org/10.1070/QE1999v029n03ABEH001463>.
- [36] T. Galstian, K. Asatryan, V. Presniakov, A. Zohrabyan, A. Tork, A. Bagramyan, S. Careau, M. Thiboutot, M. Cotovanu, High optical quality electrically variable liquid crystal lens using an additional floating electrode, *Opt. Lett.* 41 (2016) 3265–3268.

<https://doi.org/10.1364/OL.41.003265>.

- [37] T. Galstian, O. Sova, K. Asatryan, V. Presniakov, A. Zohrabyan, M. Evensen, Optical camera with liquid crystal autofocus lens, *Opt. Express*. 25 (2017) 29945–29964. <https://doi.org/10.1364/oe.25.029945>.
- [38] S.-H. Lin, L.-S. Huang, C.-H. Lin, C.-T. Kuo, Polarization-independent and fast tunable microlens array based on blue phase liquid crystals, *Opt. Express*. 22 (2014) 925–930. <https://doi.org/10.1364/OE.22.000925>.
- [39] J.-P. Cui, H.-X. Fan, Q.-H. Wang, A polarisation-independent blue-phase liquid crystal microlens using an optically hidden dielectric structure, *Liq. Cryst.* 44 (2017) 643–647. <https://doi.org/10.1080/02678292.2016.1226973>.
- [40] O. Sova, V. Reshetnyak, T. Galstian, Modulation transfer function of liquid crystal microlenses and microprisms using double dielectric layer, *Appl. Opt.* 57 (2018) 18–24. <https://doi.org/10.1364/AO.57.000018>.
- [41] O. Sova, T. Galstian, Modal control refractive Fresnel lens with uniform liquid crystal layer, *Opt. Commun.* 474 (2020) 126056. <https://doi.org/10.1016/j.optcom.2020.126056>.
- [42] O. Sova, T. Galstian, Liquid crystal lens with optimized wavefront across the entire clear aperture, *Opt. Commun.* 433 (2019) 290–296. <https://doi.org/10.1016/j.optcom.2018.10.030>.
- [43] T. Galstian, K. Asatryan, V. Presniakov, “Method and apparatus for spatially modulated electric field generation and electro-optical tuning using liquid crystals,” patent WO2007/098602, September 7, 2007.
- [44] O. Sova, V. Reshetnyak, T. Galstian, Theoretical analyses of a liquid crystal adaptive lens with optically hidden dielectric double layer, *J. Opt. Soc. Am. A*. 34 (2017) 424–431. <https://doi.org/10.1364/JOSAA.34.000424>.
- [45] X. Shang, J.-Y. Tan, O. Willekens, J. De Smet, P. Joshi, D. Cuypers, E. Islamaj, J. Beeckman, K. Neyts, M. Vervaeke, H. Thienpont, H. De Smet, Electrically controllable liquid crystal component for efficient light steering, *IEEE Photonics J.* 7 (2015) 1–13. <https://doi.org/10.1109/JPHOT.2015.2402592>.
- [46] T. Galstian, P. Clark, P.T.C. Antognini, J. Parker, D.A. Proudian, T.E. Killick, A. Zohrabyan, “Autofocus system and method,” U.S. patent 8,629,932, January 14, 2014.
- [47] A. Bagramyan, T. Galstian, A. Saghatelian, Motion-free endoscopic system for brain imaging at variable focal depth using liquid crystal lenses, *J. Biophotonics*. 10 (2017) 762–774. <https://doi.org/10.1002/jbio.201500261>.
- [48] A. Bagramyan, T. Galstian, Dynamic control of polarization mismatch and coma aberrations in rod-GRIN assemblies, *Opt. Express*. 27 (2019) 14144–14151. <https://doi.org/10.1364/OE.27.014144>.
- [49] T. Galstian, K. Asatryan, V. Presniakov, A. Zohrabyan, Electrically variable liquid crystal lenses for ophthalmic distance accommodation, *Opt. Express*. 27 (2019) 18803–18817. <https://doi.org/10.1364/oe.27.018803>.
- [50] www.lensvector.com, (2020).
- [51] H. Ren, D.W. Fox, B. Wu, S.-T. Wu, Liquid crystal lens with large focal length tunability and low operating voltage, *Opt. Express*. 15 (2007) 11328–11335. <https://doi.org/10.1364/OE.15.011328>.
- [52] X. Nie, R. Lu, H. Xianyu, T.X. Wu, S.-T. Wu, Anchoring energy and cell gap effects on liquid

- crystal response time, *J. Appl. Phys.* 101 (2007) 103110. <https://doi.org/10.1063/1.2734870>.
- [53] G.W. Kaye, T.H. Laby, “Physical Properties of Sea Water”. Tables of physical and chemical constants (16th ed.), (2017). www.kayelaby.npl.co.uk.
- [54] R.M. Pashley, M. Rzechowicz, L.R. Pashley, M.J. Francis, De-gassed water is a better cleaning agent, *J. Phys. Chem. B.* 109 (2005) 1231–1238. <https://doi.org/10.1021/jp045975a>.
- [55] A. Bogi, S. Faetti, Elastic, dielectric and optical constants of 4'-pentyl-4-cyanobiphenyl, *Liq. Cryst.* 28 (2001) 729–739. <https://doi.org/10.1080/02678290010021589>.
- [56] J. Li, S.T. Wu, Extended Cauchy equations for the refractive indices of liquid crystals, *J. Appl. Phys.* (2004). <https://doi.org/10.1063/1.1635971>.
- [57] S. Faetti, B. Cocciaro, Elastic, dielectric and optical constants of the nematic mixture E49, *Liq. Cryst.* (2009). <https://doi.org/10.1080/02678290902736903>.
- [58] Y.-H. Lin, H.-S. Chen, H.-C. Lin, Y.-S. Tsou, H.-K. Hsu, W.-Y. Li, Polarizer-free and fast response microlens arrays using polymer-stabilized blue phase liquid crystals, *Appl. Phys. Lett.* 96 (2010) 113505. <https://doi.org/10.1063/1.3360860>.
- [59] S. Sato, Applications of liquid crystals to variable-focusing lenses, *Opt. Rev.* 6 (1999) 471–485. <https://doi.org/10.1007/s10043-999-0471-z>.
- [60] L. Guoqiang, Adaptive Lens, in: *Prog. Opt.*, 2010: pp. 199–283. <https://doi.org/10.1016/B978-0-444-53705-8.00004-7>.
- [61] C.-W. Chen, M. Cho, Y.-P. Huang, B. Javidi, Three-dimensional imaging with axially distributed sensing using electronically controlled liquid crystal lens, *Opt. Lett.* 37 (2012) 4125–4127. <https://doi.org/10.1364/OL.37.004125>.
- [62] H.-S. Chen, Y.-H. Lin, An endoscopic system adopting a liquid crystal lens with an electrically tunable depth-of-field, *Opt. Express.* 21 (2013) 18079–18088. <https://doi.org/10.1364/OE.21.018079>.
- [63] J.L. Alió, J.L. Alió del Barrio, A. Vega-Estrada, Accommodative intraocular lenses: where are we and where we are going, *Eye Vis.* 4 (2017) 16. <https://doi.org/10.1186/s40662-017-0077-7>.
- [64] H.E. Milton, P.B. Morgan, J.H. Clamp, H.F. Gleeson, Electronic liquid crystal contact lenses for the correction of presbyopia, *Opt. Express.* 22 (2014) 8035–8040. <https://doi.org/10.1364/oe.22.008035>.
- [65] H.-S. Chen, Y.-J. Wang, P.-J. Chen, Y.-H. Lin, Electrically adjustable location of a projected image in augmented reality via a liquid-crystal lens, *Opt. Express.* 23 (2015) 28154–28162. <https://doi.org/10.1364/OE.23.028154>.
- [66] Y.-H. Lee, G. Tan, T. Zhan, Y. Weng, G. Liu, F. Gou, F. Peng, N. V. Tabiryan, S. Gauza, S.-T. Wu, Recent progress in Pancharatnam–Berry phase optical elements and the applications for virtual/augmented realities, *Opt. Data Process. Storage.* 3 (2017) 79–88. <https://doi.org/10.1515/odps-2017-0010>.
- [67] F. Kahn, “Electronically variable iris or stop mechanisms,” U.S. patent 3,741,629, June 26, 1973.
- [68] L. Begel, T. Galstian, Liquid crystal lens with corrected wavefront asymmetry, *Appl. Opt.* 57 (2018) 5072–5078. <https://doi.org/10.1364/AO.57.005072>.
- [69] A. Zohrabyan, T. Galstian, K. Asatryan, V. Presniakov, M. Thiboutot, A. Bagramyan, A. Tork, J. Parker, T. Cooper, B. Khodadad, “In-flight auto focus method and system for tunable

- liquid crystal optical element,” U.S. patent 15,196,421, 29 June, 2016.
- [70] G. Li, P. Valley, P. Äyräs, D.L. Mathine, S. Honkanen, N. Peyghambarian, High-efficiency switchable flat diffractive ophthalmic lens with three-layer electrode pattern and two-layer via structures, *Appl. Phys. Lett.* 90 (2007) 2005–2008. <https://doi.org/10.1063/1.2712773>.
- [71] G. Li, D.L. Mathine, P. Valley, P. Ayras, J.N. Haddock, M.S. Giridhar, G. Williby, J. Schwiegerling, G.R. Meredith, B. Kippelen, S. Honkanen, N. Peyghambarian, Switchable electro-optic diffractive lens with high efficiency for ophthalmic applications, *Proc. Natl. Acad. Sci.* 103 (2006) 6100–6104. <https://doi.org/10.1073/pnas.0600850103>.
- [72] D.S. Goodman, *Geometric Optics*, in: M. Bass (Ed.), *Handbook of Optics*, McGraw- Hill, New York, NY, 1995.
- [73] D. Malacara, *Optical Shop Testing*, 3rd ed., John Wiley & Sons, Inc., Hoboken, NJ, USA, 2007. <https://doi.org/10.1002/9780470135976>.
- [74] I.R. Guralnik, V.N. Belopukhov, G.D. Love, A.F. Naumov, Interdependence of the electrical and optical properties of liquid crystals for phase modulation applications, *J. Appl. Phys.* 87 (2000) 4069–4074. <https://doi.org/10.1063/1.373032>.
- [75] J.H. Mathews, K.D. Fink, *Numerical Methods Using Matlab*, 4th ed., Prentice-Hall Inc., New Jersey, USA, 2004.
- [76] T. Galstian, K. Asatryan, V. Presniakov, A. Bagramyan, A. Tork, A. Zohrabyan, S. Careau, “Liquid crystal optical device with advanced electric field control capability,” U.S. patent 9,833,312, December 5, 2017.
- [77] K. Richdale, M.A. Bullimore, K. Zadnik, Lens thickness with age and accommodation by optical coherence tomography, *Ophthalmic Physiol. Opt.* 28 (2008) 441–447. <https://doi.org/10.1111/j.1475-1313.2008.00594.x>.
- [78] A. Hassanfiroozi, Y.-P. Huang, B. Javidi, H.-P.D. Shieh, Hexagonal liquid crystal lens array for 3D endoscopy, *Opt. Express*. 23 (2015) 971–981. <https://doi.org/10.1364/oe.23.000971>.
- [79] A. Hassanfiroozi, Y.-P. Huang, B. Javidi, H.-P.D. Shieh, Dual layer electrode liquid crystal lens for 2D/3D tunable endoscopy imaging system, *Opt. Express*. 24 (2016) 8527–8538. <https://doi.org/10.1364/OE.24.008527>.
- [80] T. Galstian, H. Earhart, “Reprogrammable tuneable liquid crystal lens intraocular implant and methods therefor,” U.S. patent 20160106533, April 21, 2016.
- [81] P. Clark, T. Galstian, K. Asatryan, V. Presniakov, A. Bagramyan, A. Tork, A. Zohrabyan, S. Careau, “Methods and apparatus for focus improvement in multiple liquid crystal cell lenses,” U.S. patent US14777086, February 11, 2016.
- [82] T. Galstian, “Tuneable liquid crystal lens intraocular implant and methods therefor,” U.S. patent 10,098,727, October 16, 2018.
- [83] Y.-H. Lin, Y.-J. Wang, Electrically tunable liquid crystal lenses for augmented reality, in: *Front. Opt. / Laser Sci.*, OSA, Washington, D.C., 2018: p. FM3D.7. <https://doi.org/10.1364/FIO.2018.FM3D.7>.
- [84] M.B. Kumar, D. Kang, J. Jung, H. Park, J. Hahn, M. Choi, J.-H. Bae, H. Kim, J. Park, Compact vari-focal augmented reality display based on ultrathin, polarization-insensitive, and adaptive liquid crystal lens, *Opt. Lasers Eng.* 128 (2020). <https://doi.org/10.1016/j.optlaseng.2020.106006>.
- [85] J.C. Jones, M. Wahle, J. Bailey, T. Moorhouse, B. Snow, J. Sargent, Polarisation independent

- liquid crystal lenses and contact lenses using embossed reactive mesogens, *J. Soc. Inf. Disp.* 28 (2020) 211–223. <https://doi.org/10.1002/jsid.874>.
- [86] B. Winn, D. Whitaker, D.B. Elliott, N.J. Phillips, Factors affecting light-adapted pupil size in normal human subjects., *Invest. Ophthalmol. Vis. Sci.* 35 (1994) 1132–1137. <http://www.ncbi.nlm.nih.gov/pubmed/8125724>.
- [87] S.-T. Wu, Design of a liquid crystal based tunable electrooptic filter, *Appl. Opt.* 28 (1989) 48–52. <https://doi.org/10.1364/AO.28.000048>.
- [88] A. Pusenkova, T. Galstian, Reducing the light scattering impact in liquid-crystal-based imaging systems, *Appl. Opt.* 59 (2020) 4780–4789. <https://doi.org/10.1364/AO.394289>.
- [89] T. Zhan, J. Zou, J. Xiong, X. Liu, H. Chen, J. Yang, S. Liu, Y. Dong, S. Wu, Practical chromatic aberration correction in virtual reality displays enabled by cost-effective ultra-broadband liquid crystal polymer lenses, *Adv. Opt. Mater.* 8 (2020). <https://doi.org/10.1002/adom.201901360>.
- [90] T. Okada, H. Shimazu, A. Toda, S. Sato, “Liquid crystal lenses having a Fresnel lens,” U.S. patent 4,904,063, February 27, 1990.
- [91] S. Sato, A. Sugiyama, R. Sato, Variable-focus liquid-crystal Fresnel lens, *Jpn. J. Appl. Phys.* 24 (1985) L626–L628. <https://doi.org/10.1143/JJAP.24.L626>.
- [92] Y. Ooi, T. Nomura, T. Kakiuchi, M. Oosawa, Y. Tanabe, “Liquid crystal lens element optical head device,” U.S. patent 7,738,344, June 15, 2010.
- [93] S. Suyama, M. Date, S. Kohda, K. Kato, S. Sakai, “Liquid crystal optical device,” U.S. patent 6,469,683, October 22, 2002.
- [94] H.T. Dai, Y.J. Liu, X.W. Sun, D. Luo, A negative–positive tunable liquid-crystal microlens array by printing, *Opt. Express.* 17 (2009) 4317–4323. <https://doi.org/10.1364/OE.17.004317>.
- [95] L. Li, D. Bryant, P.J. Bos, Liquid crystal lens with concentric electrodes and inter-electrode resistors, *Liq. Cryst. Rev.* 2 (2014) 130–154. <https://doi.org/10.1080/21680396.2014.974697>.
- [96] T. Galstian, K. Asatryan, V. Presniakov, A. Bagramyan, A. Zohrabyan, S. Careau, “Flat liquid crystal layered Fresnel lens device,” patent WO 2017/197533, November 23, 2017.
- [97] J. Li, C.-H. Wen, S. Gauza, R. Lu, S.-T. Wu, Refractive indices of liquid crystals for display applications, *J. Disp. Technol.* 1 (2005) 51–61. <https://doi.org/10.1109/JDT.2005.853357>.
- [98] N.R. Draper, H. Smith, *Applied Regression Analysis*, 3rd ed., 1998.
- [99] W.J. Smith, *Modern Optical Engineering: The Design of Optical Systems*, McGraw-Hill, 2008. <https://doi.org/10.1036/0071476873>.
- [100] Raspberry pi 4 specifications, (2020). <https://www.raspberrypi.org/products/raspberry-pi-4-model-b/specifications/>.
- [101] The raspberry pi camera module v2 specifications, (2020). <https://www.raspberrypi.org/products/camera-module-v2/>.
- [102] N. Koren, Tutorials on testing photographic systems, (2020). <http://www.normankoren.com/Tutorials/MTF5.html>.
- [103] D.K. Schroder, *Semiconductor Material and Device Characterization*, John Wiley & Sons, Hoboken, New Jersey, USA, 2005. <https://doi.org/10.1002/0471749095>.
- [104] A. Pusenkova, T. Galstian, Electrically tunable liquid crystal lens in extreme temperature conditions, *Mol. Cryst. Liq. Cryst.* 703 (2020) 39–51.

<https://doi.org/10.1080/15421406.2020.1743941>.

- [105] J.A. Nelder, R. Mead, A simplex method for function minimization, *Comput. J.* 7 (1965) 308–313. <https://doi.org/10.1093/comjnl/7.4.308>.
- [106] M. Khosrow-Pour, *Advanced Methodologies and Technologies in Artificial Intelligence, Computer Simulation, and Human-Computer Interaction*, IGI Global, 2019. <https://doi.org/10.4018/978-1-5225-7368-5>.
- [107] D.G. Voelz, *Computational Fourier Optics: A MATLAB Tutorial*, SPIE, 2011. <https://doi.org/10.1117/3.858456>.